THE EFFECTS OF CESIUM DEPOSITION AND GAS EXPOSURE ON THE FIELD EMISSION PROPERTIES OF SINGLE WALL AND MULTIWALL NANOTUBES

Atul Wadhawan , B.S.

Dissertation Prepared for the Degree of

DOCTOR OF PHILOSOPHY

UNIVERSITY OF NORTH TEXAS

May 2002

APPROVED:

Jose Perez, Major Professor
Duncan Weathers, Committee Member
Terry Golding, Committee Member
Zhibing Hu, Committee Member
Sam Matteson, Chair of Department of Physics
C. Neal Tate, Dean of the Robert B. Toulouse School of Graduate Studies

Wadhawan, Atul., The Effects of Cesium Deposition and Gas Exposure on the Field Emission Properties of Single Wall and Multiwall Carbon Nanotubes. Doctor of Philosophy (Physics), May 2002, 118 pp., 7 tables, 47 illustrations, references, 52 titles.

The effects of Cs deposition on the field emission (FE) properties of single-walled carbon nanotube (SWNT) bundles were studied. In addition, a comparative study was made on the effects of O_2, Ar and H_2 gases on the field emission properties of SWNT bundles and multiwall carbon nanotubes (MWNTs).

We observed that Cs deposition decreases the turn-on field for FE by a factor of 2.1 - 2.9 and increases the FE current by 6 orders of magnitude. After Cs deposition, the FE current versus voltage (*I-V*) curves showed non-Fowler-Nordheim behavior at large currents consistent with tunneling from adsorbate states. At lower currents, the ratio of the slope of the FE *I-V* curves before and after Cs deposition was approximately 2.1. Exposure to N_2 does not decrease the FE current, while exposure to O_2 decreases the FE current. Our results show that cesiated SWNT bundles have great potential as economical and reliable vacuum electron sources.

We find that H_2 and Ar gases do not significantly affect the FE properties of SWNTs or MWNTs. O_2 temporarily reduces the FE current and increases the turn-on voltage of SWNTs. Full recovery of these properties occurred after operation in UHV. The higher operating voltages in an O_2 environment caused a permanent decrease of FE current and increase in turn-on field of MWNTs. The ratios of the slopes before and after O_2 exposure were approximately 1.04 and 0.82 for SWNTs and MWNTs, respectively. SWNTs compared to MWNTs would appear to make more economical and reliable vacuum electron sources.

ACKNOWLEDGMENTS

This work was supported by the Texas Advanced Technology Program under Award No. 003594-048-1999, and by the National Science Foundation under Award No. DMR-0074636.

TABLE OF CONTENTS

LIST OF TABLES

LIST OF ILLUSTRATIONS

CHAPTER 1

INTRODUCTION

This dissertation deals with two related subjects : effects of cesium deposition on the field emission (FE) properties of single wall carbon nanotube (SWNT) bundles and the effects of Ar, H_2, and O_2 gases on the FE properties of single wall carbon nanotubes and multiwall carbon nanotubes (MWNTs).

1.1 Carbon Nanotubes as Electron Sources

Electron sources are becoming increasingly important in research and everyday life in devices such as cathode ray tubes (CRTs), vacuum tubes and microwave generators. Formerly electron sources relied mostly on thermionic electron emission, a process where electrons are heated from the tail of the Fermi level of the emitter into vacuum [1]. The temperature of the cathode needs to be over 2000°C to allow free electrons to escape from the surface. As a result, exposure of the heated emitter to residual oxygenic gases in the vacuum seriously poisons the cathodes [2,3]. In addition, radiative heating from the filaments could also damage surrounding devices [1]. Both

exposure to residual gases and radiative heating greatly limit the lifetime of the emission devices.

A better alternative to thermionic emission is cold cathode emission where electrons are emitted by reducing the surface potential barrier of the cathode by applying an electric field. If an electric field is applied to the surface of a solid the potential step confining the electrons to the solid becomes a potential barrier triangular in shape. If the width of the surface barrier becomes narrow enough, electrons will tunnel from the highest occupied states of the solid into the surrounding vacuum. Thus it differs from thermionic emission where only electrons with sufficient energy to go over the potential barrier are emitted.

Materials such as molybednum microtip arrays are available for potential commercial applications as FE electron sources in flat panel displays. Metals such as tungsten and platinum are routinely etched into sharp tips for use in scanning tunneling microscopy (STM) – a fundamental tool in surface science research. Numerous other scientific instruments and techniques such as atomic force microscopy, field emission microscopy, etc, rely on metallic tips for their analyzing capabilities. Thus the recent discovery of carbon nanotubes (CNTs) is set to revolutionize the commercial and scientific communities with their exceptional electronic and mechanical properties.

Why are CNTs such good field emitters? As discussed in chapter 2, the exact mechanism by which CNTs field emit is not clearly understood. However, an inherently high aspect ratio (that is, the ratio of length to diameter) which causes the amplification of the local external electric field seems to be an important factor. Another advantage

CNTs possess over other types of emitters is high chemical and mechanical stability which make them inherently more durable in vacuum environments [4]. Finally CNTs are capable of sustaining large current densities with low external fields which makes them more economical to operate when compared to other types of emitters.

1.2 Effects of Cs Deposition on the Field Emission Properties of Single-Walled Carbon Nanotube Bundles

It has been well established that the work function of a metal or semiconductor surface is reduced even after a partial coverage of cesium [5,6]. Cs deposition on metal field emitters such as Mo micro-tip arrays has been reported to increase the FE current from this material by lowering its work function [7]. Moreover deposition of cesium onto carbon and diamond films has also been shown to reduce their workfunctions and enhance field emission characteristics [8,9].

Deposition of alkali metals such as Cs, K and Na onto CNTs has also been performed in recent years. Due to their different structure and packing , deposition onto SWNT bundles is likely to be different from that of MWNTs where alkali metals can be intercalated in between the concentric shells if defects are present [10,11]. Recently Cs was deposited on laser ablation synthesized SWNT bundles and the sample analyzed using direct transmission electron microscopy (TEM) and electron energy loss spectroscopy (EELS) [12]. Using EELS and TEM it was shown that the intercalation of Cs caused structural disorder to the two dimensional lattice of the SWNT nanotube

bundles and that most of the deposited Cs did not remain on the surface, but reversibly intercalated in between the nanotube bundles [12].

Transport and electronic properties of doped SWNTs have been investigated as well. Cs and K deposition have been shown to decrease resistance and increase conductivity of SWNTs [13,14,15]. But in a context more relevant to FE research, the work function of Cs-intercalated SWNT bundles was measured using ultraviolet spectroscopy (UPS) [16]. UPS has an advantage over other techniques used to measure work functions such as FE or Schottky emission in that it does not employ any uncertain parameters. Our work described in Chapter 4 which measures the FE properties of cesiated SWNTs is a logical extension of this previous research.

1.3 Effects of O_2, Ar and H_2 gases on the Field Emission Properties of Single-Walled and Multiwall Carbon Nanotubes.

CNTs have shown great potential in vacuum microelectronic devices principally because they require low operating voltages to sustain high currents [17,18]. But to become viable technological devices, reliability of operation under extreme operational conditions must be established. A key aspect to operating in an evacuated environment is understanding how emitters react with ambient residual gases that are unavoidably present. There are several potential sources of gases in typical emitter setups such as out-gassing of materials, residue from fabrication processes, electron stimulated desorption from phosphors and surfaces, phenomena associated with high electric fields dissociation

and ionization, ion sputtering and electron impact ionization of the gases between gate and phosphors [19].

A lot of interest has been shown of late on the effects of gases on the electronic and transport properties of carbon nanotubes . The electrical conductance of a semi-conducting SWNT is known to increase upon exposure to nitrogen dioxide and decrease with exposure to NH_3 [20]. Also, oxygen in particular has been found to have a marked effect on the electrical properties of SWNTs [21]. While a lot of the recent work relates to the transport measurements of CNTs, little has been done to determine the impact of residual gas exposure as it relates to field emission (FE). Previous studies have reported about the effects of gases on the FE of CNTs, but these experiments were limited to an initial single current value over a period of gas exposure [4,22,23,24]. Also lacking is a comparative analysis among the various types of CNTs , such as single wall carbon nanotubes (SWNTs) and multiwall carbon nanotubes (MWNTs). Prior to our research a case could be made that MWNTs because of their multi-layer structure are more reliable and durable practical emitters. The results presented in chapter 5 assert that the lower operational voltages of SWNTs not only make them more economical emitters but also afford them a greater degree of protection.

References

1. J. E. Jaskie, *MRS Bulletin* **21**, 3,59 (1996).

2. C. R. K. Marrian, G.A. Haas and A. Shih, *Appl. Surf. Sci.* **16,**73 (1983).

3. G. A. Haas, R. E. Thomas, C. R. K. Marrian and A. Shih, *IEEE Trans. Electron Dev.* **ED-38**, 2244 (1991).

4. K. A. Dean, and B. R. Chalamala, *Appl. Phys. Lett*. **75**, 3017 (1999).

5. M. W. Geis and J. C. Twichell, *Appl.Phys. Lett.* **67**, 1328 (1995).

6. R. U. Martinelli and D. G. Fischer, *Proc. IEEE* **62**, 1339 (1974).

7. J. M. Macaulay, I. Brodie, C. A. Spindt, and C. E. Holland, *Appl. Phys. Lett*. **61**, 997 (1992).

8. Y. W. Ko and S. I. Kim, *J. Appl. Phys.* **82**, 2631 (1997).

9. L. S. Pan, T. E. Felter, D. A. A. Ohlberg, W. L. Hsu, C. A. Fox, R. Cao, and G. Vergara, *J. Appl. Phys.* **82**, 2624 (1997).

10. O. Zhou, R. M. Fleming, D. W. Murphy, C. H. Chen, R. C. Haddon, A. P. Ramirez, S. H. Glarum, *Science* **263** , 1744 (1994).

11. S. Suzuki, and M. Tomita, *J. Appl. Phys.* **79** 3739 (1996).

12. S. Suzuki, C. Bower and O. Zhou, *Chem. Phys. Lett* **285**, 230 (1998).

13. R. S. Lee, H. J. Kim, J. E. Fisher, A. Thess, R. E. Smalley, *Nature* **388,** 257 (1997).

14. A. M. Rao, P. C. Eklund, S. Bandow, A. Thess, R. E. Smalley, *Nature* **388**, 257 (1997).

15. L. Grigorian, G. U. Sumanasekera, A. L. Loper, S. Fang, J. L. Allen, and P.C. Eklund, *Phys. Rev. B* **58,** R4195 (1998).

16. S. Suzuki, C. Bower, Y. Watanabe and O. Zhou, *Appl Phys. Lett*.. **76**, 4007 (2000).

17. A. G. Rinzler, J. H. Hafner, P. Nikolaev, L. Lou, S. G. Kim, D. Tomanek, P. Nordlander, D. T. Nordlander, D. T. Colbert, and R. E. Smalley, *Science* **269**, 1550 (1995).

18. W. A. de Heer, A. Chatelain, and D. Ugarte, *Science* **270**, 1179 (1995).

19. B. R. Chalamala, R. M. Wallace and B. E. Gnade, *J.Vac. Sci. Technol. B* **16** 2859 (1998).

20. J. Kong, N. R. Franklin, C. Zhou, M. G. Chapline, S. Peng, K. Cho, and H. Dai, *Science* **287**, 622 (2000).

21. P. G. Collins, K. Bradely, M. Ishigami, and A. Zettl, *Science* **287**, 1801 (2000).

22. J. -M. Bonard, J. -P. Salvetat, T. Stockli, W. A. de Heer, *Appl. Phys. Lett*. **73**, 918 (1998).

23. J. -M. Bonard, F. Maier, T. Stockli, A. Chatelain, W. A. de Heer, J. -P. Salvetat, and L. Forro, *Ultramicroscopy* **73**, 7 (1998).

24. D. S. Chung, W. B. Choi, J. H. Kang, H. Y. Kim, and I. T. Han, Y. S. Park, Y. H. Lee, N. S. Lee, J. E. Jung, and J. M. Kim, *J. Vac. Sci. Technol.* **B 18**, 1054 (2000).

CHAPTER 2

THEORETICAL BACKGROUND

2.1 Introduction

In sections 2.2 and 2.3 of this chapter I briefly describe how carbon atoms are configured to form the complex nanotube structure, and how restrictions placed upon these structures give rise to the unique and diverse electronic properties of carbon nanotubes. In this description I concentrate mainly on single wall carbon nanotubes which can be thought of as the fundamental building blocks of all types of nanotubes including those that were utilized in my experiments, namely the rope-like bundles of single walls and the multiwall nanotubes.

Sections 2.4 – 2.5 deal with field emission (FE) theory as it applies to carbon nanotubes. The exact mechanism by which carbon nanotubes field emit is still not clearly understood. Unlike graphite which is a semi-metal, carbon nanotubes form as either semiconductors or metals. Thus sections 2.3 and 2.4 deal with FE from conventional metallic and semiconducting tips, respectively. Another mechanism by which nanotubes are thought to emit is through adsorbate states formed due to the presence of “impurity” molecules adsorbed on the nanotube surface. Section 2.5 briefly explains this emission model. Finally section 2 highlights how one cannot rule out the influence of localized states situated on the end caps of carbon nanotubes. However, this is the least developed

of the emission theories since the discovery of localized states on the end caps of carbon nanotubes is a recent phenomenon. In all likelihood, carbon nanotubes field emit utilizing some or all of the mechanisms mentioned above. Perhaps one model dominates over the others depending on how the carbon nanotubes are grown and then prepared for experimentation.

2.2 Structure of Single-Wall Nanotubes

Carbon atoms are found to exist in a variety of forms such as diamonds, graphite, carbon fibers and nanotubes. This abundance in variety is principally due to the many configurations the four valence electrons of carbon adopt in forming bonds—a process called hybridization. In sp^2 hybridization, the 2s orbital and two 2p orbitals of a carbon atom are mixed to form hybrid bonds with other atoms. Graphite which consists of layers of hexagonal lattices of carbon atoms is an example of sp^2 bonded carbon atoms. A single layer of graphite forms a two-dimensional material called a graphene layer. A single wall carbon nanotube (SWNT) can basically be described as a graphene sheet rolled up into a seamless cylindrical shape. A basic building unit of the single wall nanotube is the six-membered structure known as a benzene ring. Its orientation relative to the axis of the nanotube provides many possible structure and properties for carbon nanotubes. Figure 2.1 shows the three possible examples of SWNTs with their end caps detached . Each end-cap is basically a hemisphere of a carbon fullerene -- a sixty-carbon atom structure

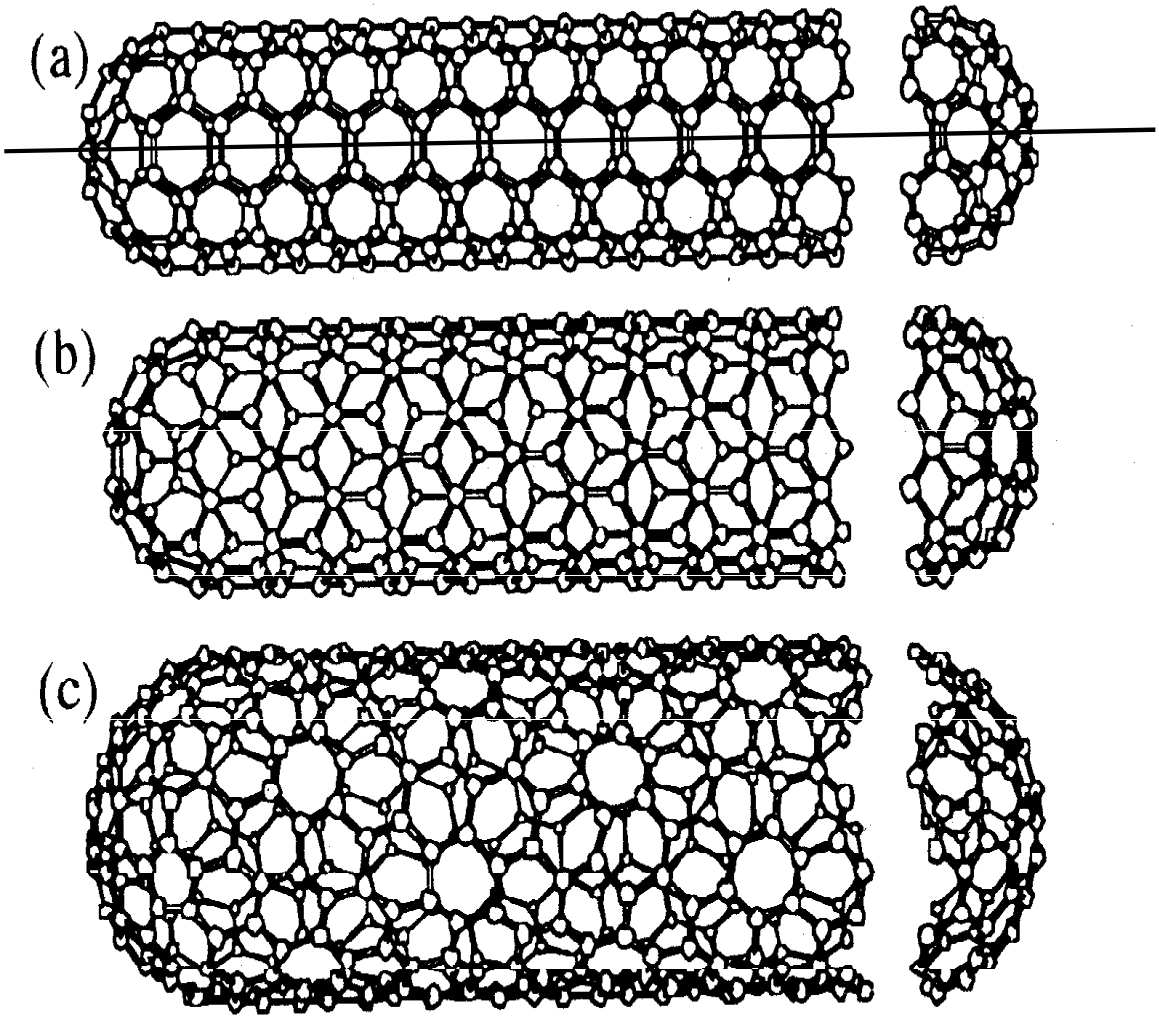

Figure 2.1 The orientation of the six-membered benzene ring determines the symmetry classification of carbon nanotubes: (a) armchair, (b) zigzag, and (c) chiral nanotubes. For armchair carbon nanotubes the benzene rings are lined up with the axis of the nanotube allowing metallic conduction of electrons [Adapted from Ref 8].

discovered in the early 1990's and popularly known as a "buckyball". The end-caps are different from the rest of the tube in that they contain six pentagons along with the requisite number of hexagons needed to fit perfectly to the cylindrical body.

Carbon nanotubes have two types of symmetry classifications: achiral (symmorphic) or chiral (non-symmorphic). An achiral nanotube is one whose mirror image is identical to the original. There are only two cases of of achiral nanotubes – armchair and zigzag as shown in Figure 2.1 (a) and (b) respectively. Armchair and zigzag are so designated due to the shape of the cross-sectional ring shown at the edge of the nanotubes in Figure 2.1. Basically one can roll up a graphene sheet along one of its symmetry axis and obtain an armchair or a zigzag nanotube. On the other hand if you roll up a graphene sheet in a direction other than a symmetry axis you get chiral nanotubes. Thus chiral nanotubes possess a spiral symmetry whose mirror image is not identical to the original.

The primitive cell or unit cell for a carbon nanotube in real space is shown by the quadrilateral OAB$'$B in Figure 2.2 . The figure illustrates the unrolled graphene sheet lattice of the nanotube, in which the vector **OB** is in the direction along the nanotube axis. The vector **OA** which is perpendicular to **OB** is an important structural parameter of the nanotube. As the graphene sheet is rolled end to end, **OA** lies along the circumference of the nanotube. **OA** and **OB** help define the translational vector **T** and the chiral vector **C** which determines the symmetry properties of the nanotube.

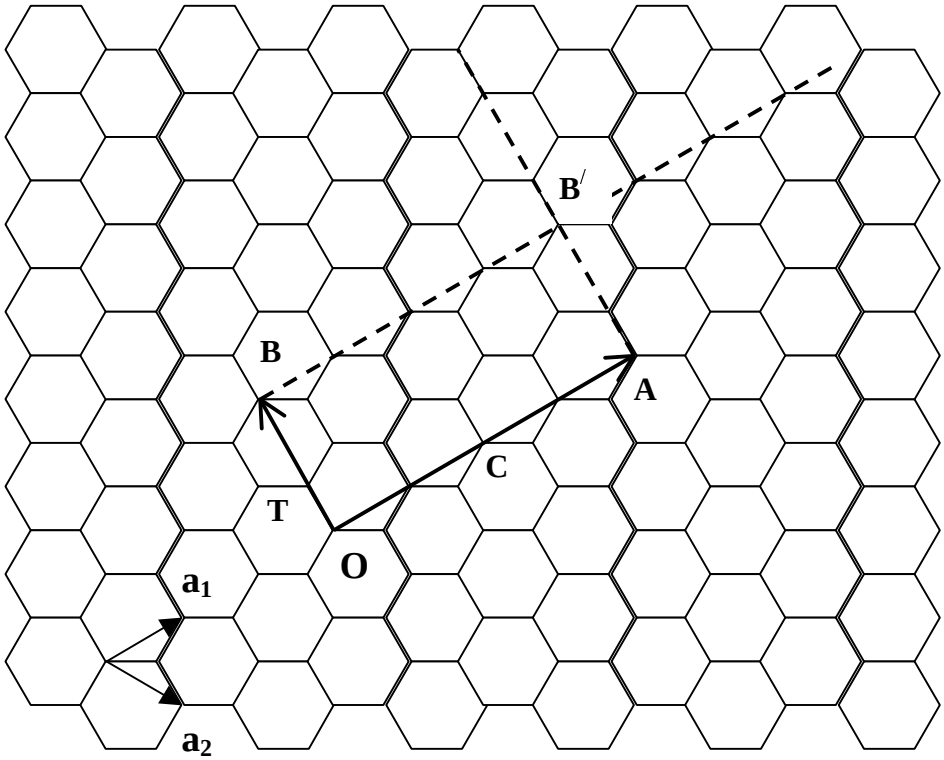

Figure 2.2 Illustration of the chiral vector of a zigzag **C** = (4, 0) nanotube. Also depicted is the translational vector **T** for this nanotube. The quadrilateral OAB/B defines the unit cell in real space.

The chiral vector **C** is given by

$$\mathbf{C} = n\mathbf{a}_1 + m\mathbf{a}_2 \equiv (n, m) \qquad (2.1)$$

where n, m are integers and $0 \leq |m| \leq n$. $\mathbf{a_1}$ and $\mathbf{a_2}$ are the real space unit vectors of the graphene sheet. **C** essentially determines the nanotube because if you move n times the vector $\mathbf{a_1}$ along the graphene sheet and then m times $\mathbf{a_2}$ from the origin you get to the tip of the chiral vector. Then you roll up the sheet so that the origin coincides with the tip of **C** and a nanotube is realized. For the case **C** = (n, 0), that is integer m = 0, we have a zigzag nanotube. If **C** = (n , n), that is n = m, an armchair nanotube results. All other (n, m) combinations result in chiral nanotubes. The diameter of the nanotube is also determined by the chiral vector and is given by :

$$d = L / \pi \quad \text{where} \tag{2.2}$$

$$L = |\mathbf{C}| = a(n^2 + m^2 + nm)^{1/2} . \tag{2.3}$$

The translation vector **T** is given by

$$\mathbf{T} = t_1\mathbf{a_1} + t_2\mathbf{a_2} \equiv (t_1 , t_2) \tag{2.4}$$

where t_1 and t_2 are integers. **T** lies parallel to the nanotube axis and is perpendicular to **C**. Figure 2.3 shows the reciprocal lattice vectors $\mathbf{K_1}$ and $\mathbf{K_2}$ for the **C** = (4, 0) achiral zigzag nanotube. Expressions for $\mathbf{K_1}$ and $\mathbf{K_2}$ are obtained from the orthogonality relations

$$\mathbf{C} \cdot \mathbf{K_1} = 2\pi \qquad \mathbf{T} \cdot \mathbf{K_1} = 0$$

$$\mathbf{C} \cdot \mathbf{K_2} = 0 \qquad \mathbf{T} \cdot \mathbf{K_2} = 2\pi \tag{2.5}$$

From these we get ,

$$\mathbf{K_1} = 1/N\ (-t_2\mathbf{b_1} + t_1\mathbf{b_2}), \qquad \mathbf{K_2} = 1/N\ (m\mathbf{b_1} - n\mathbf{b_2}) \tag{2.6}$$

where $\mathbf{b_1}$ and $\mathbf{b_2}$ are the reciprocal lattice vectors of the graphene sheet and N is the number of hexagons in the nanotube unit cell. Thus for the **C** = (4, 0) nanotube whose real space unit cell is shown in Figure 2.2, the reciprocal space vectors are:

$$\mathbf{K_1} = \mathbf{b_1}/4 + \mathbf{b_2}/8\ , \qquad \mathbf{K_2} = -\ \mathbf{b_2}/2\ . \tag{2.7}$$

These are represented on the honeycomb lattice in Figure 2.3. The vectors $\mathbf{K_1}$ and $\mathbf{K_2}$ are the reciprocal space vectors that correspond to the chiral vector **C** and translational vector **T**, respectively which exist in real space.

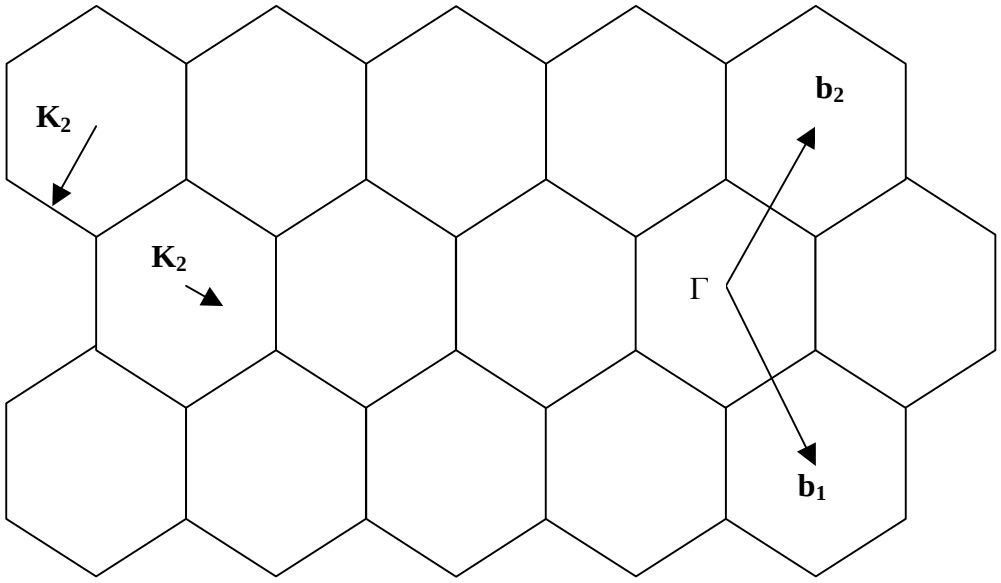

Figure 2.3 The reciprocal lattice of the **C** = (4 , 0) zigzag nanotube. The vectors $\mathbf{K_1}$ and $\mathbf{K_2}$ are the reciprocal space vectors corresponding to **C** and **T**. The vectors $\mathbf{b_1}$ and $\mathbf{b_2}$ are the unit reciprocal space vectors for a graphene sheet.

2.3 Structure of Multiwall Nanotubes

A few researchers have hypothesized that the layered structure of multiwall nanotubes consist of a scroll like or "Swiss roll" structure [1,2]. However most experimental evidence points to the structure of multiwall nanotubes as consisting of concentric shells of discrete nanotubes, the so called "Russian doll" arrangement [3]. The spacing between the adjacent layers is between 0.34 – 0.36 nm [4] and in most cases the multiwalls have chiral symmetry [5,6] and the various layers have different helicities [7].

2.4 Electronic Properties of Single Wall Nanotubes

A graphite sheet consists of a layer of hexagonally arranged carbon atoms. What holds this honeycomb pattern together are the sp^2 hybridized σ covalent bonds lying in the plane of the graphene sheet. This leaves the π electron orbitals, which are located perpendicular to the sheet, to determine the electronic and solid-state properties of graphite. Thus it is not surprising that the electronic properties of carbon nanotubes , which are basically rolled up graphene sheets, can be determined from a tight-binding calculation for the π electrons of the carbon atoms [8].

The electronic properties of carbon nanotubes arise principally due to the restrictions imposed on the electrons in the nanotube body. In fact the only direction electrons are free to propagate is along the nanotube axis. They are confined radially by the mono-atomic thickness of the graphene sheet and along the circumference by the circular structure of the tube. Thus by using periodic boundary conditions in the circumferential direction, the chiral vector **C** becomes quantized while the wave vector along the axis **T** remains continuous [8].

Dispersion relations which connect wave vectors to energy are most easily obtained for the highly symmetric achiral nanotubes such as the armchair and zigzag tubes. Figure 2.4 depicts the unit cell in real space which contains four carbon atoms and Figure 2.5 shows the Brioullin zone of an armchair nanotube. Energy dispersion relations are calculated along the perimeter of the dotted triangle connecting the high symmetry points Γ, K and M which are at the center, the corner, and the edge as shown in

Figure 2.5. By applying boundary conditions we obtain the energy dispersion relations for a generic armchair **C** = (n, n) nanotube [9]:

$$E^{a}_{q}(k) = \pm t \{1 \pm 4 \cos(q\pi/n) \cos(ka/2) + 4 \cos^{2}(ka/2) \}^{1/2} \qquad (2.8)$$

where, $(-\pi < ka < \pi)$, and $(q = 1,\ldots,2n)$.

The superscript "a" refers to armchair and k is a one dimensional vector in the direction of $\mathbf{K_2}$ (see Figure 2.5). The parameter "a" in Eq (2.8) refers to the length of the unit vector of the nanotube. The resulting one dimensional dispersion relations for the (5, 5) armchair nanotube are shown in Figure 2.6 where six dispersion relations for the conduction band and six for the valence band can be seen. The valence and the conduction bands cross and the resulting degeneracy point is the reason the (5, 5) tube is a zero-gap semiconductor since only infinitesmal excitations are required to excite carriers into the conduction band [8]. All (n, n) armchair nanotubes yield 4n energy subbands analogous to eqn. 2.8 with 2n conduction and 2n valence bands and have a band degeneracy between the highest valence band and the lowest conduction band causing them to exhibit metallic conduction [8-15].

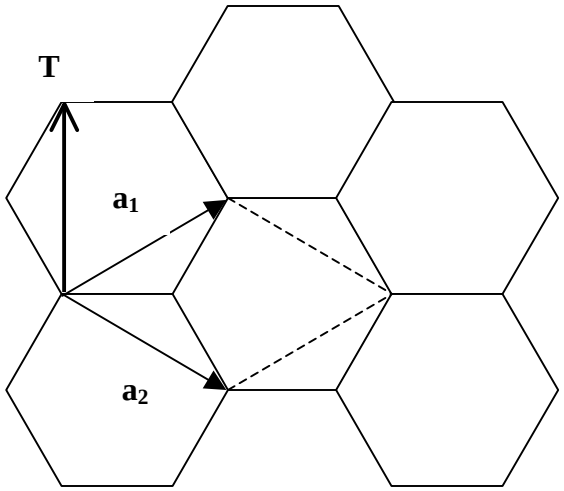

Figure 2.4 The real space lattice of an armchair **C** = (n, n) nanotube. The rhombus formed by the dashed lines is the unit cell of a graphene sheet.

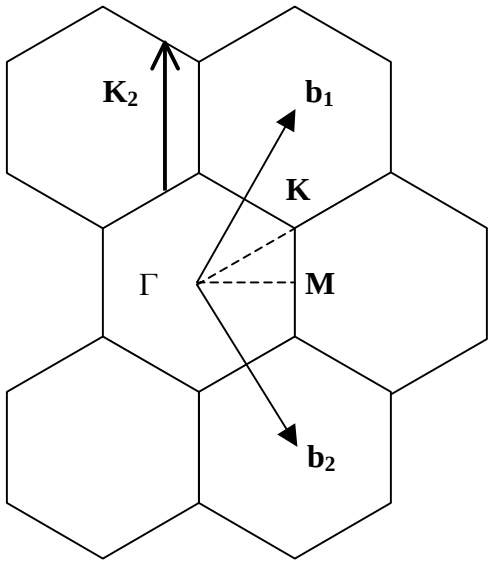

Figure 2.5 The reciprocal lattice of the **C** = (n, n) nanotube. Energy dispersion relations are calculated along the perimeter of the triangle Γ, K, and M.

The energy bands for zigzag nanotubes **C** = (n, 0) are similarly obtained [8]

$$E^{z}_{q}(k) = \pm t \{1 \pm 4 \cos(q\pi/n) \cos(\sqrt{3}ka/2) + 4 \cos^2(q\pi/n)\}^{1/2} \qquad (2.9)$$

$$\text{where,} \quad (-\pi/\sqrt{3} < ka < \pi/\sqrt{3}), \quad \text{and} \quad (q = 1,\ldots,2n)$$

The superscript "z" is for zigzag nanotubes. The one dimensional dispersion relations are shown for (9, 0) and (10, 0) zigzag nanotubes in Figure 2.6. For a general zigzag tube, when n is a multiple of 3 the energy gap at k = 0 (Γ point in Figure 2.5) becomes zero and we have a zero–gap zigzag nanotube. When n is not a multiple of 3, an energy gap at k = 0 appears.

Similar analyses done for the dispersion relations of chiral nanotubes show that the nanotubes can be classified into general categories depending on the relationships between the chiral numbers n and m [16,17]. If the greatest common divisor between the sum (n – m) and the integer 3 is one, then the chiral nanotube will be a semiconductor. If however the sum (n – m) is a multiple of 3 the nanotubes exhibit metallic properties.

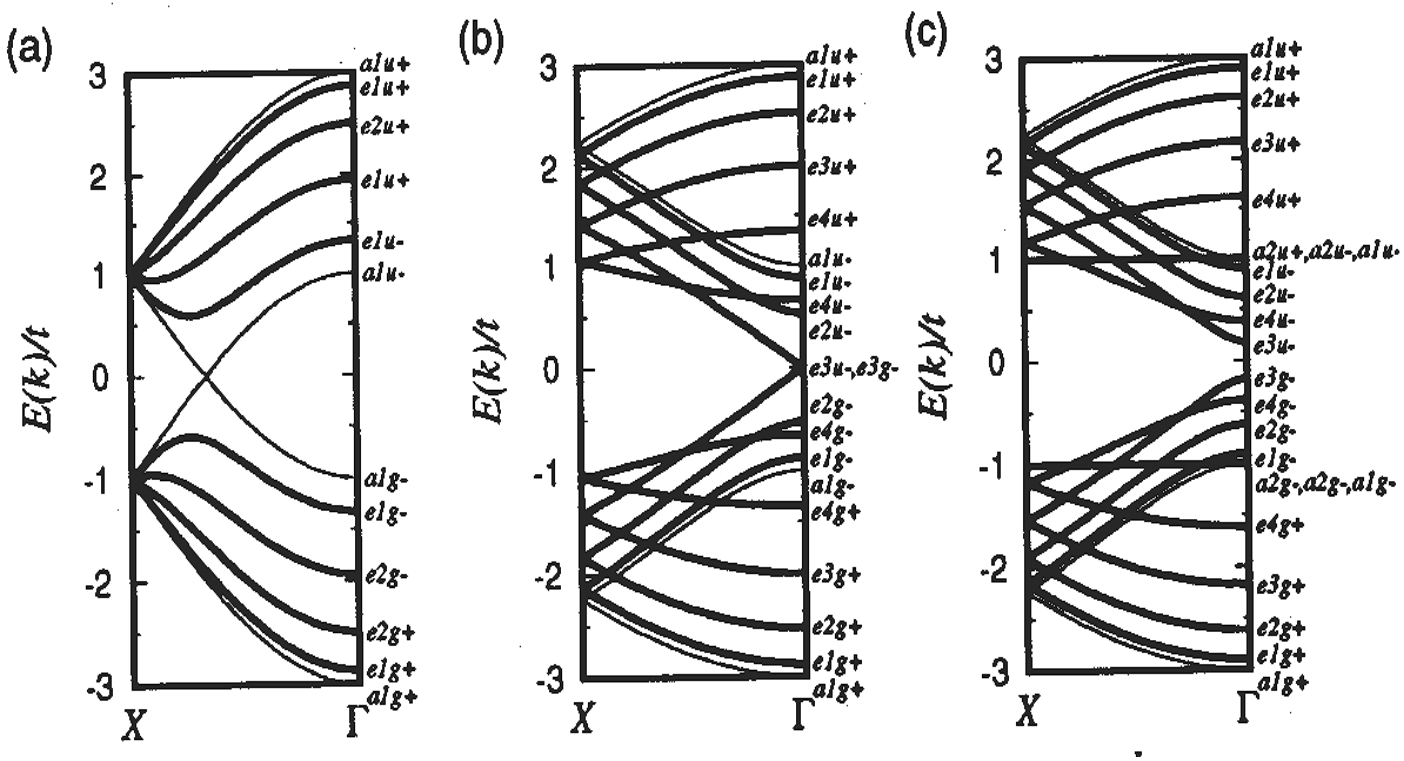

Figure 2.6 One dimensional dispersion relations for (a) armchair (5, 5) (b) zigzag (9, 0) and (c) zigzag (10, 0) nanotubes. The Γ point corresponds to k = 0 while the X point corresponds to k = ± π/a for armchair and k = ± π/√3a for zigzag nanotubes. [From Ref.8]

The one dimensional density of electronic states as a function of energy is another parameter of interest. As discussed in section 2.9 electronic states located on the caps of nanotubes are believed to play a pivotal role in the enhanced field emission mechanisms of nanotubes. Figure 2.7 shows the density of states for armchair (8, 8), (9, 9), (10, 10), and (11, 11) nanotubes. These like all armchair nanotubes are metallic; however, their density of states differs from the smoothly profiled density of states of conventional metals. The peaks shown in Figure 2.7 correspond to energy subbands and are important in analyzing experimental results.

2.5 Electronic Properties of Multiwall Nanotubes

The electronic properties of multiwall nanotubes can be understood in terms of the structure of the constituent single wall nanotubes [8]. The electronic structural difference between single and multiwall nanotubes is mainly due to the difference in the diameter of the tubes rather than in the numbers of concentric graphene sheets [18]. This is because experiments have shown that electronic properties like conductance in multiwall nanotubes are governed by only one of the concentric tubes [19,20,21]. More than likely this is the outermost shell. The electronic density of states of a multiwall nanotube can be approximated in terms of a superposition of those of the individual single wall nanotubes due to the weak Van der Waal interactions between the concentric shells [8,18].

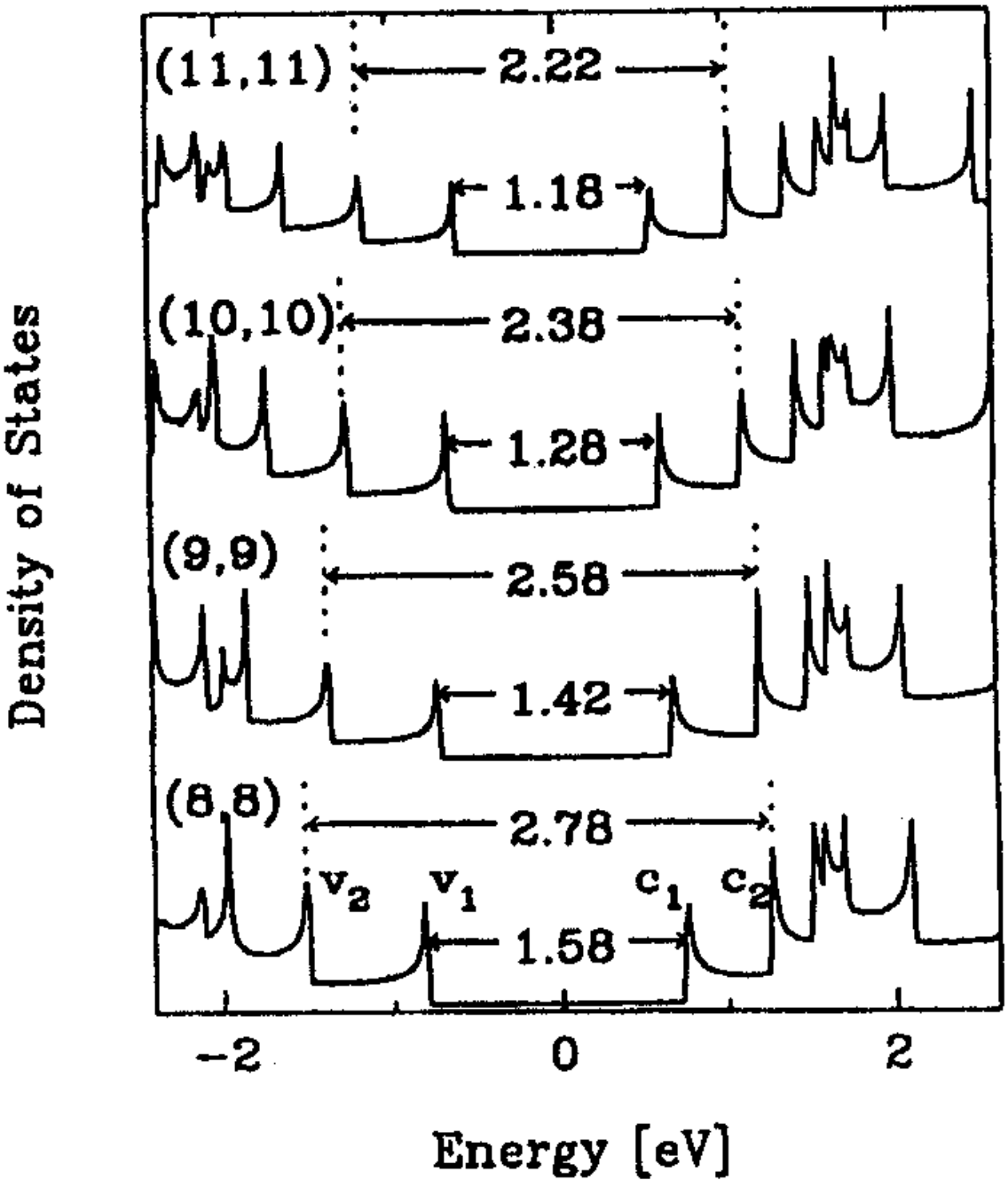

Figure 2.7 Electronic density of states for (8,8), (9,9), (10,10), and (11,11) armchair nanotubes [From Refs.8,22].

2.6 Field Emission From Metallic Conductors

Field emission is a quantum mechanical phenomenon where the potential barrier at the solid's surface has been deformed so greatly by an external field F, that electrons can easily tunnel through it. One can readily develop the condition required for field emission from an analysis of Heisenberg's uncertainty principle,

$$\Delta x \, \Delta \mathrm{p} \approx \hbar \qquad (2.10)$$

where Δx and Δp are the uncertainties in the position and momentum of the electron, respectively, and $\hbar$ is Planck's constant. The uncertainty in the position of the electron is comparable to the width of the barrier, which is given by [23],

$$\Delta x = \left[\left(\frac{\phi}{eF} \right)^2 \right]^{1/2} \qquad (2.11)$$

where ϕ is the barrier height and F the external field.

The uncertainty in momentum of the electron is that corresponding to the height of the barrier ϕ,

$$\Delta p = (2m\phi)^{1/2} \quad . \tag{2.12}$$

Substituting (3) into (1), one gets the uncertainty in position of the electron,

$$\Delta x = \frac{\hbar}{(2\ m\ \phi\ )^{1/2}} \quad . \tag{2.13}$$

For field emission to occur, the barrier width (2.11) should be on the order of magnitude of the uncertainty in the electron position (2.13). This requires that

$$(\phi / eF) \approx \hbar / (2m\phi)^{1/2} \tag{2.14}$$

or

$$(2m)^{1/2}\phi^{3/2}/eF\hbar \cong 1. \tag{2.15}$$

The potential barrier near the surface of the solid is decreased by an image term. This is due to the attractive pull of the image charge experienced by electrons as they depart the

surface. If the external electric field is applied in the 'x' direction, the potential energy function is given by [24],

$$V(x) = (\phi + E_f) - \frac{e^2}{16\pi\varepsilon_o x} - ex F_x \tag{2.16}$$

where E_f is the Fermi energy. As figure 2.8 shows the resulting barrier is smaller than that obtained by neglecting image effects. The position and value of the top of this barrier, called the Schottky saddle [25], is determined by setting the derivative of (2.16) to zero. Thus the position of the Schottky saddle is

$$x_{max} = (e / 16\pi\varepsilon_o F_x)^{1/2} . \tag{2.17}$$

The maximum height of the barrier, called the Schottky saddle point, is given by

$$V_{max} = (\phi + E_f) - (e^3 F_x / 4\pi\varepsilon_o x)^{1/2} \tag{2.18}$$

It was R.H.Fowler and L.W. Nordheim who first utilized quantum mechanical concepts to devise a model to explain the cold emission of electrons from metals [26]. The energy distribution of the emitted electrons which follows Fermi-Dirac statistics is important to the derivation of the Fowler-Nordhiem (F-N) equation. The number of electrons in a unit volume in the momentum range $dp_x dp_y dp_z$ is given by the number of cells in the corresponding volume of phase space multiplied by the Fermi-Dirac distribution function [27]:

$$N(p_x,p_y,p_z)dp_x dp_y dp_z = (2/h^3)(1 + e^{(E-\mu)/kT})^{-1} dp_x dp_y dp_z \quad , \qquad (2.19)$$

or, in terms of velocities ,

$$N(v_x,v_y,v_z)dv_x dv_y dv_z = (2m/h^3)(1 + e^{(E-\mu)/kT})^{-1} dv_x dv_y dv_z \qquad (2.20)$$

where $E = m/2[(v_x)^2 + (v_y)^2 + (v_z)^2]$ and μ is the chemical potential. By first determining the energy distribution of the electrons normal to the emission surface and integrating over E_x one gets the expression for the total current density I [27],

$$I = 6.2 \times 10^{6} [(\mu/\phi)^{1/2} /\alpha^{2}(\phi + \mu)]F^{2}\exp(-6.8\times10^{7}\phi^{3/2}\alpha/F) \quad (2.21)$$

which is the F-N equation for metal emitters. The Fowler - Nordheim equation can be simplified to give the resulting expression :

$$I = aV^{2}\exp\left(\frac{-b\phi^{3/2}}{\beta V}\right) \quad (2.22)$$

where I is the field emission current, a and b are constants, ϕ is the work function, V the applied voltage, and β the geometric enhancement factor. The geometric enhancement factor reflects the geometry of the emission area that is responsible for the presence of high local electric fields. In order to determine the values of a and b, current - voltage (I-V) curves are measured on the assumption that a and b are constant. The slope of the I-V curve at any point where I can be differentiated with respect to V is used to determine the value of $b\phi^{3/2}$. The value of $b\phi^{3/2}$ is substituted into Eq. 2.22, which together with the I-V curve is used to determine the value of a which, primarily depends on the emission surface area.

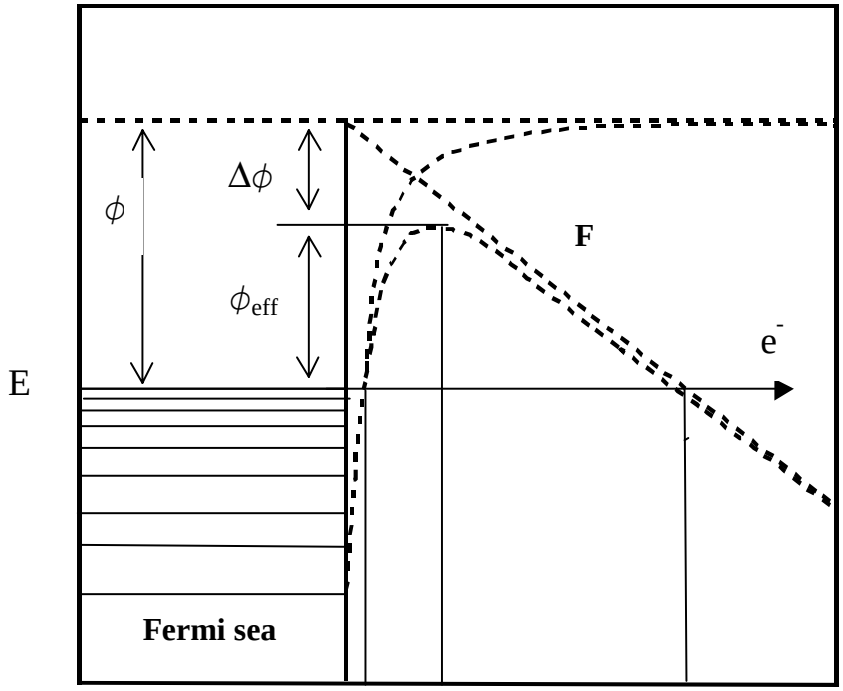

Figure 2.8 Field emission model for electrons tunneling from a metal tip. ϕ is the workfunction of the metal and ϕ_{eff} the effective work function due to the external field. E_f represents the Fermi energy. The external field F deforms the barrier allowing for the tunneling of electrons.

A graph of ln(I / V^2) versus 1/V, called a Fowler-Nordheim (F-N) plot, may then be plotted where the slope of the resulting line depends on the work function and the geometric factor. On the assumption that the geometric factor remains fixed, the variation of the slope may be used to evaluate the relative changes in work function . Conversely if the work function is assumed to remain constant for a particular experimental situation the change in the geometric enhancement factor may be determined.

2.7 Field Emission from Semiconductors

In a metal the Fermi level lies at the highest filled state at 0°K where as in a semiconductor the Fermi level is located approximately at the middle of the energy gap E_g. If impurity donor states are present, the energy required to ionize electrons from these states is E_i . If $kT << E_g/2$ and $E_i >> kT$, the conduction band will be empty. If the external electric field is high enough tunneling of electrons can occur from the top of the valence band as shown in Figure 2.9. In this scenario the image correction becomes considerable and the emission current is given by the modified F-N equation [27],

$$I = 6.2 \times 10^{6} [(\mu/\phi)^{1/2} /\beta^{2}(\phi + \mu)]F^{2}\exp(-6.8\times10^{7}\phi^{3/2}\beta/F), \qquad (2.23)$$

where

$$\beta = \{ 1- (K-1/K + 1)^{1/2} 3.6\times10^{-4} F^{1/2}/(\phi + E_g)\}^{1/2} \qquad (2.24)$$

and K is the dielectric constant of the material.

Field emission occurs from the conduction band of semiconductors if the external field penetrates into the material and twists the conduction band below the Fermi level. The Fermi level is usually close to the undeformed conduction band when donor

impurities are present. If the applied field is high the bottom of the conduction band will tend to dip below μ in n-type materials. This creates a depression in the potential into which electrons will collect as shown in Figure 2.10. These electrons don't congregate in dense enough states to be described by a Boltzmann distribution and consequently follow Fermi statistics. The highest filled state of this pool will coincide with the Fermi energy of the bulk to equalize the chemical potential throughout the material. The field emission current in this scenario is given by [27]:

$$I = 6.2 \times 10^{6} \left[(\mu/\phi - \nu F^{4/5})^{1/2} / \alpha^{2}(\phi - \nu F^{4/5} + \mu)\right] F^{2} \exp(-6.8\times10^{7}(\phi - \nu F^{4/5})^{3/2}\alpha/F) \quad (2.25)$$

where $\nu = 4.5 \times 10^{-7}\ \mathrm{K}^{-2/5}$

and K is the dielectric constant of the material.

Doping semiconductors with impurity atoms containing excess electrons will raise the Fermi level thereby reducing the effective work function. Conversely "hole doping" lowers the Fermi level, increasing the effective work function.

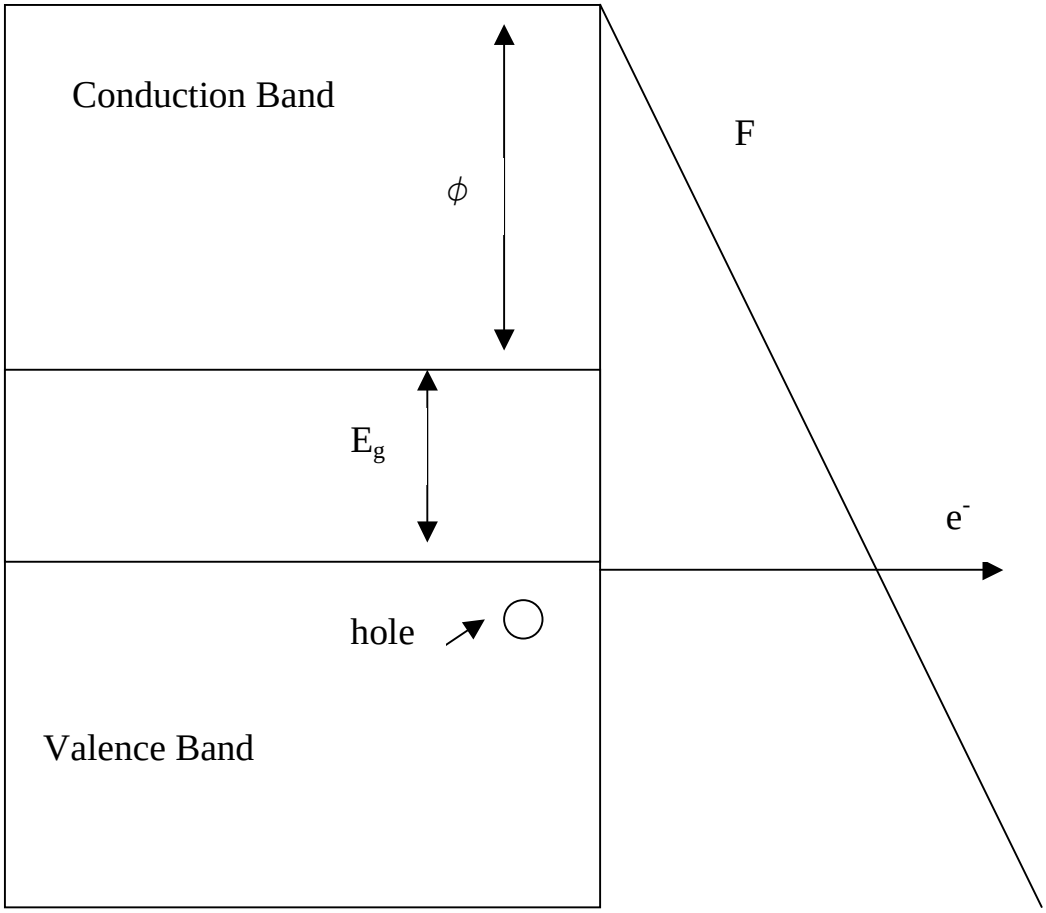

Figure 2.9 Field emission model for the tunneling of electrons from the valence band of a semi-conducting material with an energy gap E_g. The emission of an electron leaves a hole behind in the valence band allowing for enough conduction to balance the emission current. ϕ is the workfunction of the material.

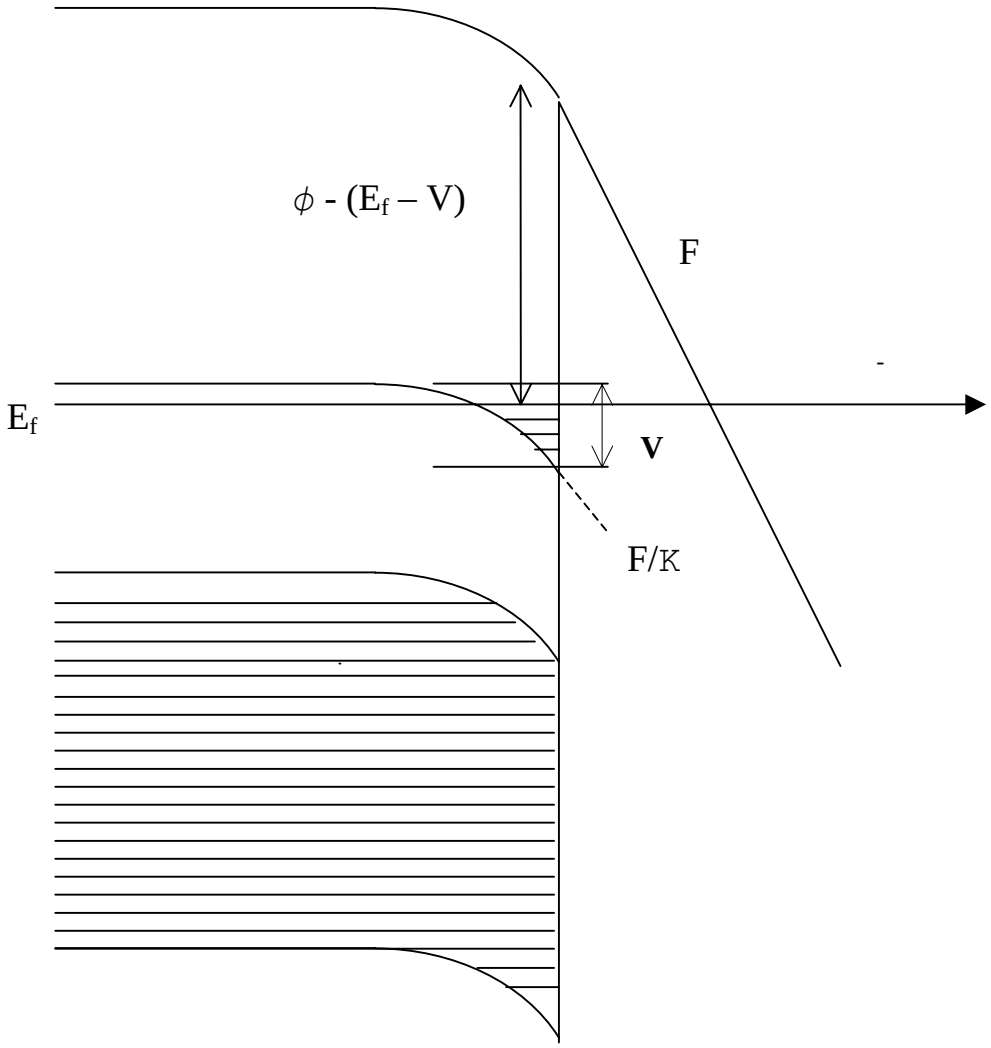

Figure 2.10 Field emission model for the tunneling of electrons from the conduction band of a semi-conductor with dielectric constant K. The external field F penetrates the material and bends the conduction band by V to below the Fermi level E_f . A “metallic” pool of electrons obeying Fermi statistics collects in the depression created.

2.8 Field Emission through Adsorbate States

Another possible mechanism by which carbon nanotubes are thought to field emit, at least at room temperature, is by resonant tunneling of electrons through adsorbate states. The molecule believed involved in this process is water or some type of its derivative such as OH^- radicals [28]. The emission from adsorbed molecules on metal tips is a well studied phenomenon. As Figure 2.11 depicts, the external electric field partially penetrates the adsorbed molecule and deforms its potential energy. The Fermi level of the metal equalizes with the highest filled state of the molecule and a decrease in the effective work function of the molecule results [29]. These adsorbed states thus create a resonant tunneling condition for electrons which increases the local tunneling current at the molecule. These adsorbate states on carbon nanotubes are removed above $900^\circ K$ with an accompanying reduction of the field emission current [28].

2.9 Field Emission from Localized States

As discussed in section 2.3, carbon nanotubes possess discrete peaks in the bulk local density of states. This discontinuity in the electronic structure at the nanotube caps differs from the continuum states of metal emitters. Investigators have also shown that nanotube caps possess distinct local electronic states [30]. This unique local electronic structure is believed to play a role in enhancing field emission current.

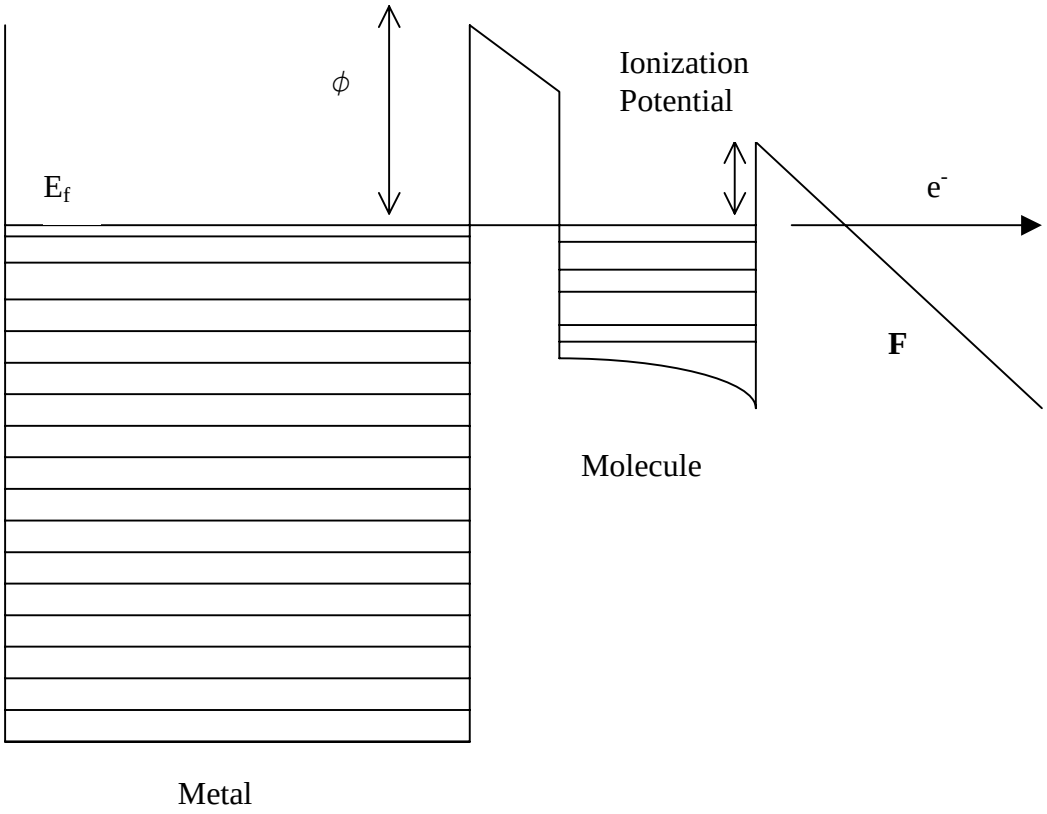

Figure 2.11 Model for the field emission from adsorbate states formed on metal tips. E_f is the Fermi level of the metal with a workfunction ϕ. The external field F lowers the ionization potential of the molecule as well as deforming the potential barrier allowing electrons to tunnel from the molecule.

Recent ab initio pseudopotential electronic calculations of single walled carbon nanotubes in applied fields have shown the presence of unusual localized states at the top of the nanotubes [31]. These states are believed to be responsible for high field emission current by allowing a charge buildup at the end of the nanotubes when an external field is applied. Han and Ihm [31] hypothesize that the accumulated charge on the nanotube caps enhances the local electric field which in terms of the Fowler-Nordheim theory is the driving force of field emission.

Additional importance of the role of localized states has come from the field emission energy distribution (FEED) measurements done on carbon nanotubes. FEED data have shown the presence of tunneling states above the Fermi level in single wall carbon nanotubes [32]. FEED data of multiwall nanotubes also show an energy spread of the electron distribution which is half that of metallic emitters, indicating that the emission of electrons occurs from narrow energy levels [33].

2.10 Auger Electron Spectroscopy

Auger electron spectroscopy (AES) derives its name from the Auger effect first observed by Pierre Auger, a French physicist, in the mid 1920's . Its utility as a technique for surface analysis however wasn't established till much later in the mid 1960's. The first step in the process involves irradiating a surface with a primary beam of electrons. Then a precise measurement is made of the number of emitted secondary electrons as a function of kinetic energy. This helps in identifying the specific element involved in the emission of the Auger electrons.

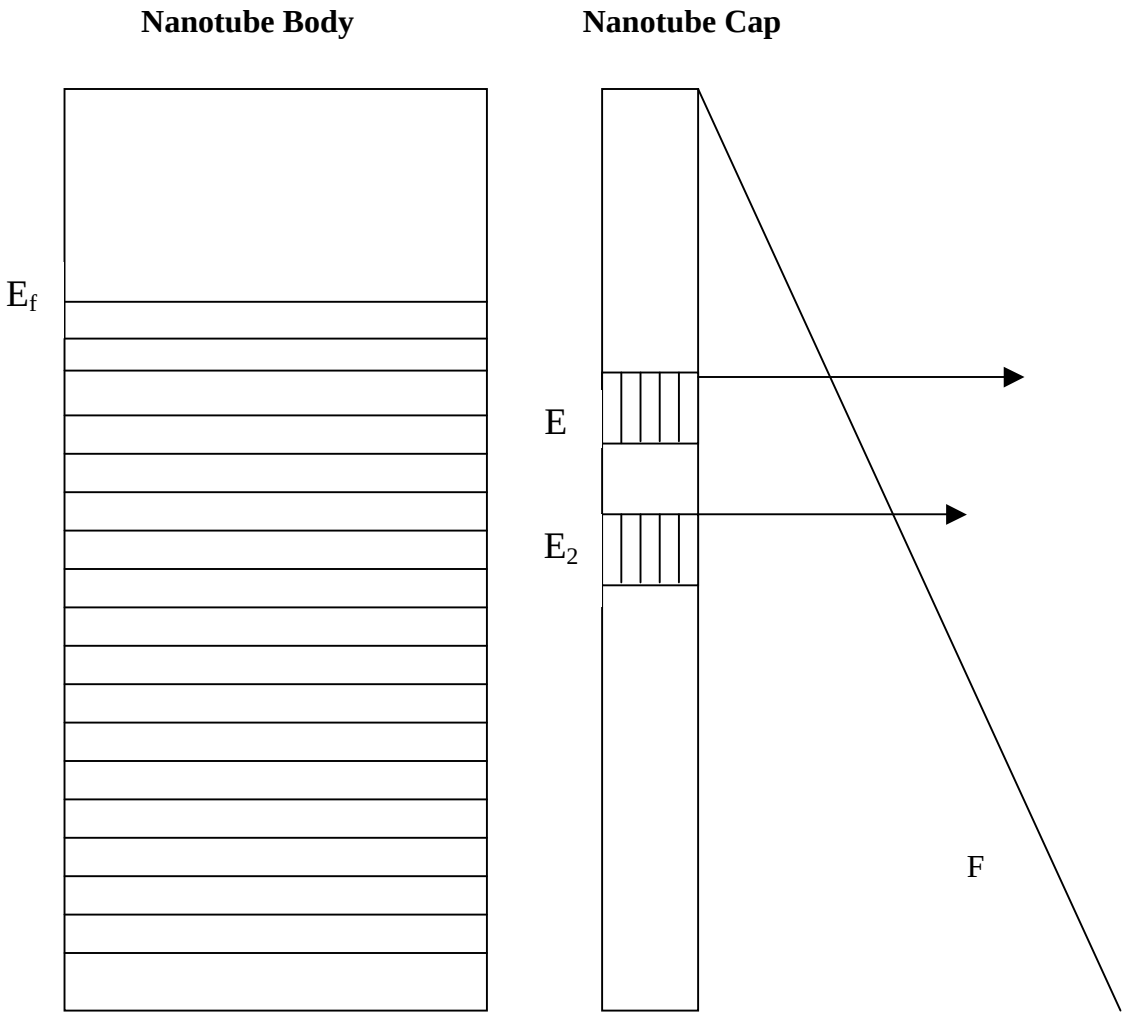

Figure 2.12 Model for Field emission from the localized states E_1 and E_2 located on the cap of carbon nanotubes. Localized states are speculated to exist above the Fermi energy level E_f of the bulk nanotube body as well.

As illustrated in Figure 2.13 a primary beam of electrons ejects an electron from a core 1s ground state of a surface atom. The ion thus formed is unstable and the vacant orbital in 1s is quickly filled by an electron dropping down from a higher level such as a 2s orbital. The energy released in the process can be absorbed by an electron in a higher orbital such as 2p, causing it to be ejected as an Auger electron. The final ion state shown in Figure 2.13 is still not stable and after more electron arrangements the system quickly returns to its ground state. From conservation of energy, the kinetic energy of the Auger electron is

$$E_k = E_{1s} - E_{2s} - E_{2p} \tag{2.26}$$

where the subscripts designate the respective energy levels of the states. This equation is not strictly accurate since the Auger process deals with electrons in ionized states, which will have different energies from the above ground states represented in equation (2.26) [35]. A point to note is that the production of an Auger electron involves at least three electrons . Thus the detection of the elements hydrogen and helium is not feasible.

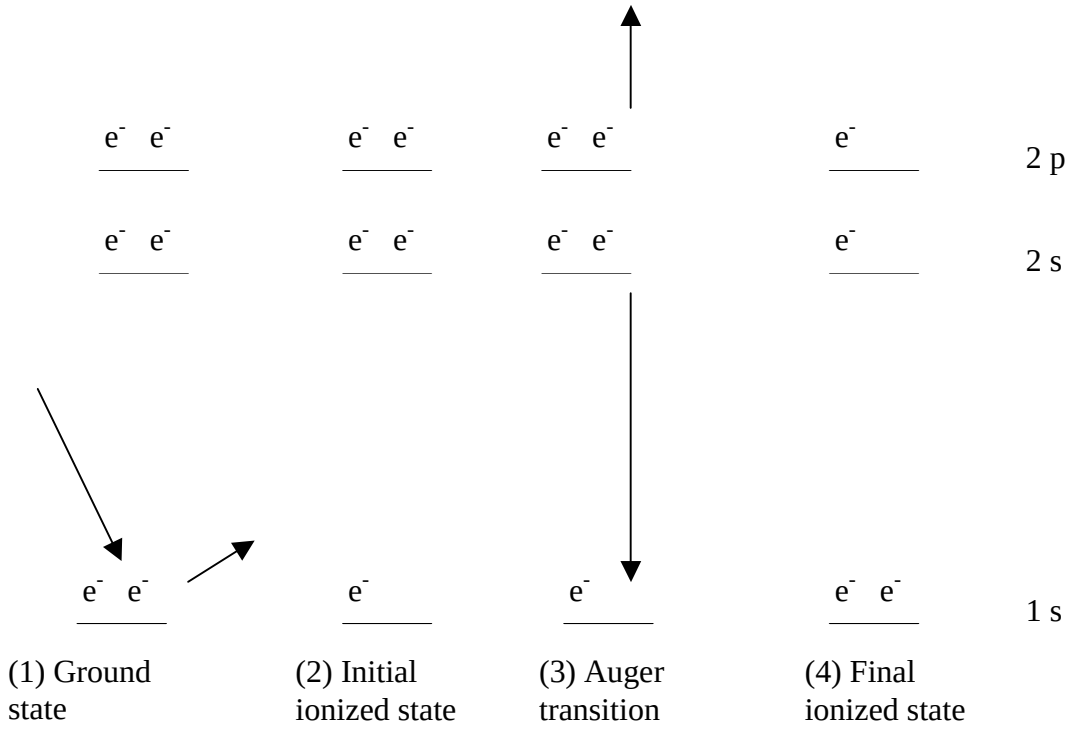

Figure 2.13 Schematic illustration of the Auger process.

REFERENCES

1. O. Zhou, R. M. Fleming, D. W. Murphy, C. H. Chen, R. C. Haddon, A.P. Ramirez, and S. H. Glarum, *Science*, **263** 1744 (1994).

2. S. Amelinckx, D. Bernaerts, X. B. Zhang, G. Van Tendeloo and J. Van Landuyt, *Science*, **267**, 1334 (1995)

3. P. J. F. Harris, Carbon Nanotubes and Related Structures, New Materials for the Twenty-first Century (Cambridge University Press, Cambridge, 1999).

4. J. -M Bonard, H. Kind, T. Stockli and L. -O. Nilsson, *Solid-State Electronics* **45**, 893 (2001).

5. S. Iijima, *Nature*, 354 (1991).

6. D. Bernaerts, M. Op De Beeck, S. Amelinckx, J. Van Landuyt, G. Van Tendeloo, *Phil. Mag. A* ,**74** , 723 (1996)

7. X. F. Zhang, X. B. Zhang, G. Van Tendeloo, S. Amelinckx, M. Op de Beeck, J. Van Landuyt, *J. Cryst. Growth* **3**, 130 (1993).

8. R. Saito, G. Dresselhaus, and M. S. Dresselhaus , Physical Properties of Carbon Nanotubes (Imperial College Press, London, 1998).

9. R. Saito, M. Fujita, G. Dresselhaus, and M. S. Dresselhaus *Phys. Rev. B* **46**,1804 (1992).

10. J. W. Mintmire, B. I. Dunlap, and C. T. White, *Phys. Rev. Lett*. **68,** 631 (1992).

11. J. W. Mintmire, D. H. Robertson, and C. T. White, *J. Phys. Chem. Solids* **54,** 1853 (1993).

12. T. Hamada, M. Furuyama, T. Tomioka, and M. Endo, *J. Mater. Res.* **7**, 1178 (1992).

13. R. Saito, M. Fujita, G. Dresselhaus, and M. S. Dresselhaus. In Electrical Optical and Magnetic Properties of Organic Solid State Materials, MRS Symposia Proceedings, Boston, edited by L. Y. Chiang, A. F. Garito, and D. J. Sandman, page 333, materials Research Society Press, Pittsburgh, PA, (1992).

14. R. Saito, M. Fujita, G. Dresselhaus, and M. S. Dresselhaus, *Appl. Phys. Lett.* **60**, 2204 (1992).

15. R. Saito, G. Dresselhaus, and M. S. Dresselhaus, *J. Appl. Phys*. **73**, 494 (1993).

16. M. S. Dresselhaus , R. A. Jishi, , G. Dresselhaus, D. Inomata, K. Nakao, and R. Saito, *Molecular Materials* **4**, 27 (1994).

17. R. A. Jishi, D. Inomata, K. Nakao, M. S. Dresselhaus and G. Dresselhaus , *J. Phys. Soc. Jpn*. **63**, 2252 (1994).

18. S. Suzuki, C. Bower, Y. Watanabe and O. Zhou, *Appl. Phys. Lett*. **76**, 4007 (2000).

19. P. Delaney, M. D. Ventra, and S. T. Pantelides, *Appl. Phys. Lett.* **75**, 3837 (1999).

20. S. Frank, P. Poncharal, Z. L. Wang, and W. A. de Heer, *Science* **280**, 1744 (1998).

21. P. G. Collins, M. Hersam, M. Arnold, R. Martel, and P. Avouris , *Phys. Rev. Lett.* **86**, 3128 (2001).

22. A. M. Rao, E. Richter, S. Bandow, B. Chase, P. C. Eklund, K. C. Williams, M. Menon, K. R. Subbaswamy, A. Thess, R. E. Smalley, G. Dresselhaus, and M. S. Dresselhaus, *Science* **275**, 187 (1997).

23. D. Bohm, *Quantum Theory* (Prentice-Hall, Englewood Cliffs, 1951).

24. J. S. Blakemore, *Solid State physics* (Cambridge University Press, Cambridge, 1985). pp.192.

25. W. Schottky, *Z. tech. Physik* **14**, 63 (1923).

26. R. H. Fowler and L. W. Nordheim, *electron Emission in Intense electric Fields*, *Proc. Roy. Soc. Ser. A*, **Vol. 119**, 173 (1928).

27. R. Gomer, *Field Emission and Field Ionization* (Harvard University Press, Cambridge, MA 1961).

28. K. A. Dean, P. V. Allen, and B. C. Chalamala, *J. Vac. Sci. Tech*. **B 17** 1959 (1999)

29. R. H. Good and E. W. Meuller, Handbuch der Physik, (Springer, Berlin,1956), vol 21, pg 26.

30. R. Tamura and M. Tsukada, *Phys. Rev. B*. **52**, 6015 (1995).

31. S. Han and J. Ihm, *Phys. Rev. B.* **61**, 9986 (2000).

32. K. A. Dean, O. Groening. O. M. Kuttel and L. Schlapbach, *Appl. Phys. Lett.* **75**, 2773 (1999).

33. J. -M. Bonard, J. -P. Salvetat, T. Stockli, L. Forro and A. Chatelain , *Appl. Phys. A* **69**, 245 (1999).

35. C. N. Banwell and E. M. McCash, Fundamentals of Molecular Spectroscopy (McGraw-Hill Book Company, UK, 1994).

CHAPTER 3

EXPERIMENTAL APPARATUS

3.1 The UHV Preparation Chamber

The first stage of the UHV system is the preparation chamber which serves an essential role in the heating and out-gassing of my carbon nanotube samples. Made entirely with UHV compatible materials it is very important that it not only remove all contaminants out-gassed from the sample during heating but in addition not unintentionally contaminate the sample. Thus its construction of UHV compatible materials as well as all metal flange seals serves this purpose well.

The preparation chamber is equipped with a sixty liter per second turbomolecular pump set at the back. This pump is separated from the chamber by a gate valve which allows for continuous operation of the pump, since shutting down the pump every time the chamber is brought up to atmospheric pressure for sample placement could expose it to possible contamination. Once the sample is placed in the preparation chamber a roughing pump is used for its evacuation. To avoid back diffusion of pump oil, a molecular sieve and a liquid nitrogen cryogenic trap are placed between the mechanical pump and the chamber. Once the chamber has been evacuated, the gate valve separating the turbomolecular pump is opened to bring the pump back on line. However if required the turbomolecular pump can bring down the chamber pressure from atmosphere to 10^{-7} Torr in less than thirty minutes. Also equipped in the chamber are three pressure

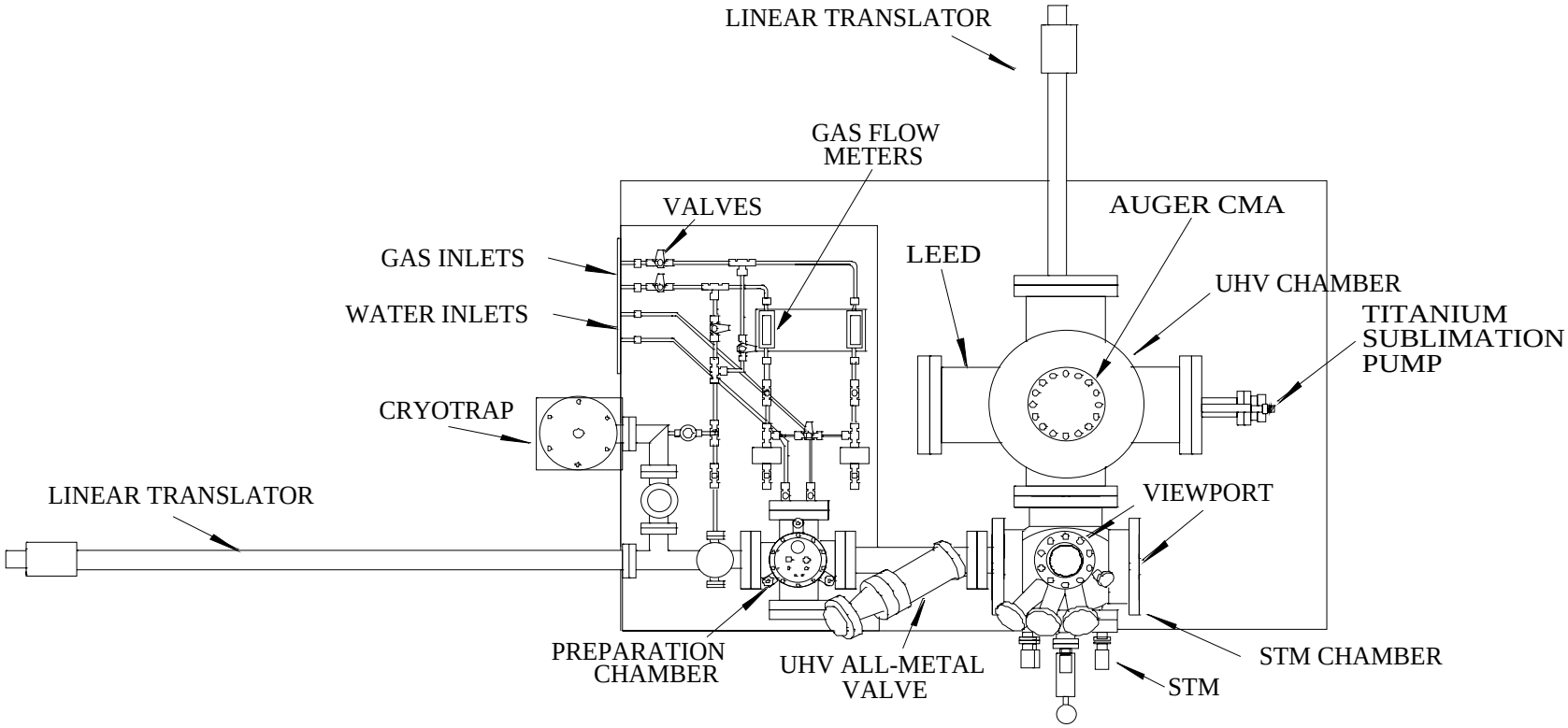

Figure 3.1 Schematic drawing of the top view of the UHV Preparation chamber and the UHV STM system

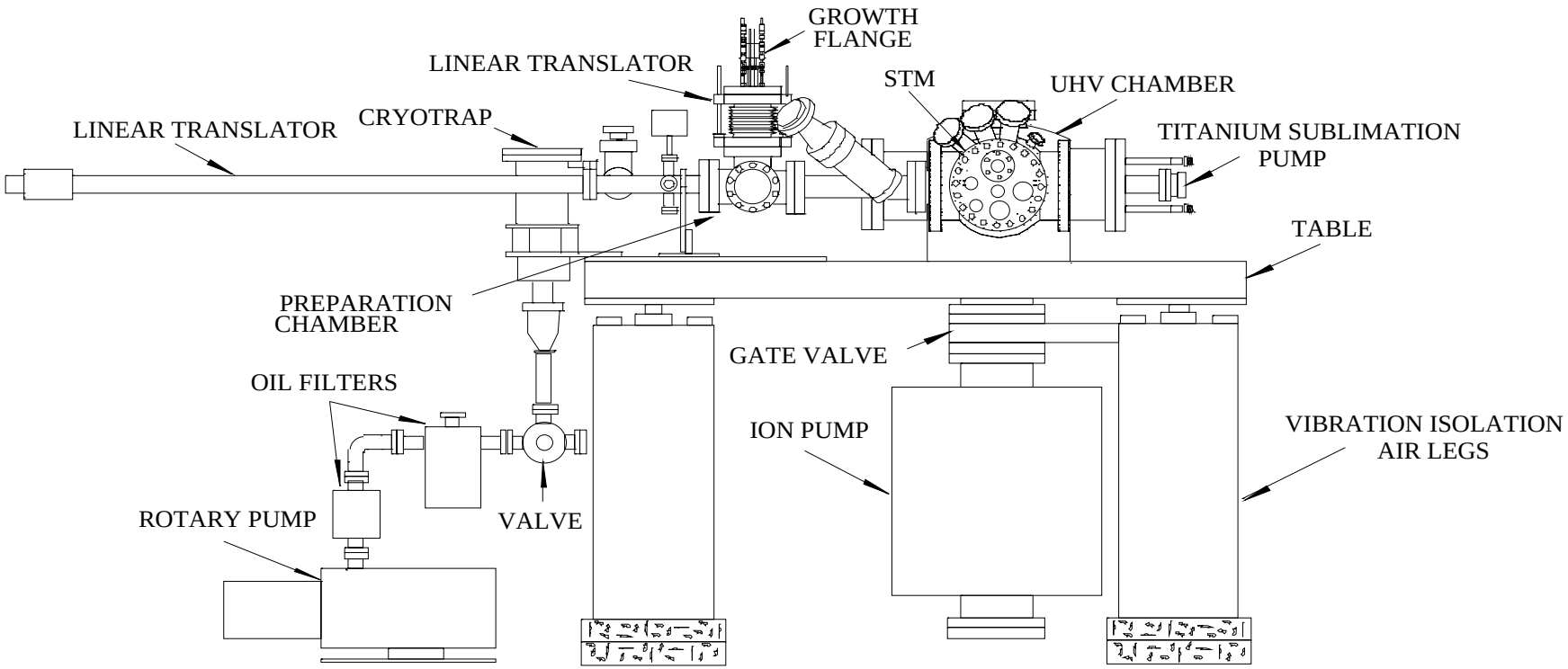

Figure 3.2 Schematic drawing of the side view of the UHV Preparation chamber and the UHV STM system.

gauges: a capacitance Baratron gauge, a thermocouple gauge which is reliable up to 10^{-3} Torr and an ionization gauge which can measure pressure all the way down to UHV. The ion gauge is particularly useful in monitoring the out-gassing from the CNT samples.

Figure 3.3 shows the UHV compatible electrical feed-throughs and water feed-throughs connected to the top flange. The sample holder that is mounted on a linear translator is eased into position to make contact with the electrical feed-through ends. Once in contact, current can be passed through the sample for resistive heating. The water feed-throughs are to cool the sample while the chamber itself is cooled by an external water-jacket during the heating process. The temperature of the sample is measured by placing a digital pyrometer eight inches from the sample and focussed through the view port. Once the sample is ready for transfer, it is translated through an all metal valve into the UHV STM chamber using a linear horizontal translator.

3.2 The UHV System

The main UHV STM chamber was custom built by MDC vacuum products corporation [1]. As the sample is linearly translated into the chamber it is picked up by a rotary arm and can be placed in one of three stages (see Figure 3.4). The first is the experimental stage, the second is the heating stage which is appropriately wired to transmit current to the tantalum clips for heating the sample. The third is an extra stage useful when more than one sample is being analyzed.

An eight inch view port provides a side view into the chamber as shown in Figure 3.5. The least obstructed view into the chamber however is provided by a 4-5/8 inch

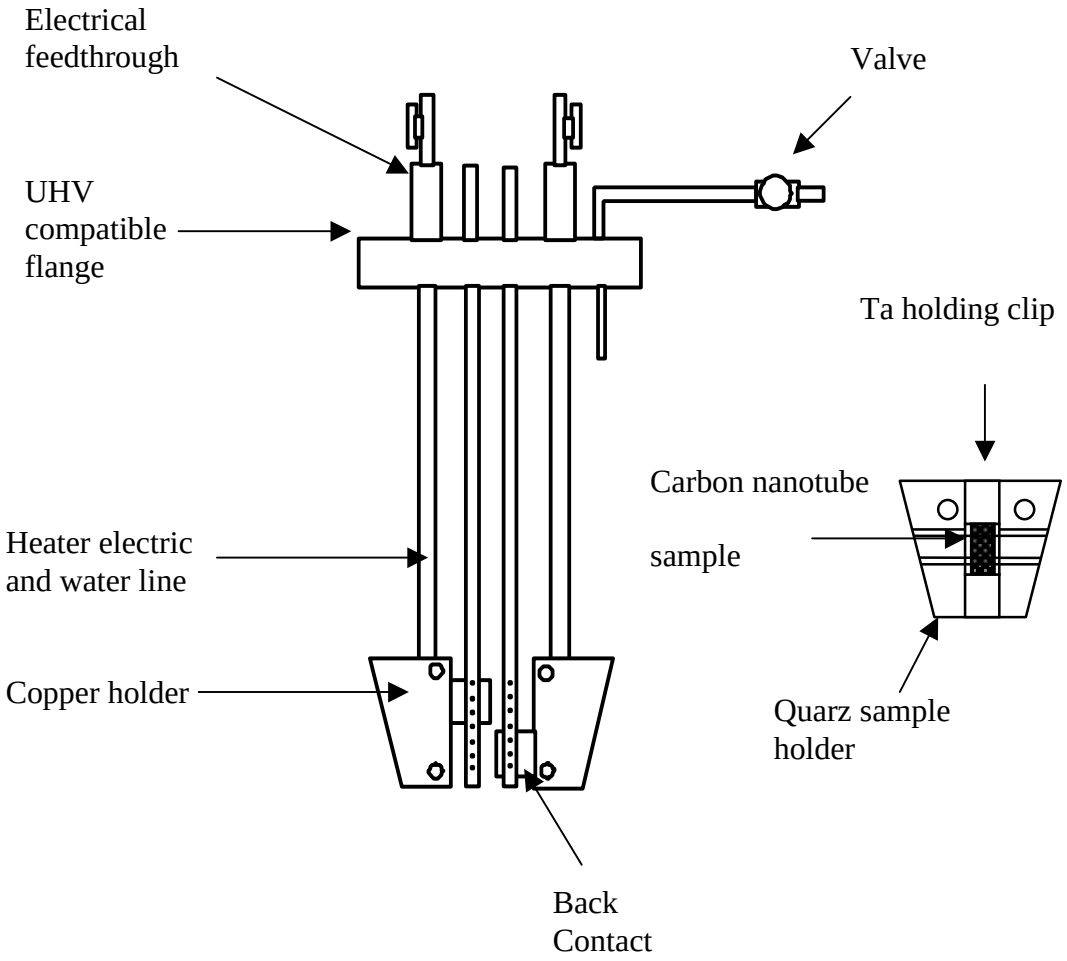

Figure 3.3 Schematic diagram of the sample holder and the sample heating system used for out-gassing of the carbon nanotube samples inside the UHV compatible preparation chamber.

view port located on top of the chamber shown in Figure 3.4. Both these ports are relied upon extensively when manipulating the samples and translators inside the chamber.

Three 2-3/4 inch ports which are angled to focus directly at the center of the heater

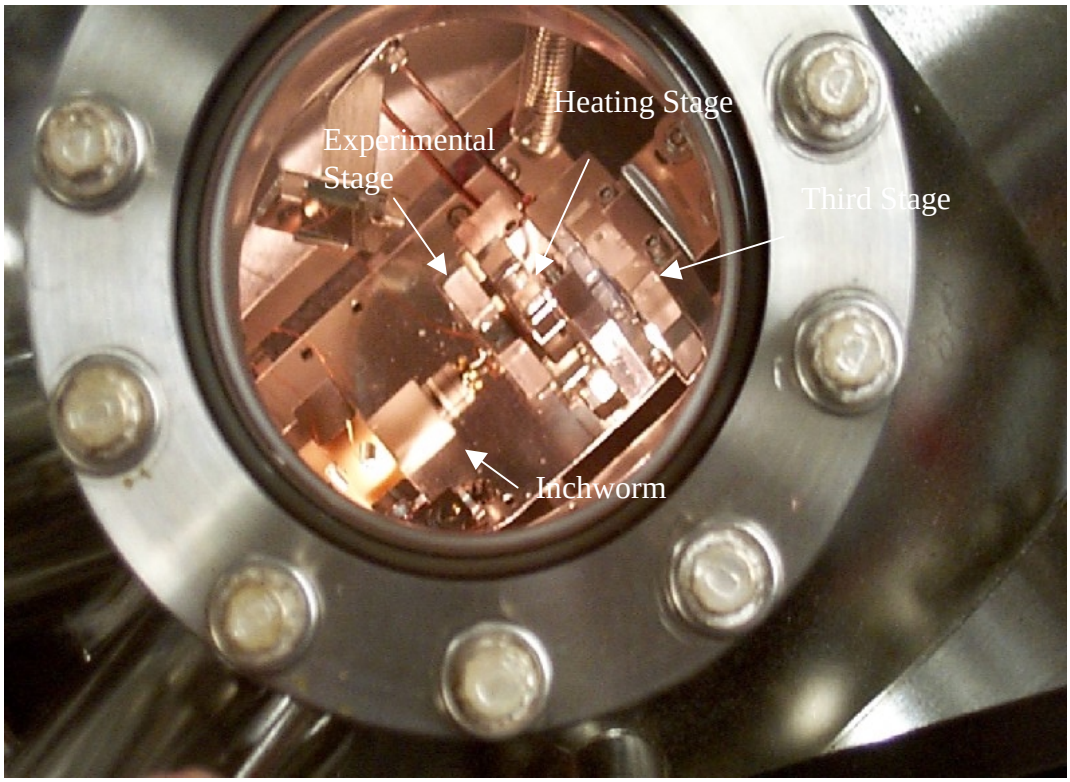

Figure 3.4 View from the top 4-5/8 inch port looking into the UHV STM chamber. The heating stage is used for de-gassing samples in the chamber. The experimental stage is loaded with the quartz holder which has the carbon nanotube film attached to it. The inchworm is used in the coarse approach of the sample.

stage are fitted with sensitive monitoring equipment. One has a residual gas analyzer (RGA) manufactured by Stanford Research Systems which was used to monitor the precise exposure of the nanotube samples to various gases that were leaked into the chamber. The RGA which is essentially a quadrupole mass spectrometer can scan gas species up to 200 atomic mass units (amu) with a resolution of one amu at 10% of peak maximum [2]. The RGA is also used for routine vacuum analysis and leak checking. The other angled port contains an ion sputter gun manufactured by Omicron [3] used for

sputter cleaning and annealing of samples. The third port is used during evaporation of materials onto samples.

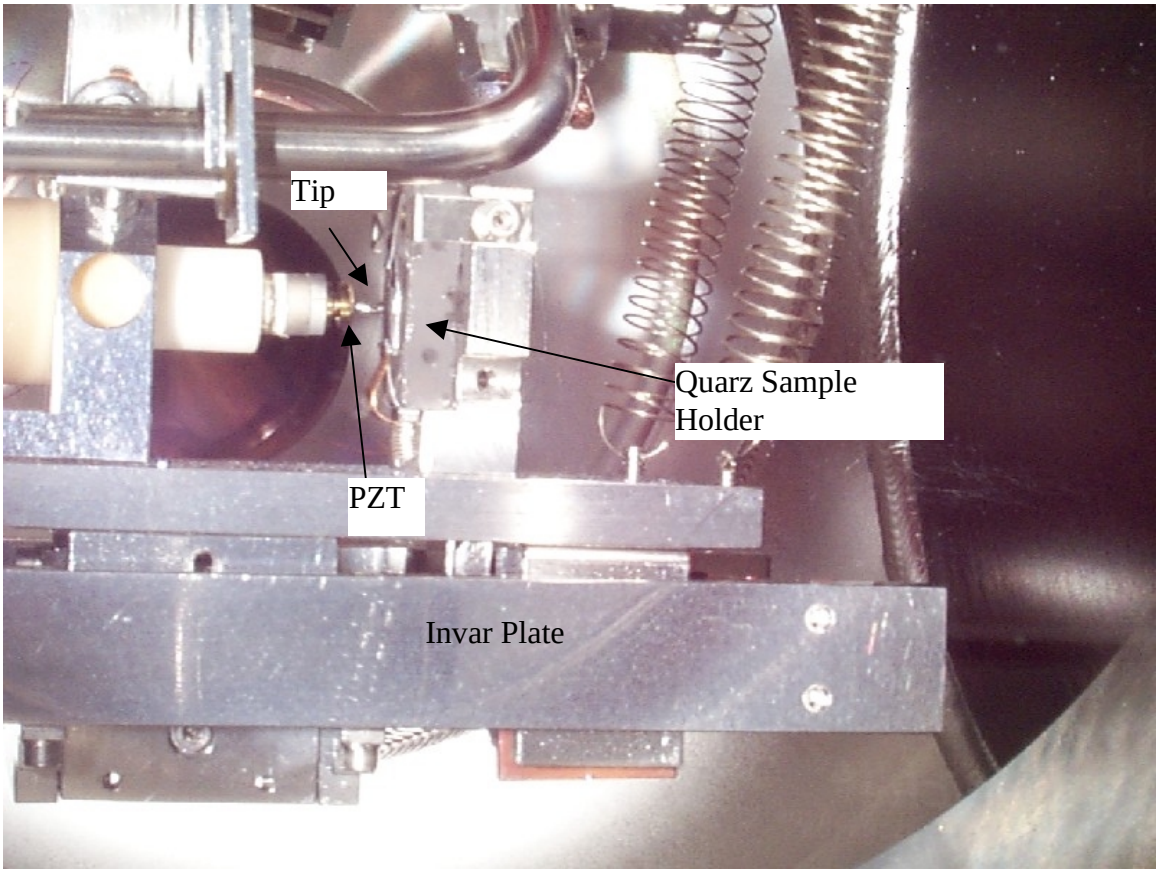

Figure 3.5 Side view from the 8 inch port looking into the UHV STM chamber. The spherical tip is positioned 250 microns from the carbon nanotube sample.

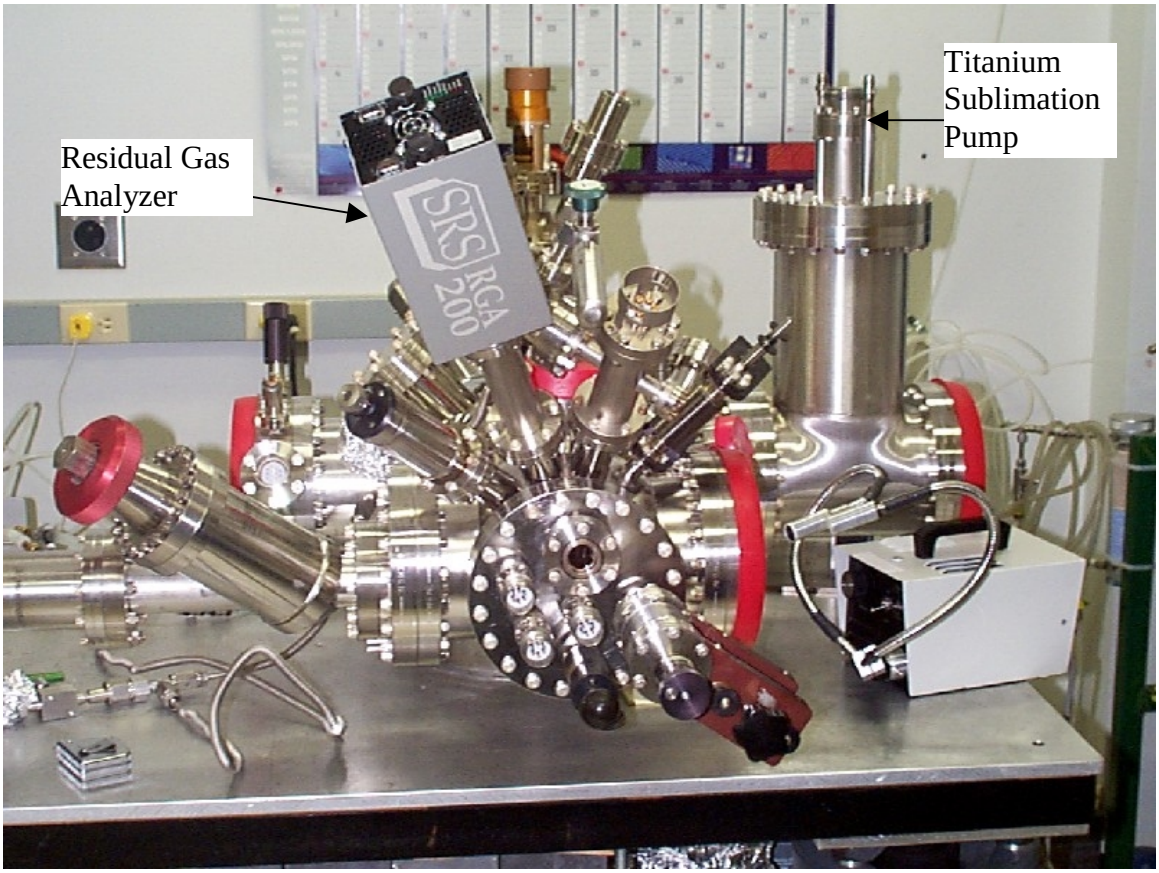

Figure 3.6 View of the STM table showing the Residual Gas Analyzer and Titanium Sublimation Pump.

Attached to the UHV STM chamber described above is the larger main UHV chamber shown in Figure 3.1. This chamber is equipped with a 400 liter per second ion pump which can lower the pressure to below 10^{-10} Torr. In addition a titanium sublimation pump is attached to one of the ports and can be used to quickly bring down the pressure during periods of heavy out-gassing from samples. On the top port of the main chamber

is mounted an Omicron Auger system that consists of a cylindrical mirror analyzer and coaxial electron gun. The Auger system was used to determine the amount of surface contamination on the single wall nanotube sample in the first part of the experiment.

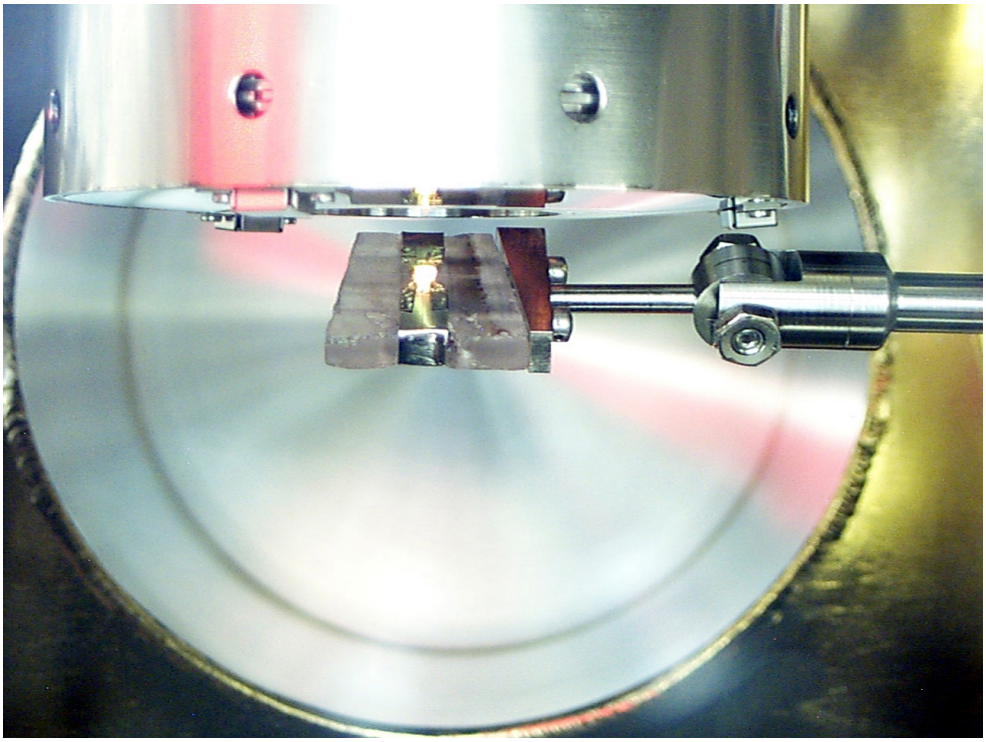

Figure 3.7 Auger electron gun and analyzer performing surface analysis of a sample film.

It was also used to estimate the amount of cesium coverage of the surface of the single wall nanotubes. The UHV chamber is also equipped with several Varian leak valves for precise gas exposure.

3.3 The UHV STM Positioning System

In general, the field emission current is a sensitive function of the anode-nanotube film distance, therefore it is important to precisely position the anode with respect to the film. To achieve this the technology behind the Burleigh instruments Inc. [4] Aris 5000 UHV-compatible STM is used. It consists of two piezo actuators, an inchworm motor and a scanning tube. The inchworm motor is for coarse approach and positions the anode within a few microns from the film. The piezo which is activated by applied voltages is used for fine positioning and is capable of motion in the three x, y, and z directions. The entire assembly sits on an invar base mounted on a vibration isolation system that consists of four springs and four eddy current damping magnet assemblies. The STM experimental stage which is also made of invar holds the carbon nanotube sample as coarse and fine adjustments slowly place the anode tip within tunneling range. Tunneling occurs at about 0.5 – 1.0 nanometres and consists of field emission from the carbon nanotubes into the positively biased anode tip. Once tunneling is detected the tip is retracted using the inchworm alone to the required distance for experimentation. Then the STM is disengaged and separate high voltage electronics are used to measure the FE I-V data. Figure 3.10 shows the schematic for the electrical setup used to take the data. A personal computer controls the digital power supply through a co-axial connection. The power supply positively biases the tip which causes the carbon nanotubes to field emit current. This current is detected by a multimeter and sent to the computer through an IEEE connection. A 600 KΩ ballast resistor is placed in the circuit to act as a current limiter in case of catastrophic failure due to arcing. The labview software is quite

versatile and can take hysterisis curves as well as current versus time data, in addition to the FE I-V curve measurements.

3.4 Cesium Metal Dispenser

Attached through two 2-3/4 inch ports angled into the main UHV chamber are K and Cs metal dispensers purchased from SAES [5]. The reducing agent used in the SAES alkali metal dispensers is the st 101 getter material [5]. Besides its reducing action, the st 101 alloy is able to irreversibly sorb almost all the chemically active gases produced during the reduction reaction, thus preventing them from contaminating the metal vapor. The reducing agent mixture is held in a metal container with a trapezoidal cross-section with a slit to allow for the evaporation of the Cs metal vapor. The dispenser is heated by running current through terminal wires fitted through the port. The heating starts the reduction reaction that subsequently causes the free alkali metal to be evaporated onto the sample.

The Cs evaporation yield of the metal dispensers has been precisely determined by SAES and under the required operating conditions the dispenser yields 28 micrograms (μg) per minute [5,6]. For a sample placed 2 cm from the 2.5 cm long active emitting wire of the dispenser I estimated a deposition density of 1.78 $\mu g/cm^2$ per minute evaporated onto the sample. This calculation was made based on the assumption that the Cs flux at 2 cm from the source can be approximated by a half cylindrical surface. An estimation of the amount of Cs intercalated into the SWNT film which is approximately

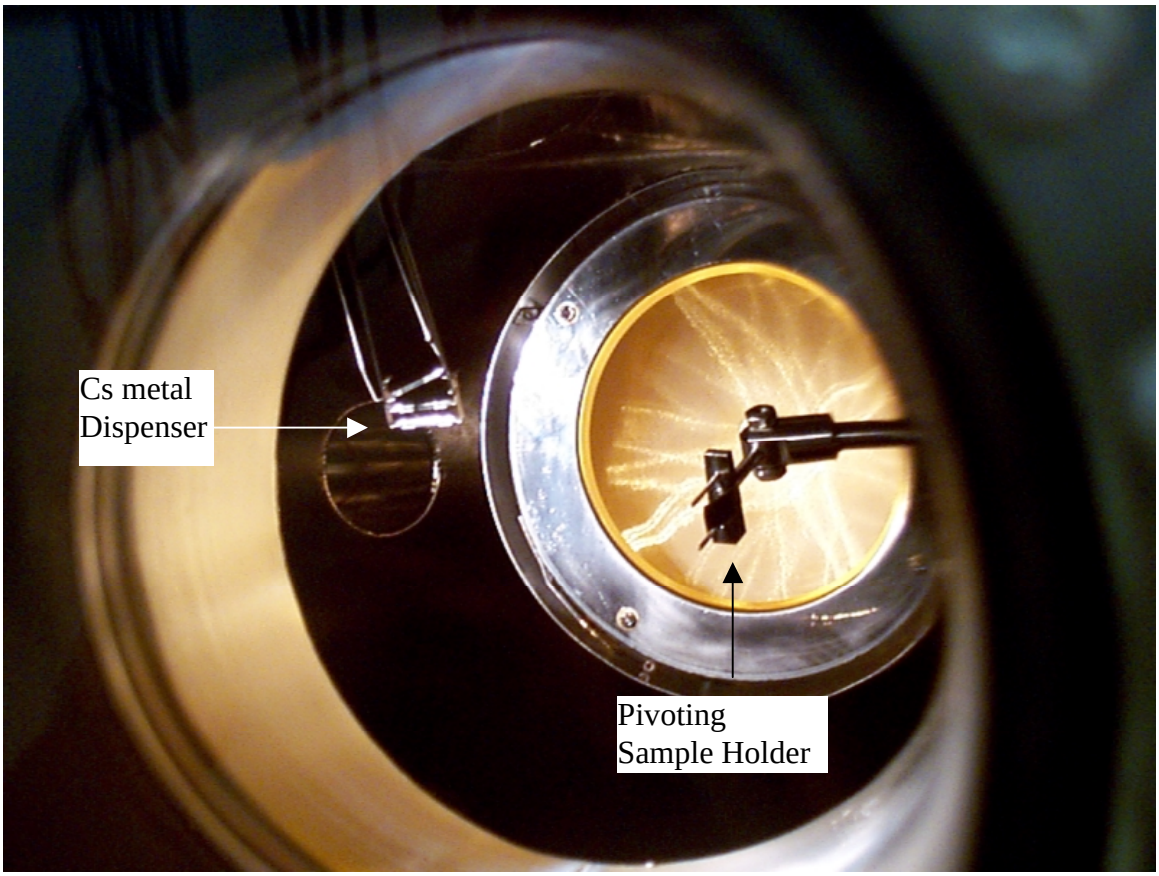

Figure 3.8 View through the 8 inch side port showing the interior of the main UHV chamber. The pivoting sample holder is attached to the end of a linear translator which is used to bring in samples from the UHV STM chamber. The carbon nanotube sample is positioned approximately 2 cm below the Cs metal dispenser for deposition of cesium.

1 cm^2 in area can also be made utilizing the Auger data presented in section 4.6 of chapter 4. The number of carbon atoms in the first two layers (region of Auger analysis) of the SWNT bundles is approximated by treating the SWNT bundles as cylinders lined up adjacent to each other as shown in Figure 3.9. By including only the area on the top half of each cylinder the total area of the film surface increases by a factor of $\pi/2$ to $\pi/2$ cm^2. This area is divided by the area of the unit cell of a graphene sheet shown in Figure 2.4 which contains two carbon atoms. Thus we get a total of 1.17×10^{16} carbon atoms for

the first two layers of the SWNTs. The Auger data shows that after 4 minutes of deposition the surface coverage of Cs is roughly 15%. This amounts to about 1.755×10^{15} Cs atoms which are found to be interspersed within the first two layers of the SWNTs. As mentioned above the SAES getter deposits 7.16μg or 3.226×10^{16} Cs atoms in the 4 minute period. Thus approximately 3.051×10^{16} Cs atoms weighing 6.73 μg either intercalate or "bounce" off the surface. However we can further assume a sticking coefficient close to unity and thus assume a major portion of the deposited Cs does indeed intercalate.

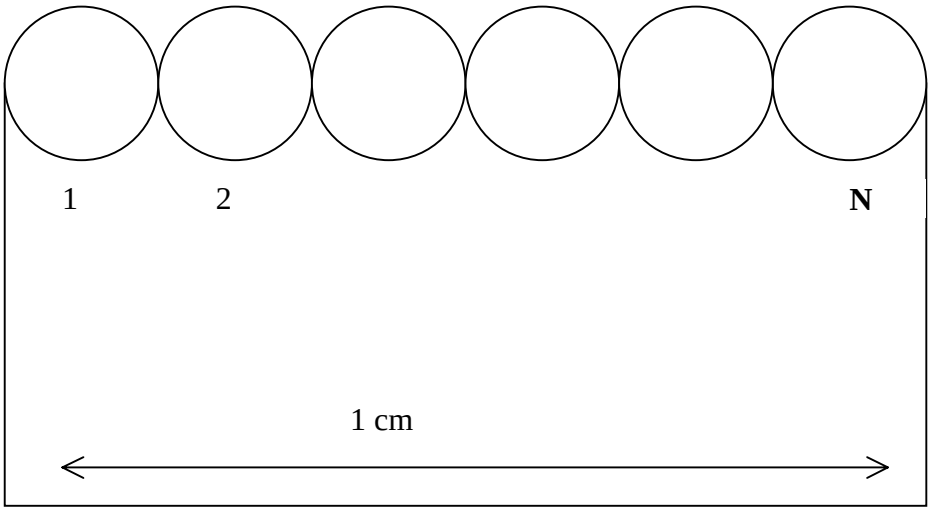

Figure 3.9 Schematic illustration approximating a mat of single wall nanotube bundles. Accounting for the curvature of the cylinders, the surface area becomes $\pi/2$ times greater than that of a flat surface.

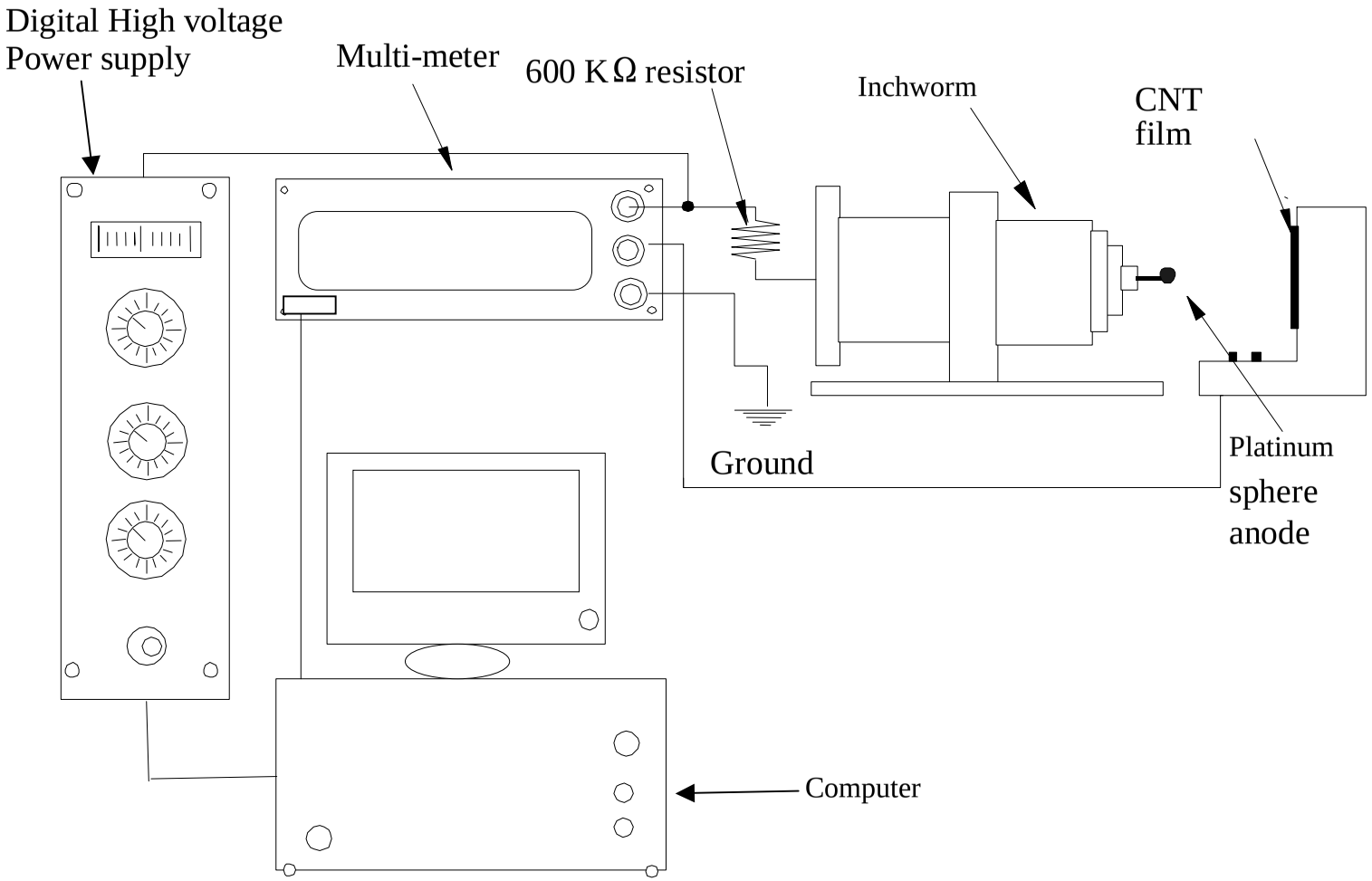

Figure 3.10 Schematic illustration of the electrical system used to acquire field emission data.

3.5 Multiwall Nanotube Growth Setup

The system described in Figures 3.11 and 3.12 was used to produce the MWNTs utilized for the FE analysis in this dissertation. It consists of a glass tube 91 cm in length and having a diameter of 5.65 cm that is placed inside a tube furnace for heating. The entire system can be evacuated to a pressure of 1×10^{-6} Torr using a mechanical rotary pump. Placed strategically at the exhaust end of the glass tube and before the intake of the pump are liquid nitrogen cryogenic traps. These are to prevent the carbonaceous waste products of the CVD process from contaminating the rest of the system, especially the pump. The flow rate of the gasses nitrogen, hydrogen and acetylene used in the growth process are measured in units of standard cubic centimeter per minute (sccm) using digital gas flow meters manufactured by Sierra instruments, Inc. The gas flow itself is controlled by needle meter valves manufactured by Nupro, Inc. The pressure of the system during the growth process is monitored by a Baratron diaphragm capacitance gauge.

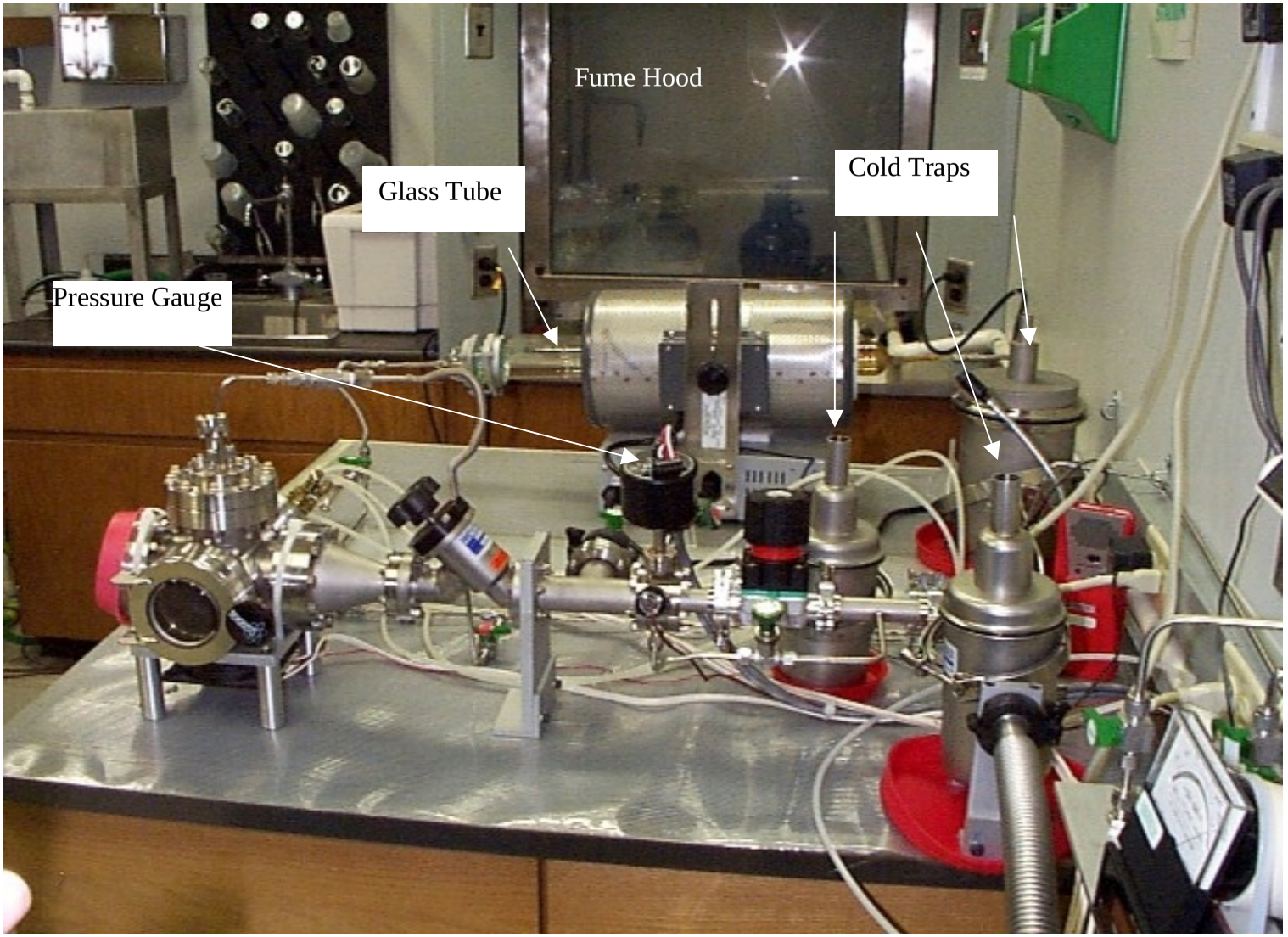

Figure 3.11 Side view of the multiwall nanotube growth setup.

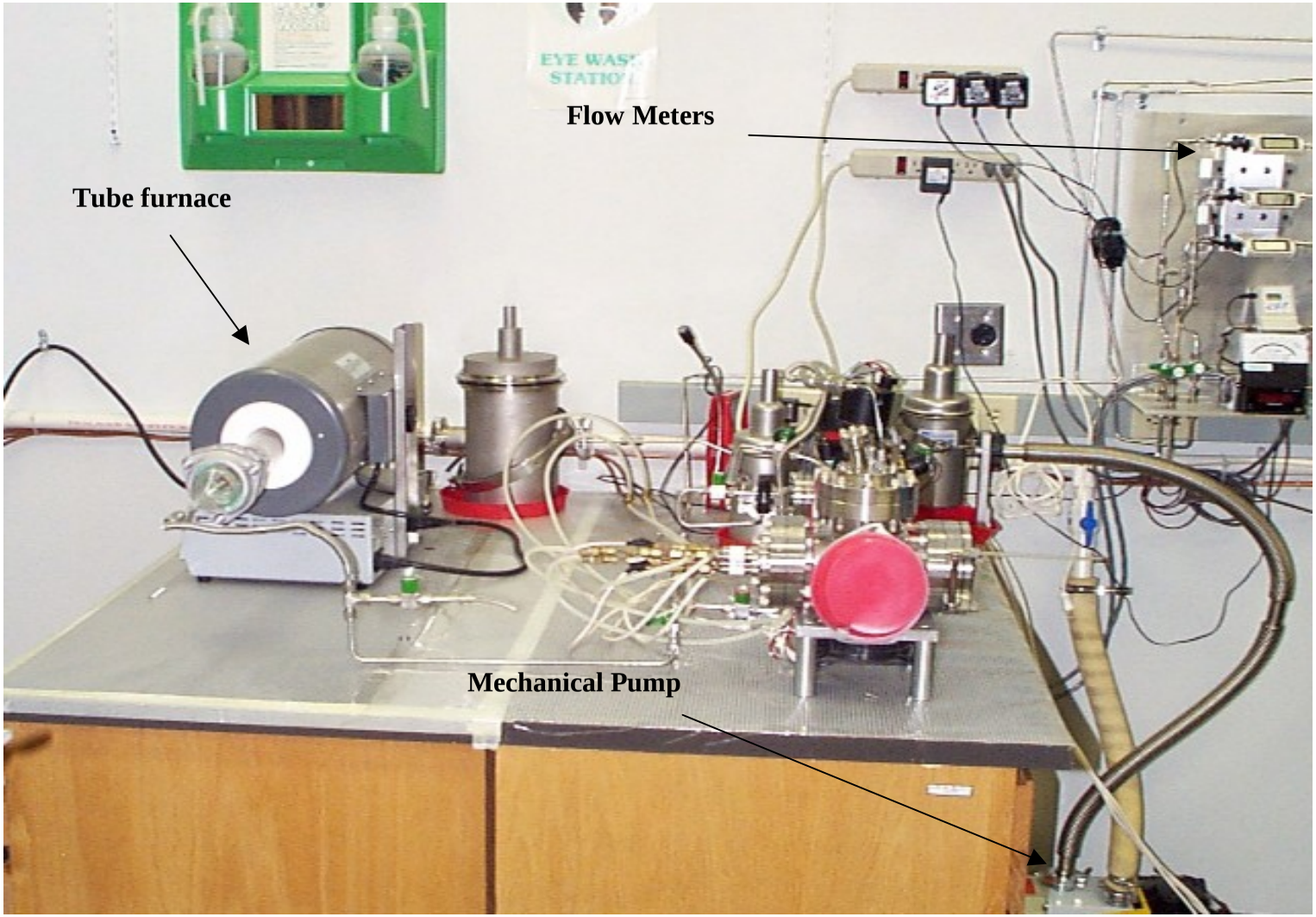

Figure 3.12 Front view of the multiwall nanotube growth setup.

REFERENCES

1. MDC Vacuum Products Corporation, 23842 Cabot Boulevard, Hayward, CA 94545-1651.

2. T. Biernet, J. Begen, and R. Meclewski, *Surf. Sci.* **266**, 11 (1992).

3. Omicron Associates, 1226 Stoltz Road, Bethel Park, PA 15102.

4. Burleigh Instruments, Inc., Fishers, NY 14453.

5. SAES Getters, Inc., Colorado Springs, CO 80906

6. M. Succi, R. Canino, and B. Ferrario, *Vacuum* **35**, 579 (1985).

CHAPTER 4

EFFECTS OF CESIUM DEPOSITION ON THE FIELD EMISSION PROPERTIES OF SINGLE WALL NANOTUBE BUNDLES

4.1 Introduction

Before describing the experiment in detail in section 4.6 a brief history of cesium (Cs) deposition on field emitting materials is presented in section 4.2. Section 4.3 deals with recent experiments that have doped carbon nanotubes (CNTs) with alkali metals, particularly Cs and established the intercalation of the Cs atoms within the CNT structure. Section 4.4 then highlights the effects of the doping on the electronic properties of the CNTs. Section 4.5 deals with the production of single wall nanotubes (SWNTs). I present my results and discuss them in section 4.7 and conclude in section 4.8.

4.2 Cesium Deposition on Field Emitting materials

It has been known for over sixty years that deposited electropositive elements such as Cs can enhance the thermionic and field emission (FE) properties of metal emitters. Indeed the first experiment on a cesiated tungsten emitter that resulted in

enhanced FE was done in 1940 [1]. Since then it has been well established that the workfunction of a metal or a semi-conductor surface is reduced by a partial coverage of Cs [2,3,4]. Using Fowler-Nordhiem (F-N) analysis, Macaulay et al found that Cs deposited on Molybednum micro-cathode arrays reduces the workfunction as well as the operating voltage required for FE.[5]. Diamond films and carbon materials in general have been shown to have improved FE characteristics after deposition of Cs. Pan et al found that cesiation dramatically improved the threshold field and emitter density of diamond like carbon (DLC) films [6]. Chemical vapor deposition (CVD) grown diamond also had its FE properties improved after deposition of Cs [3].

4.3 Doping and Intercalation of Carbon Nanotubes

SWNT bundles grown by catalyst assisted laser vaporization form rope like bundles with a two dimensional triangular lattice [7]. Doping carbon nanotubes with the aim of altering their lattice structure and properties has shown great potential in recent years. Alkali-metals such as Cs, K and halogens like bromine and iodine have been reacted with carbon nanotubes in techniques similar to those used in synthesizing graphite intercalation compounds [8]. MWNTs consist of concentric layers of nanotubes and alkali metal dopants are known to intercalate in between the adjacent shells if defects are present [9,10]. The doping of SWNTs is somewhat different as recent experiments have shown that doping compounds come to reside in between the individual nanotubes within the bundle. An indication that doped SWNTs formed intercalation compounds

came when bulk samples of SWNTs were reacted with vapor-phase bromine or potassium with a resulting forty-fold enhancement in conductivity [11]. The Raman active vibrational modes were also observed to shift after deposition of alkali metals (K or Rb) onto SWNT bundles [12]. Direct structural evidence of intercalation however came only after in-situ transmission electron microscopy (TEM) and electron energy loss spectroscopy (EELS) studies of alkali-metal doped SWNTs were done. TEM revealed that alkali metals such as Cs introduced structural disorder to the lattice structure of the pristine SWNTs with no periodic structure and only weak diffraction spots showing [8]. EELS further established that most of the Cs deposited did not end up just on the surface but intercalated into the bundles [8].

4.4 Effects of Doping on Electronic Properties of Carbon Nanotubes

The transport and electronic properties of doped CNTs are a fascinating area of study. No doubt a major reason for research in this area is the quest for new super-conducting phases in analogy with super-conducting alkali-metal doped graphite and C_{60} [13]. SWNT mats exhibit non-metallic behavior below a certain temperature T and metallic behavior above T [11,14,15,16]. The value for the threshold temperature T varies from 35 K for a single SWNT bundle up to 300 K and higher for mats [15]. Doping of SWNT bundles with either donors or acceptors is expected to shift the Fermi energy in the electronic band structure and can shed light on the electronic conduction mechanism [13]. Indeed, deposition of electropositive elements like Cs or K has been shown to decrease resistance and increase conductivity of SWNTs [11,12,13]. Recent research on

the work function and valence band states of Cs intercalated SWNT bundles was carried out using ultra violet spectroscopy (UPS) [17]. UPS is a powerful tool since it can measure the valence band electronic structure on a wide energy range as well as make a direct measurement of the work function. The work function was found to have decreased from 4.8 eV of the pristine SWNTs to 2.4 eV for the Cs intercalated bundles [17].

4.5 Production of Single Wall Carbon Nanotubes

The SWNT bundles used in the field emission experiment were purchased from Tubes@Rice [18]. These were produced using a laser to vaporize a Cobalt-Nickel target positioned in a flow tube which is kept at 1100°C and has argon gas flowing through it. SWNTs condensed from the laser vaporization plume are swept downstream in the Ar flow and deposit on the quartz tube walls outside the heated zone [19]. The material collected from this process consists of 40-50 vol % of SWNT with the remainder largely being amorphous carbon and residual catalyst particles. This raw material is then treated with a twelve hour 2.6 M nitric acid reflux, followed by rinsing in pH 8.0 water, centrifugation, extraction with toluene, and then a final filtration that results in material consisting of greater than 90 wt % SWNTs [18]. The nanotubes produced are tangled ropes, all single wall with a mean tube diameter of 1.2 nm. It is composed of a nearly random mixture of armchair, zigzag and chiral helicities. While the SWNT ropes are essentially endless they are composed of vast numbers of individual SWNT in Van der Waal contact, with most tubes being 0.2 to 2 microns in length.

4.6 Experiment

The slurry of SWNT bundles in toluene was deposited onto a conducting Si substrate and allowed to dry resulting in a mat of approximately 10 microns thickness as measured by an optical microscope. The Si wafer was then secured onto a quartz holder using tantalum clips as shown in Figure 3.3. The sample was then placed in the UHV compatible preparation chamber for out-gassing as described in chapter 3. It was heated to 500 °C with the temperature measured by a digital pyrometer. The fluctuating pressure due to the out-gassing was monitored with an ionization gauge and after almost 24 hours the sample was ready for transfer. It was then linearly translated through an all metal valve into the UHV-STM chamber. From the UHV-STM chamber it was further translated into the adjoining main UHV chamber which is equipped with an Auger spectroscopy system as well as a Cs metal dispenser as described in section 3.4 of chapter 3. In the main UHV chamber Auger spectroscopy was performed on the sample using an electron beam current of 2 nA to prevent any sample damage. The Auger spectroscopy revealed that the nanotube sample did not have any surface contaminants so the sample was transferred back to the STM chamber for FE current-voltage (*I-V)* measurements. After I-V measurements the clean sample is moved back to the main UHV chamber and positioned 2 cm below a Cs metal dispenser. Cs is deposited for a period of 1 minute and then the sample is transferred once again to the STM chamber for I-V measurements. Then the anode tip is positioned at a separation of 20 microns as described in section 3.3 and FE *I-V* data acquired.

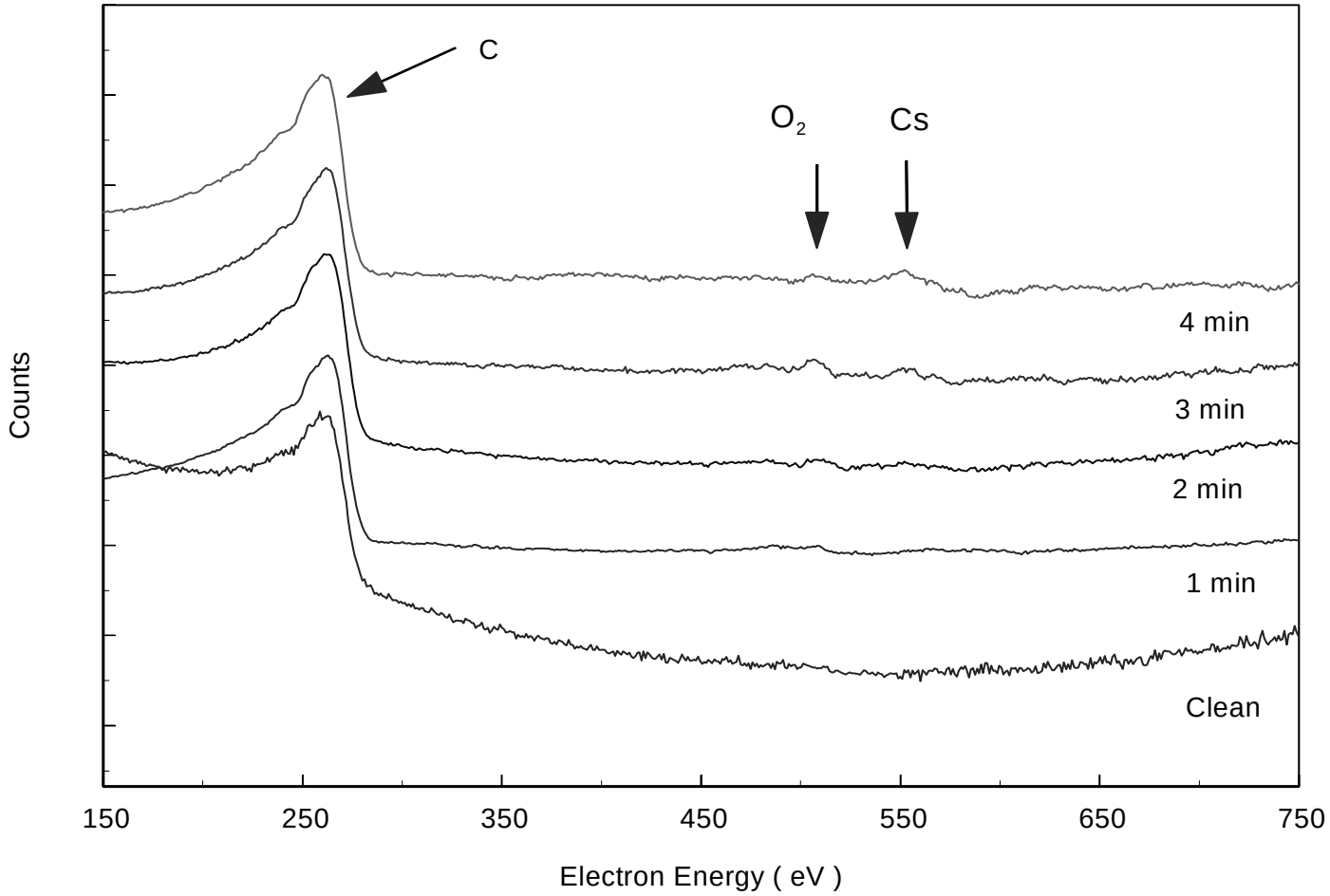

Figure 4.1 Auger spectra of the single wall carbon nanotube sample showing the results of cesium deposition

Then the tip was retracted to place it at a separation of 75μm, 150μm, and 250μm and the measurements repeated. The anode was positioned over approximately the same area of the SWNT sample each time. After the I-V data was taken Auger spectroscopy was performed to determine the amount of Cs on the film. This procedure was repeated 4 times resulting in FE *I-V* curves after total Cs deposition times of 1,2, 3 and 4 minutes. The Auger data are presented in Figure 4.1 with the background subtracted from the graphs to allow for accurate measurement of peak areas. The peak areas were measured in preference to the peak to peak heights of the derivative since the peak areas provide for a more accurate quantitative analysis [20]. The ratio of the Cs to carbon peak in the Auger spectra was 0.02, 0.06, 0.10 and 0.14 after 1, 2, 3, and 4 minutes of exposure, respectively. From these values, the surface concentration of Cs was estimated to be 3%, 6%, 11%, And 15%, respectively, using standard procedures outlined in the Handbook of Auger Electron Spectroscopy [21]. Once FE *I-V* data were acquired a new area of the sample was appropriated for the gas exposure part of the experiment. The anode was positioned at a distance of 250 microns from the film and nitrogen and oxygen gases introduced to a pressure of 10^{-7} Torr. The exposures were for a period of six hours as current versus time data were acquired.

4.7 Results and Discussion

Figures 4.2 - 4.5 show FE *I-V* curves obtained as described above for anode to sample separations of 250, 150, 75 and 20 microns respectively. The data in these graphs

are plotted $\ln(I/V^2)$ vs $1/V$ to allow comparison with the straight-line behavior predicted for FE by the F-N equation. The inset in Figures 4.2 - 4.5 show the corresponding *I-V* curves plotted using a log-linear scale. The small current on the order of 5×10^{-13} A observed below the threshold voltage for FE in these graphs is due to leakage across the connectors. The observed FE current has a weak dependence on the anode to film distance *d*, consistent with geometric local field enhancement. For example, for the clean sample the threshold voltage for FE decreases from approximately 192 V to 83 V as *d* changes by over an order of magnitude from 250 μm to 20 μm. This effect is even more pronounced after the sample has been exposed to Cs for 4 minutes. The threshold voltage for FE then decreases from approximately 92 V to 36 V as *d* changes by over an order of magnitude from 250 μm to 20 μm.

In Figure 4.2 for the 250 micron distance after the 1 minute Cs deposition the threshold voltage decreases from 192 V to 136 V a decrease of almost 30%. The FE current at 208 V increases by almost 6 orders of magnitude from 7×10^{-12} A to 6.5×10^{-9} A. Table 4.1 lists the turn-on voltages and the FE current emitted at 208 V for the 250μm distance. The subsequent depositions at 2,3 and 4 minutes do not see such a dramatic change in either the threshold voltage nor the FE current. Instead we have a more gradual shift of the FN curves for the 2, 3, and 4 minute deposition curves. This behavior is seen in the 150 micron and 75 micron graphs as well shown in Figures 4.3 and 4.4, respectively. Tables 4.2 and 4.3 list the turn-on voltages and the FE current emitted at 194 V and 177.5 V for the 150μm and 75μm distances, respectively.

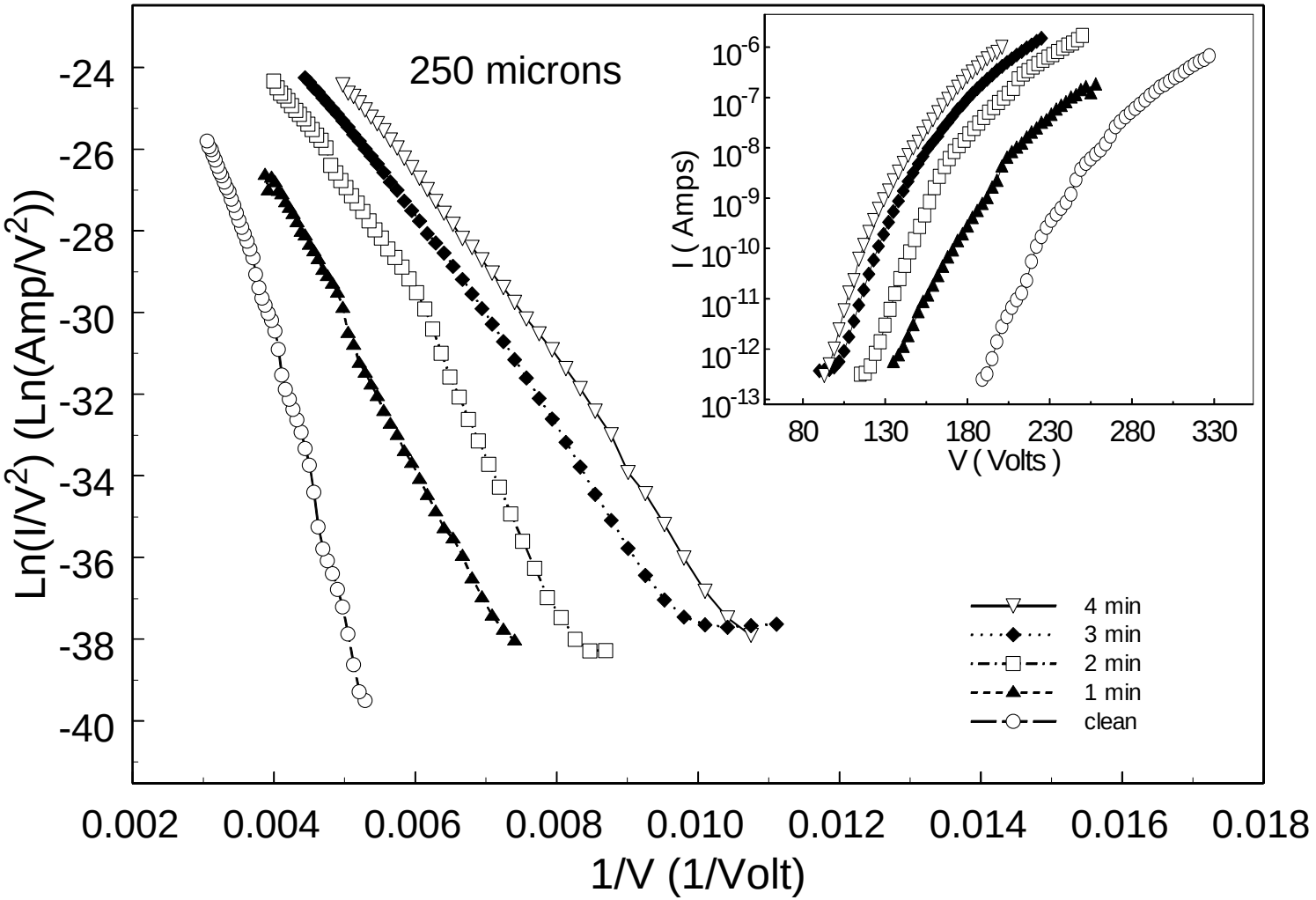

Figure 4.2. Field emission data from a film of single wall nanotube bundles for a film that is clean and exposed to Cs for 1, 2, 3, and 4 minutes. The data are plotted to allow comparison with the Fowler-Nordheim model. The measurements are taken at anode-film distance d = 250 μm The inset shows a plot of the field emission current versus voltage using a log-linear scale.

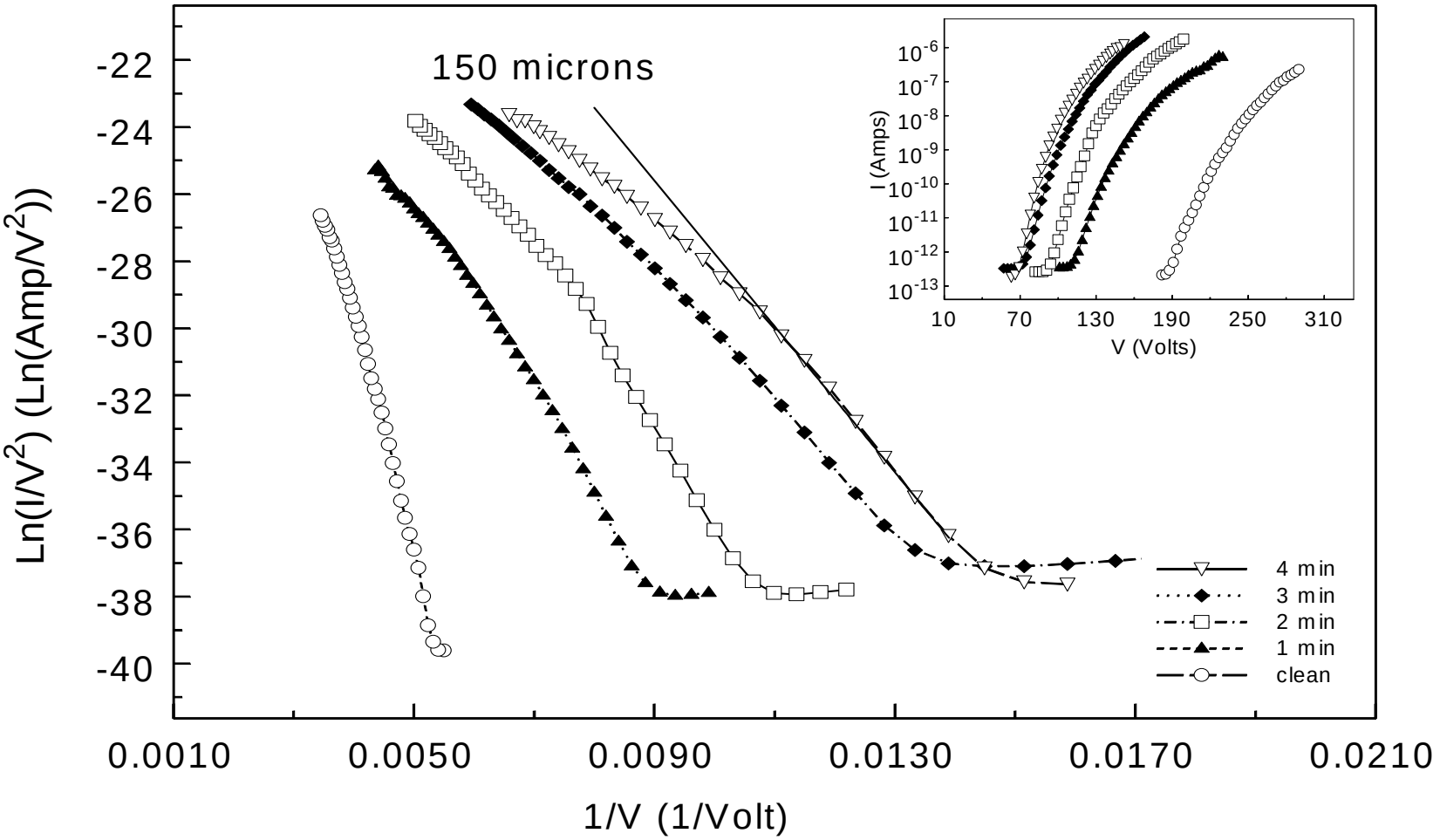

Figure 4.3. Field emission data from a film of single wall nanotube bundles for a film that is clean and exposed to Cs for 1, 2, 3, and 4 minutes. The data are plotted to allow comparison with the Fowler-Nordheim model. The measurements are taken at anode-film distance of d = 150 μm. The straight-line fit shows the departure from Fowler-Nordheim behavior at large currents. The inset shows a plot of the field emission current versus voltage using a log-linear scale.

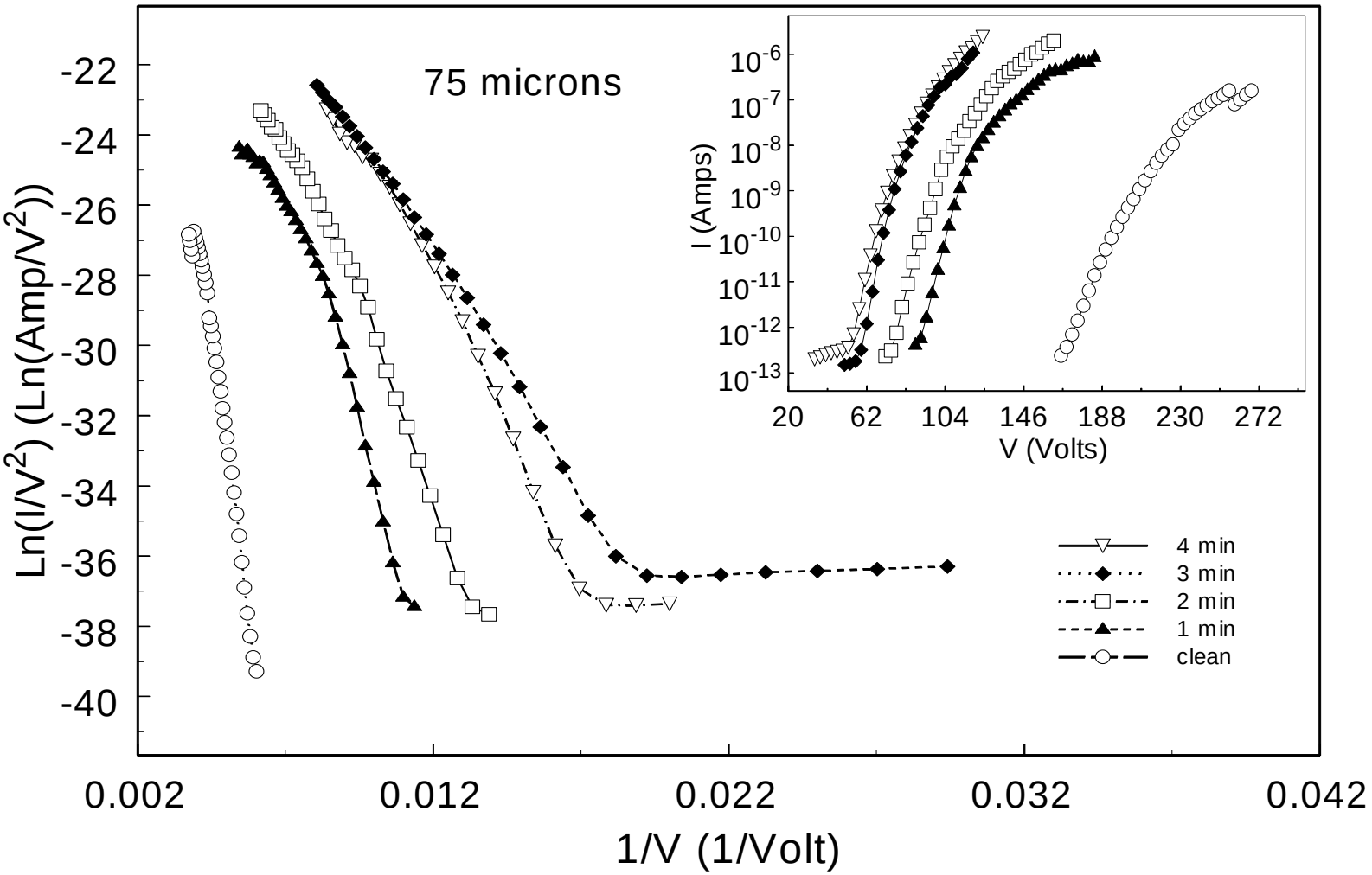

Figure 4.4. Field emission data from the film of single wall nanotube bundles that is clean and exposed to Cs for 1, 2, 3, and 4 minutes. The data are plotted to allow comparison with the Fowler-Nordheim model. The measurements are taken at anode-film distance of d = 75 μm. The inset shows a plot of the field emission current versus voltage using a log-linear scale.

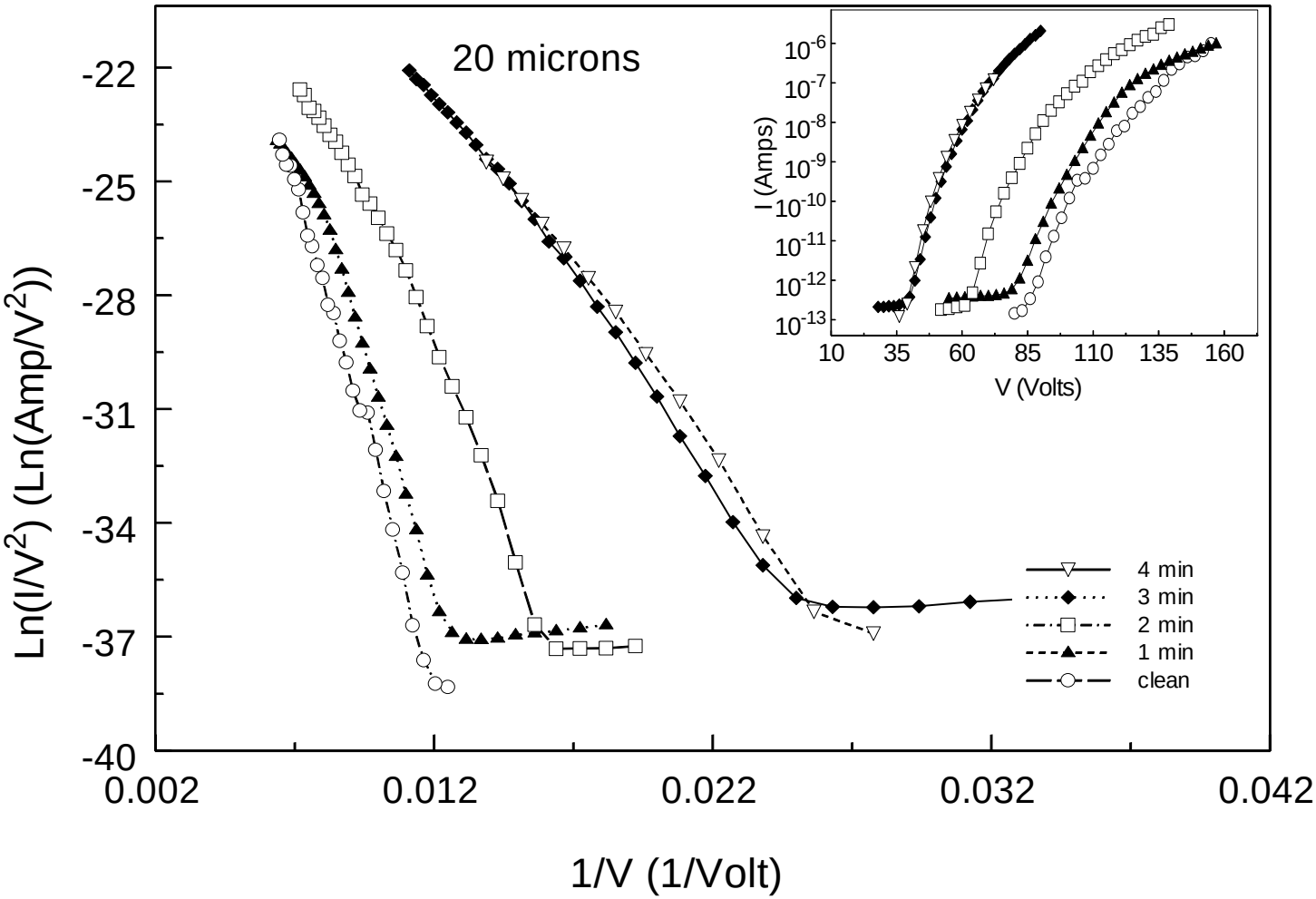

Figure 4.5. Field emission data from the film of single wall nanotube bundles that is clean and exposed to Cs for 1, 2, 3, and 4 minutes. The data are plotted to allow comparison with the Fowler-Nordheim model. The measurements are taken at anode-film distance of $d = 20\ \mu$m. The inset shows a plot of the field emission current versus voltage using a log-linear scale.

It is interesting to note that in Reference 17 a rapid shift in the Fermi level was also noted after the first Cs deposition followed by more gradual movement in subsequent depositions. They attributed this to an increase in the density of states at the Fermi level caused by the Cs intercalation.

In Figure 4.5 for the 20 micron graph, the "clean" and "1 min" curves almost overlap. Similarly for the 75 micron graph the "3 min" and "4 min" curves are transposed. Such anomalies are not seen for the larger distances of 150 microns and 250 microns leading to the hypothesis that the shorter distances are susceptible to the film's local surface morphology. That is, changes in the surface during the normal course of the experiment would have a greater effect on the shorter distances. This could be

Deposition Time	Threshold Voltage at 250μm	FE current at 208 Volts
0 minutes	192 V	7×10^{-12} A
1 minute	136 V	6.5×10^{-9} A
2 minutes	120 V	1.5×10^{-7} A
3 minutes	104 V	5×10^{-7} A
4 minutes	92 V	1.5×10^{-6} A (extrapolated)

Table 4.1 FE data for the single wall nanotube at a film-anode separation of 250 μm.

Deposition Time	Threshold Voltage at 150μm	FE current at 194 Volts
0 minutes	186 V	1.5×10^{-12} A
1 minute	113 V	8×10^{-8} A
2 minutes	94 V	1×10^{-6} A
3 minutes	74 V	9×10^{-6} A (extrapolated)
4 minutes	66 V	1.5×10^{-5} A (extrapolated)

Table 4.2 FE data for the single wall nanotube at a film-anode separation of 150 μm.

Deposition Time	Threshold Voltage at 75μm	FE current at 177.5 Volts
0 minutes	166 V	2×10^{-12} A
1 minute	88 V	5×10^{-7} A
2 minutes	73 V	3×10^{-6} A (extrapolated)
3 minutes	54 V	1×10^{-4} A (extrapolated)
4 minutes	58 V	4×10^{-5} A (extrapolated)

Table 4.3 FE data for the single wall nanotube at a film-anode separation of 75 μm.

Deposition Time	Threshold Voltage at 20 μm	FE current at 90 Volts
0 minutes	83 V	1.5×10^{-12} A
1 minute	78 V	2×10^{-11} A
2 minutes	62 V	7×10^{-9} A
3 minutes	40 V	1.5×10^{-6} A
4 minutes	36 V	2×10^{-6} A (extrapolated)

Table 4.4 FE data for the single wall nanotube at a film-anode separation of 20 μm.

compounded by the fact that the data for the farther distances was taken later in time possibly after the surface had "settled" somewhat more.

At low currents, the *I-V* curves show good agreement with the straight-line behavior predicted by the F-N equation. At larger currents, the *I-V* curves of the samples exposed to Cs show a departure from straight-line behavior towards smaller slope, as shown by the straight-line fit in Figure 4.3. This current saturation effect is not observed for the clean nanotube sample, which agrees well with the F-N equation even at high currents. A similar saturation effect has been observed in the FE *I-V* curves of single wall nanotubes at a pressure of 10^{-7} Torr [22,23] and attributed to a current and field-induced decrease in tunneling from adsorbate states [23]. In Reference [23] the adsorbates are due to H_2O in the vacuum container, and after high FE currents they observe a decrease in FE current and return to F-N behavior due to desorption of the adsorbates. Our experiments

are performed in UHV and the saturation effect is not observed in the clean sample. The saturation effect initially appears after the first Cs deposition. As the Auger results indicate, there is some deposition of O_2 along with the Cs on the nanotube surface. The O_2 probably comes from the trace oxygenic gases released during the evaporation of Cs. Thus I conjecture that the saturation effect is due to the presence of adsorbates such as Cs and O_2. We ran the SWNT emitters at high currents (10^{-6} A), yet did not observe a permanent decrease in FE current and permanent return to F-N behavior in the *I-V* curves shown in Figures 4.2-4.5, showing that the Cs adsorbates are robust and not desorbed.

The F-N equation shows that the value of $b\phi^{3/2}/\beta$ can be determined from the slope of the $\ln(I/V^2)$ vs. $1/V$ curve. Assuming that β remains the same, the ratio of the work function before and after Cs deposition can be determined from the ratio of the slope before and after deposition [5,24] We measure the slope of the straight-line behavior at low currents in the FE *I-V* curves shown in Figures 4.2-4.5. From these measurements, the ratio of the slope for the clean sample and the slope for the sample exposed to Cs for 4 minutes is found to be 1.8, 2.2, 2.5 and 2.0 for film – anode separations of 250, 150, 75 and 20 μm, respectively. It is interesting to note that the average of these values is 2.1 ± 0.3, in good agreement with the value of 2.0 for the ratio of the work function of SWNT bundles before and after Cs deposition measured using ultraviolet photoemission spectroscopy in Reference 17.

If cesiated carbon nanotubes are to be considered for potential applications as FE sources, it is important that their performance and stability be tested under UHV and gaseous environments. We studied the effects of N_2 and O_2 gases on the FE properties of

the SWNT bundles exposed to Cs for 4 minutes at *a* film – anode separation of 250 μm. The choice of O_2 as a test gas is quite obvious if one considers the prevalence of oxygen and its derivative oxygenic gases in most vacuum environments. Add to this the reactivity of O_2 and it becomes crucial to understand the effects of the exposure of the cesiated carbon nanotubes to this gas. The addition of N_2 as a test gas compliments my study quite well since N_2 is not as reactive a gas as O_2 but has a mass quite close to O_2. This allows us to distinguish between the damage done by sputter etching – an effect attributable to heavy gases [25] – and surface chemical reactions.

Figures 4.6 - 4.8 show the FE current as a function of time in UHV, and during exposure to N_2 and O_2 at 10^{-7} Torr for 6 hours for a total exposure of approximately 2167 Langmuir (L). Figure 4.6 shows that the FE current does not decrease in UHV. Figure 4.7 shows that upon introduction of N_2 there is an increase in fluctuation of the FE current. However, the FE current does not decrease in magnitude during the exposure. Figure 4.8 shows the initial current of the SWNTs at 6 nA which required 150 V. Exposure to 2167 L of O_2 then decreases the FE current by 75 % to approximately 1.5 nA. This should be compared to the results of Figure 5.9 in chapter 5 where the SWNT bundles were exposed to 6500 L while operating at 4μA. Previous research has shown that changes in FE characteristics in a gaseous environment are directly proportional to the FE current of the emitter [26,27]. Thus it is not surprising that the SWNT bundles in Figure 5.9 suffer greater current degradation than the cesiated SWNT bundles. But what stands out is that the cesiated SWNTs only partially recover whereas the results in Figure 5.9 show

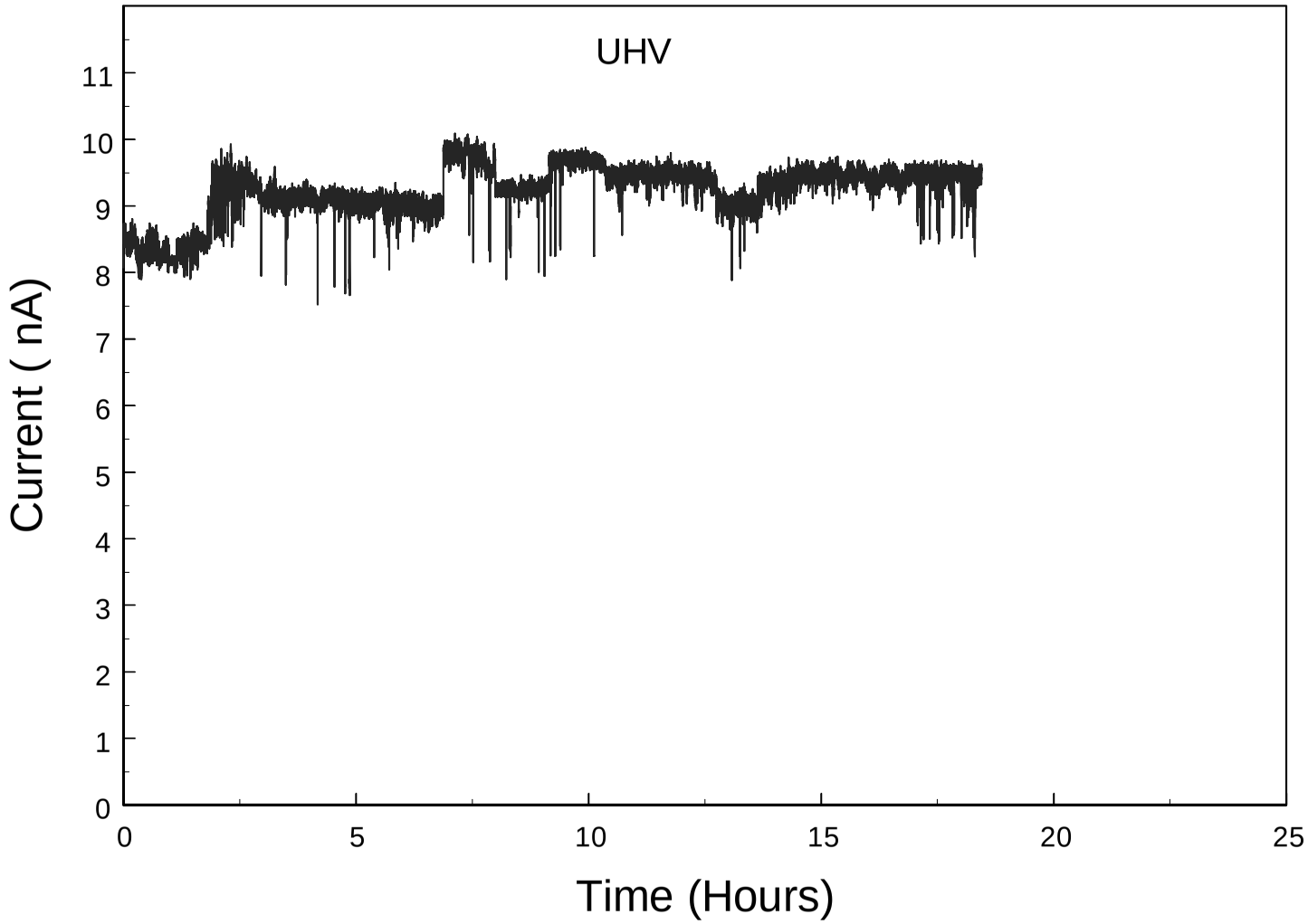

Figure 4.6 Field emission current as a function of time for a single wall nanotube sample exposed to Cs for 4 minutes and positioned at a anode-film separation of 250 μm. The current is measured while the sample is in UHV.

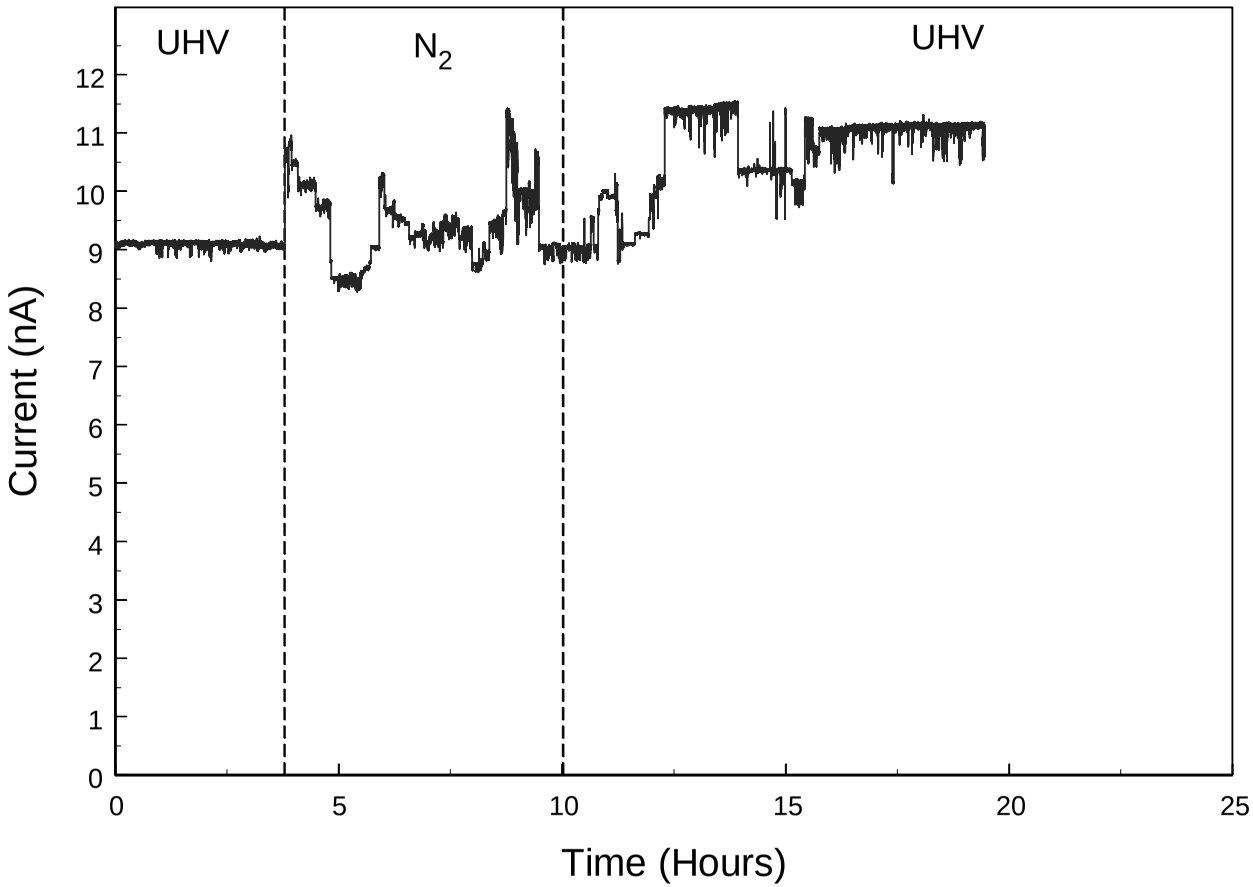

Figure 4.7. Field emission current as a function of time for a single wall nanotube sample exposed to Cs for 4 minutes and positioned at a anode-film separation of 250 μm. The current is measured while the sample is exposed to N_2 at 10^{-7} Torr for a period of 6 hours.

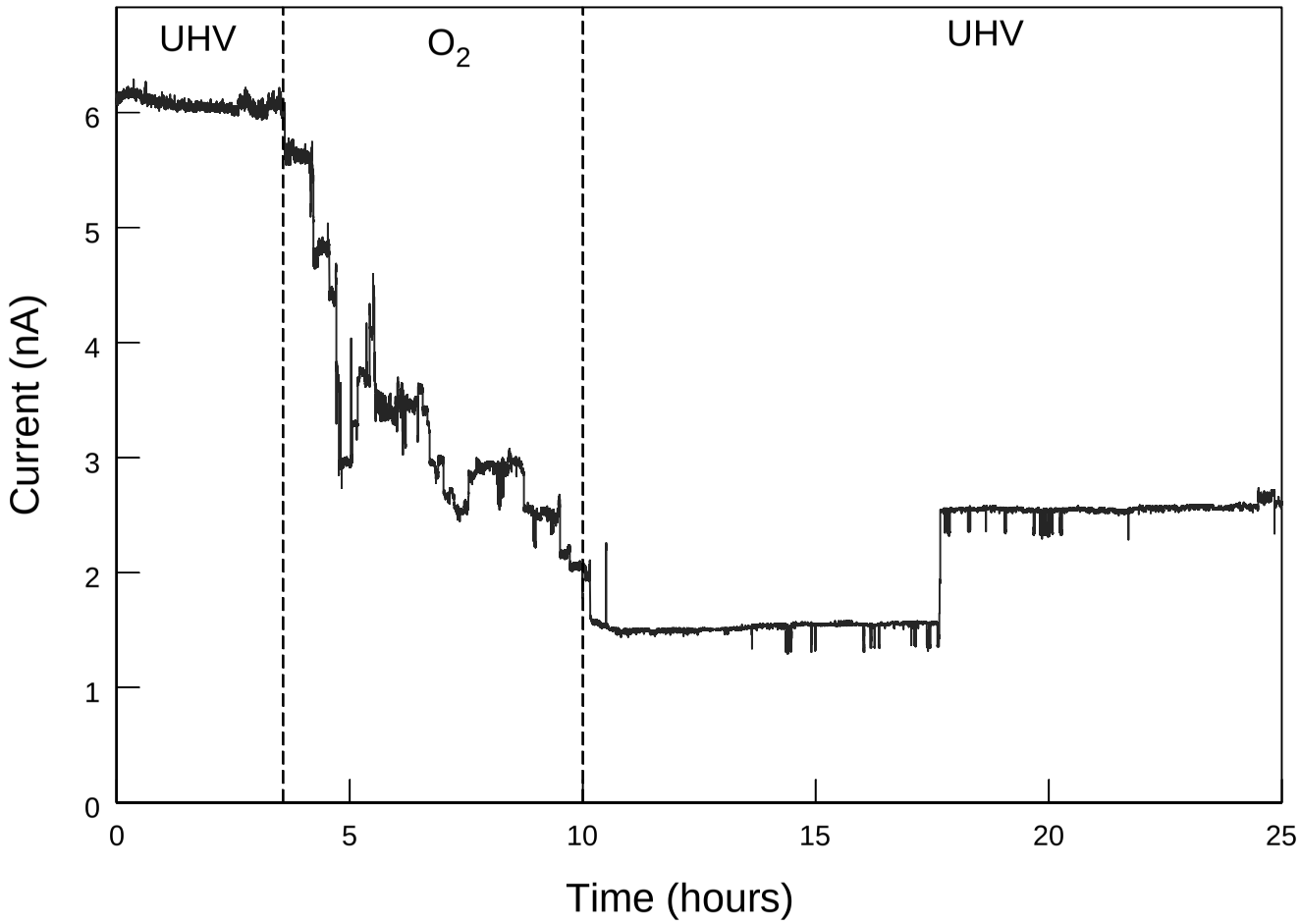

Figure 4.8. Field emission current as a function of time for a single wall nanotube sample exposed to Cs for 4 minutes and positioned at a anode-film separation of 250 μm. The current is measured while the sample is exposed to O_2 at 10^{-7} Torr for a period of 6 hours.

complete recovery. This difference is possibly due to the presence of Cs in Figure 4.8, though exactly how the Cs affects the recovery is beyond the scope of this experiment.

4.8 Conclusions

In summary, Cs deposition on SWNT bundles has a significant effect on the FE properties of the carbon nanotubes. The threshold field voltage is reduced by a factor of 2.1 - 2.9 and the FE current increased by almost 6 orders of magnitude. The FE *I-V* curves of samples exposed to Cs show a saturation effect at large currents attributed to the Cs and O_2 adsorbates. At high currents, the Cs adsorbates do not desorb. At lower currents, the ratio of slopes before and after Cs deposition is approximately 2.1, indicating perhaps, a reduction in the work function of the SWNT bundle. The reduction of the threshold voltage and the increase in FE current is due either to tunneling from Cs adsorbate states, or reduction of the work function of the SWNTs, or a combination of both effects. The magnitude of the FE current does not decrease in UHV and during exposure to N_2, but decreases during exposure to O_2. The cesiated SWNT bundles show great potential as economical and reliable vacuum electron sources.

References

1. R. Haefer, *Z. Phys.*, **116**, 604 (1940).

2. R. L. Bell, *Negative Electron Affinity Devices* (Clarendon, Oxford, 1973).

3. M. W. Geis and J. C. Twichell *Appl.Phys. Lett.* **67**, 1328 (1995).

4. R. U. Martinelli and D. G. Fischer, *Proc. IEEE* **62**, 1339 (1974).

5. J. M. Macaulay, I. Brodie, C. A. Spindt, and C. E. Holland, *Appl. Phys. Lett.* **61**, 997 (1992).

6. L. S. Pan, T. E. Felter, D. A. A. Ohlberg, W. L. Hsu, C. A. Fox, R. Cao, and G. Vergara, *J. Appl. Phys.* **82**, 2624 (1997).

7. A. Thess, R. Lee, P. Nikolaev, H. Dai, P. Petit, J. Robert, C. Xu, Y. H. Lee, S. G. Kim, A. G. Rinzler, D. T. Colbert, G. E. Scuseria, D. Tomanek, J. E. Fischer, R. E. Smalley, *Nature* **273**, 488 (1996).

8. S. Suzuki, C. Bower and O. Zhou, *Chem. Phys. Lett* **285**, 230 (1998).

9. O. Zhou, R. M. Fleming, D. W. Murphy, C. H. Chen, R. C. Haddon, A. P. Ramirez, S. H. Glarum, *Science* **263** , 1744 (1994).

10. S. Suzuki, and M. Tomita, *J. Appl. Phys.* **79** 3739 (1996).

11. R. S. Lee, H. J. Kim, J. E. Fisher, A. Thess, R. E. Smalley, *Nature* **388,** 255 (1997).

12. A. M. Rao, P. C. Eklund, S. Bandow, A. Thess, R. E. Smalley, *Nature* **388**, 257 (1997).

13. L. Grigorian, G. U. Sumanasekera, A. L. Loper, S. Fang, J. L. Allen, and P. C. Eklund, *Phys. Rev. B* **58,** R4195 (1998).

14. J. E. Fischer, R. S. Lee, H. J. Kim, A. G. Rinzler, R. E. Smalley, S. L. Yaguzhinski, A. D. Bozhko, D. E. Sklovsky, and V. A. Nalimova *Phys. Rev. B* **55,** R4921 (1997).

15. A. B. Kaiser, G. Dusberg, and S. Roth, *Phys. Rev. B* **57**, 1418 (1998).

16. J. Hone, I. Ellwood, M. Muno, A. Mizel, M. L. Cohen, A. Zettl, A. G. Rinzler, and R. E. Smalley, *Phys. Rev. Lett.* **80**, 1042 (1998).

17. S. Suzuki, C. Bower, Y. Watanabe and O. Zhou, *Appl. Phys. Lett.* **76**, 4007 (2000).

18. Tubes@Rice, P.O. Box 1892, Houston, TX 77251.

19. A. G. Rinzler, J. Liu, H. Dai, P. Nikolaev, C. B. Huffman, F. J. Rodriguez-Macias, P. J. Boul, A. H. Lu, D. Heymann, D. T. Colbert, R. S. Lee, J. E. Fischer, A. M. Rao, P. C. Eklund, and R. E. Smalley, *Appl. Phys. A* **67**, 29 (1998).

20. A. Joshi, *Metals Handbook Ninth Edition: Volume 10, Materials characterization*, (American Society for Matrials, Materials Park, OH 1986).

21. L. E Davis, N. C. MacDonald, P. W. Palmberg, G. E. Riach, and R. E. Weber, *Handbook of Auger Electron Spectroscopy* (Physical Electronics Industries, eden Prairie, 1976).

22. J. M. Bonard, J. P. Salvetat, T. Stockli, W. A. de Heer, L. Forro, and A. Chatelain, *Appl. Phys. Lett.* **73**, 918 (1998).

23. K. A. Dean, and B. R. Chalamala, *Appl. Phys. Lett.* **76**, 375 (2000).

24. C. A. Spindt, I. Brodie, L. Humphrey, and E. R. Westerberg, *J. Appl. Phys.* **47**, 5248 (1976).

25. K. A. Dean, and B. R. Chalamala, *Appl. Phys. Lett*. **75**, 3017 (1999).

26. J. Y. Cavaille and M. Dechsler, *Surf. Sci*. **75**, 342 (1978).

27. H. Adachi, K. Fujii, S. Zaima, Y. Shibata, C. Oshima, S. Otani, and Y. Ishizawa, *Appl. Phys. Lett.* **43**, 702 (1983).

CHAPTER 5

EFFECTS OF GAS EXPOSURE ON THE FIELD EMISSION PROPERTIES OF SINGLE WALL AND MULTIWALL NANOTUBES

5.1 Introduction

In sections 5.2 – 5.4, I discuss the choice of H_2, Ar and O_2 as test gases for the carbon nanotube (CNT) field emitters. Part of the motivation in choosing these particular gases comes from current research being done in the effects these gases have on the electronic and transport properties of CNTs. Sections 5.5 and 5.6 describe how multiwall nanotubes (MWNTs) were grown in the laboratory and the probable mechanism involved in their growth process. The Field emission (FE) experiment is described in detail in section 5.7 and the results are presented in section 5.8.

5.2 Selection of Hydrogen as an Ambient Test Gas

Storage of hydrogen in carbon nanotubes has garnered a lot of interest in recent years [1,2,3,4]. It is believed between 5-10 weight % (the weight of H_2 adsorbed divided by the weight of the carbon nanotubes plus the H_2 adsorbed by the nanotubes) of

hydrogen molecules can be physisorbed on the exterior surfaces of carbon nanotubes or the interstitial spaces between carbon nanotubes [4,5]. This value goes up to 20 weight % for carbon nanotubes doped with alkali metals [6]. Chemisorption sites have also been found on the exterior surfaces of single wall nanotubes (SWNTs) where H_2 molecules are likely to adsorb [7].

Although hydrogen is less than 0.00005% by volume of our general atmosphere it is an important factor in UHV studies. Because of its light mass it is notoriously difficult to pump out of vacuum chambers and is one of the most prevalent gases present at or below 1×10^{-9} Torr. In sharp metal emitters hydrogen is known to cause sputter-assisted atomic diffusion which can grow nanoscale protrusions on the emitter surface [8,9]. These protrusions can lead to increased current emission leading to runaway current which can destroy the emitter through a vacuum arc [10]. Thus in a FE vacuum system it would be crucial to understand how ambient hydrogen reacts with active CNT emitters.

5.3 Selection of Argon as an Ambient Test Gas

Argon exists in trace amounts of less than 1% by volume in the general atmosphere. It is not much of a problem gas in vacuum environments due to the relative ease of its evacuation and the general lack of its reactivity with other compounds. This lack of reactivity is in sharp contrast to oxygen, which like Ar is a high mass gas. High mass gases can dull extremely sharp tips and protrusions through sputtering [10]. Since oxygen was one of my test gases, to distinguish between current degradation due to

sputtering and current degradation due to surface chemical reactions I utilized Ar gas as well. Ar is also known to adsorb on the outer surfaces of SWNT bundles by first filling up the interstitial groove sites and then line by line covering the entire outer surface of the nanotube bundle[11].

5.4 Selection of Oxygen as an Ambient Test Gas

Oxygen molecules constitute almost 21% by volume of our planetary atmosphere. This abundance combined with the chemically reactive nature of oxygen is the reason for the prevalence of oxygen and oxygenic gases in vacuum environments. Considerable interest has been shown of late on the effects of oxygenic gases on the electronic and transport properties of carbon nanotubes . The electrical conductance of a semi-conducting SWNT is known to increase upon exposure to nitrogen dioxide [12]. Small-gap semi-conducting nanotubes exhibit metallic properties when exposed to oxygen, and oxygen in particular has been found to increase electrical conductance of the nanotubes with a corresponding increase in the local density of states [13]. The thermoelectric power is also shown to be sensitive to oxygen exposure [13].

While much of the recent work relates to the transport measurements of carbon nanotubes little has been done to ascertain the impact of gas exposure as it relates to field emission (FE). Previous studies have reported about the effects of gases on the FE of carbon nanotubes, but these experiments were limited to a single current over a period of gas exposure [10,14,15,16]. Oxygen adsorbed on metal emitters is known to reduce the

FE current by inducing surface dipoles [8,17]. As far as nanotube FE is concerned recent experimental studies have shown that exposure to H_2O induces a large current increase which remains stable over long periods in UHV conditions [18,19]. However long term exposure to oxygen results in almost instantaneous and largely irreversible current degradation [10]. Also lacking is a comparative analysis among the various types of carbon nanotubes , such as SWNTs and MWNTs, as field emitters. My study addresses this issue directly.

5.5 Production of Multiwall Carbon Nanotubes

150 nm of iron film was deposited onto a silicon wafer using a vacuum evaporator. The silicon substrate was placed on a quarz boat and put into the center of a glass tube 5.65 cm in diameter and 91 cm long which is heated by a high temperature cylindrical tube furnace made by Fisher Scientific . The silicon wafer was placed coated side up since the iron particles act as catalysts for CNT growth [20]. The tube was then evacuated to a pressure of 1×10^{-6} Torr using a liquid nitrogen trapped mechanical pump. Then nitrogen gas was introduced into the tube at a flow rate of 250 standard cubic centimeter (sccm) along with hydrogen at 11 sccm and at a pressure of 300 Torr. Then the sample was heated to a temperature of 735°C over approximately 10 minutes. On reaching 735°C, the hydrogen flow was turned off and replaced with 20 sccm of acetylene for approximately 10 minutes. The acetylene is to provide carbon for the growth of Carbon nanotubes. After this time, the acetylene was turned off and the system

pressure readjusted to 1.3 Torr and the nitrogen flow rate set at 300 sccm. The furnace was turned off and allowed to cool to room temperature over an approximately two hour period.

We experimented with various parameters such as the flow rate of gases, temperature and the growth period allowed to obtain various multiwall nanotube samples. The sample whose growth is described above and was utilized for FE analysis was chosen because it had the lowest resistance measured at approximately 400 Ω.

5.6 Growth Mechanism of Multiwall Nanotubes

It has been known for over a hundred years that carbon filaments can be created by the catalytic decomposition of a carbon containing gas on a hot surface [20]. Despite the vast expanse of time it is still not clearly understood till today exactly how carbon atoms configure to synthesize the various types of nanotubes. The growth procedure outlined in section 5.5 which I used to grow multiwall nanotubes depended on iron particles to catalyze the decomposition of acetylene at 700°C. Several growth models have been developed to describe the formation of carbon nanotubes by the catalytic breakdown of organic gases [21,22,23]. It is generally believed that the first stage in the nanotube growth is the decomposition of the hydrocarbon – acetylene in my case – on the exposed front surface of the metal particle.

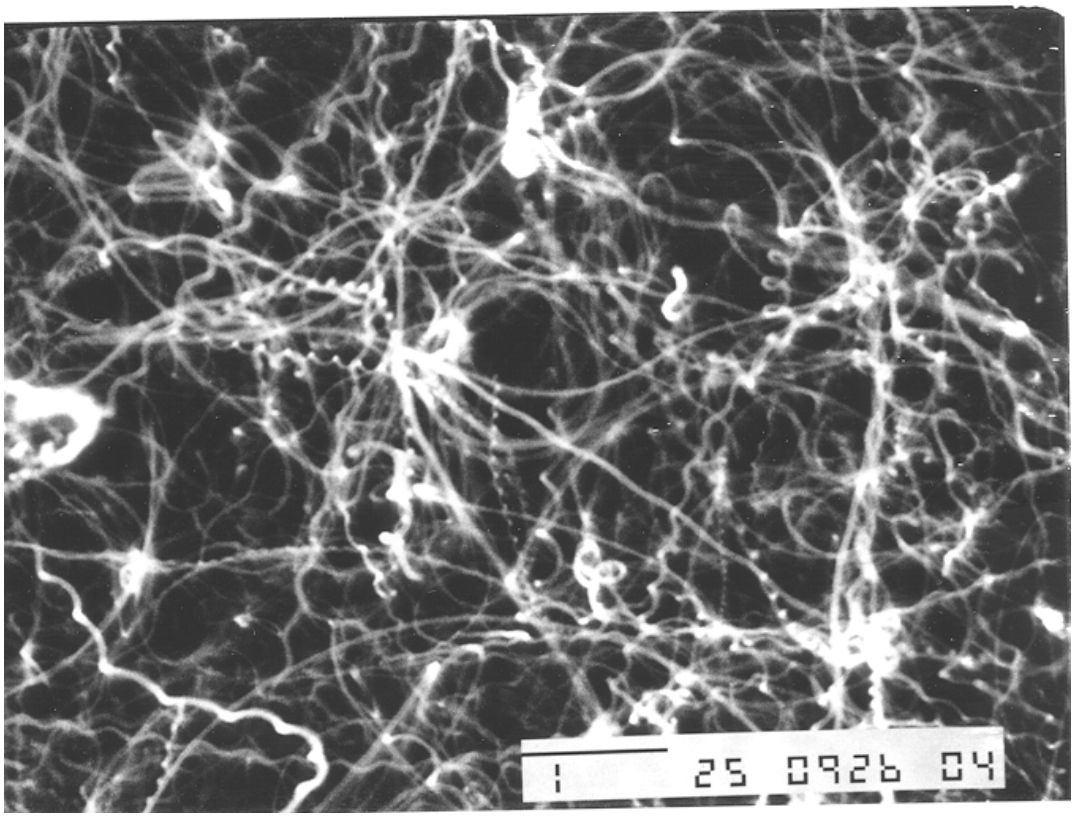

Figure 5.1 SEM picture of the multiwall nanotubes grown in the laboratory. The bar in the picture represents one micron.

This decomposition produces hydrogen and carbon which oversaturate the front surface causing the carbon to dissolve into the metal. The dissolved carbon then diffuses through the particle and is extruded on the other side. It is believed that the metallic catalyst particles promote tip growth or base growth depending on the contact force between the catalyst particles and the substrate [23]. The carbon atoms can also deposit on top of the growing tube promoting growth above the iron nanoparticle as shown in Figure 5.2.

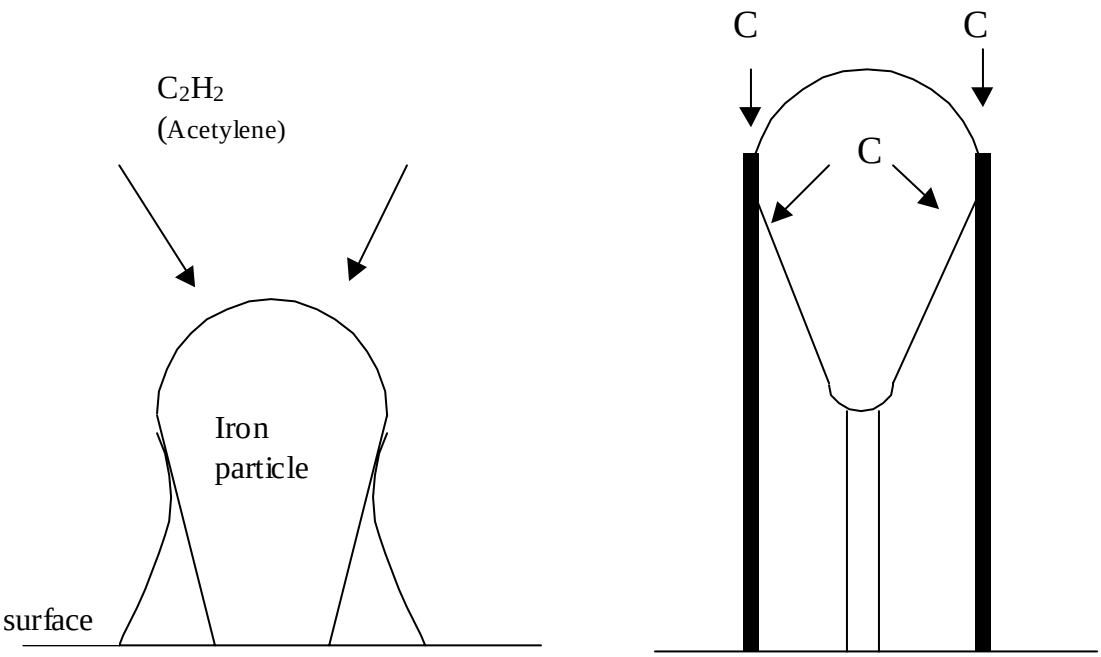

Figure 5.2 Growth model for the formation of multiwall nanotubes

5.7 Experiment

The SWNT bundles were purchased from Tubes@Rice [24] as a slurry in toluene and their characteristics and properties have been detailed in chapter 2. The slurry of SWNT bundles in toluene was deposited onto a conducting Si substrate and allowed to dry resulting in a mat of approximately 6 microns as measured by an optical telescope. The Si wafer was then secured onto a quarz holder using tantalum clips as shown in Figure 3.3 of chapter 3. The MWNTs grown on a Si substrate as described in section 4.5 were similarly mounted on a quarz holder and secured with tantalum clips.The samples were then placed in the UHV compatible preparation chamber for out-gassing as described in chapter 2. These samples were processed on different days but their transfer from the preparation chamber to UHV-STM chamber was similar. They were heated to

500 °C with the temperature measured by a digital pyrometer. The fluctuating pressure due to the out-gassing was monitored with an ionization gauge and after almost 24 hours the samples were ready for transfer. They were then linearly translated through an all metal valve into the UHV-STM chamber which, as described in detail in chapter 2, has leak valves and a gas analyzer. The carbon nanotubes are placed in the sample stage and the Burleigh UHV STM is utilized for the positioning process as described in chapter 2. Before introducing the gases , FE *I-V* curves of the sample are measured in UHV. The first gas I introduced into the chamber was hydrogen. To achieve approximately 65 L (1 L = 10^{-6} Torr s) of exposure, hydrogen was leaked into the vacuum system to a pressure of 3×10^{-7} Torr and the nanotubes were biased at voltages that produce a FE current of 4μA for 216 s. After this exposure, the vacuum system was evacuated to < 10^{-10} Torr and FE *I-V* curves are measured. In this manner, the nanotubes were not exposed to hydrogen during the *I-V* curve measurement. The samples were exposed at high voltages rather than zero volts to simulate working conditions encountered in practical applications. To achieve approximately 650 L of exposure, hydrogen was introduced again into the vacuum chamber to a pressure of 3×10^{-7} Torr and the nanotubes were biased at 4μA for 2160 s. Then the system was evacuated and the FE *I-V* curves were measured once again by a separate high voltage system as detailed in chapter 3. This procedure was repeated for 6500 L exposure with 4 μA maintained for a total of six hours. Once FE *I-V* curves had been taken the CNT sample was raised slightly to appropriate a new surface. On this surface I conducted current versus time experiments by biasing the sample to produce 4 μA while exposing it to 3×10^{-7} Torr of hydrogen for six hours. Then FE *I-V* and current

versus time experiments were done with argon gas. Finally the carbon nanotubes were exposed to oxygen and FE *I-V* data taken.

5.8 Results and Discussion

In Figures 5.3 – 5.7 the FE data are plotted $\ln(I/V^2)$ versus $(1/V)$ to allow comparison with the straight-line behavior predicted for FE by the FN equation. The inset in the figures are the *I-V* curves plotted using a log-linear scale. The small current on the order of 10^{-13} A observed below the threshold voltage for FE is due to leakage across the connectors. Before introducing O_2 , FE *I-V* curves were measured in UHV as shown by the clear-circle plots in Figures 5.3 and 5.4 .To achieve approximately 65 L of exposure, O_2 is leaked into the vacuum system to a pressure of 3×10^{-7} Torr and the nanotubes were biased at voltages that produce a FE current of 4μA for 216 s. These voltages were approximately 437V and 750V for SWNTs and MWNTs, respectively. After this exposure, the vacuum system was evacuated to $< 10^{-10}$ Torr and FE *I-V* curves were measured, as shown by the second plots in Figures 5.3 and 5.4. During the 650 L of exposure, the voltages required to bias the nanotubes at 4μA for 2160 s were 440V and 754V for SWNTs and MWNTs, respectively. Then the system is evacuated and the FE *I-V* curves were measured, as shown by the plot symbolized by clear boxes in Figures 5.3 and 5.4. The voltages required for 6500 L exposure were 459V and 844V for SWNTs and MWNTs, respectively and the FE *I-V* measured are represented by the filled boxes. The FE *I-V* curves represented by the solid circles (and labeled post-recovery) were taken last after allowing the nanotubes to operate at high currents in UHV for approximately 40 hours.

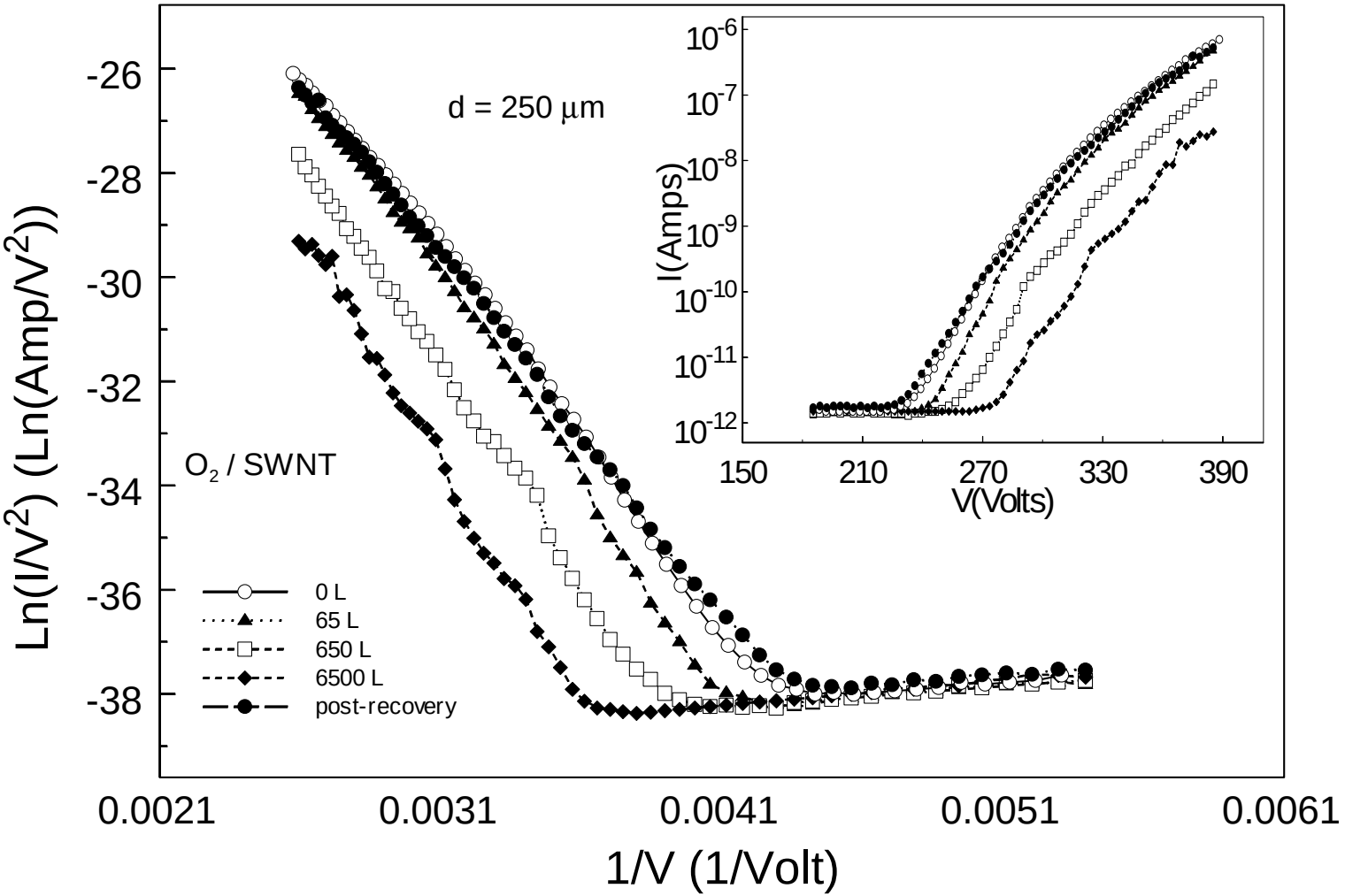

Figure 5.3. Field emission plots for 0 L , 65 L, 650 L and 6500 L O_2 exposure of single wall carbon nanotubes. The solid-circle curves labeled post-recovery were taken last after allowing the nanotubes to operate in UHV for several hours. The inset shows a plot of the field emission current versus voltage using a log-linear scale.

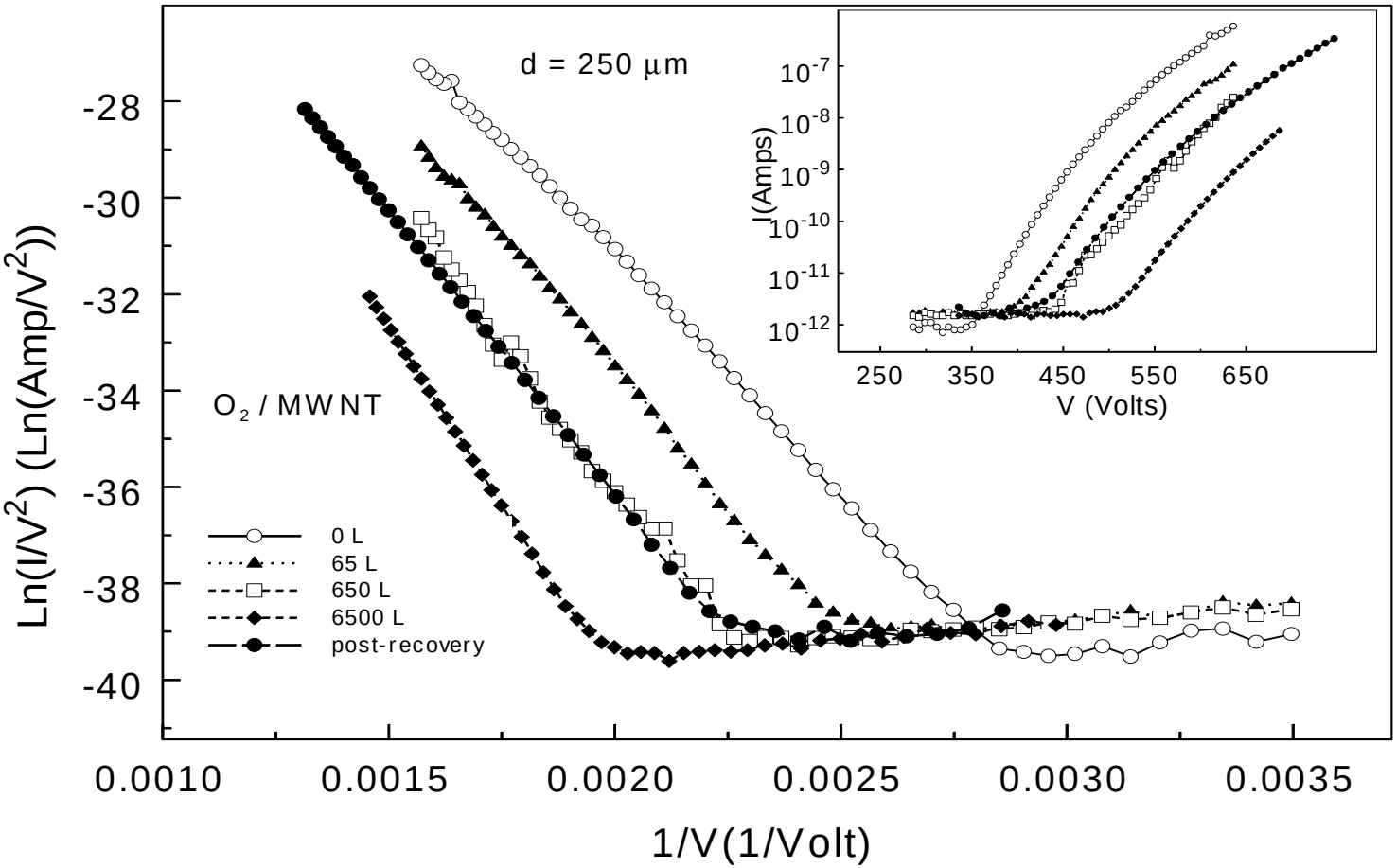

Figure 5.4. Field emission plots for 0 L, 65 L, 650 L and 6500 L O_2 exposure of multiwall carbon nanotubes. The solid circle curves labeled post-recovery were taken last after allowing the nanotubes to operate in UHV for several hours. The inset shows a plot of the field emission current versus voltage using a log-linear scale.

As shown in Figure 5.3, introduction of O_2 results in a decrease in the FE current of SWNTs, an effect that is evident after 65 L of exposure. After 6500 L of exposure, the threshold voltage for FE has increased approximately 22% from 230 V to 280 V . Before introducing O_2 the FE current is approximately 5×10^{-9} A at 300 V. After 6500 L of exposure, the FE current at 300 V decreases 2 orders of magnitude to about 5×10^{-11}A. Table 5.1 is a complete listing of the turn-on voltages for the MWNTs after each O_2 exposure. FE currents at 530 volts after each exposure are also listed. Figure 5.4 shows the FE *I-V* curves of MWNTs exposed to O_2 . Exposure to 6500 L of O_2 decreases the FE current at 600 V from approximately 2×10^{-6} A to 2×10^{-9} A, a decrease of 3 orders of magnitude. The turn on voltage increases roughly 43% from 350 V to 500 V. Table 5.2 is a complete listing of the turn-on voltages for SWNTs after each O_2 exposure. FE currents at 310 volts after each exposure are also listed. After allowing the emitters to run in UHV for approximately 40 hours, the SWNTs recover from the O_2 exposure as seen by the post-recovery plot in Figure 5.3. This almost complete recovery is an indication that the initial decrease in the FE current results from a surface chemical interaction such as formation of C-O dipoles, [10] and not permanent structural damage. The dipoles likely break up and the oxygen is desorbed during the SWNTs' operation in UHV, similar to what occurs in other types of emitters such as Mo microtip arrays during field desorption cleaning [17, 25]. The MWNTs on the other hand recover only up to about the second exposure as seen by the post-recovery curve in Figure 5.4. Even after long hours (> 40 h) of UHV operation at high currents (up to 10 μA) the MWNTs showed no further improvement.

O_2 Exposure	Threshold Voltage	FE current at 530 V
0 L	350 V	2.5×10^{-8} A
65 L	380 V	2.6×10^{-9} A
650 L	440 V	2.0×10^{-10} A
6500 L	500 V	4.0×10^{-12} A
Post-recovery	410 V	4.0×10^{-9} A

Table 5.1 FE data taken for multiwall nanotubes exposed to O_2.

O_2 Exposure	Threshold Voltage	FE current at 310 V
0 L	230 V	8.5×10^{-9} A
65 L	242 V	3.8×10^{-9} A
650 L	257 V	5.0×10^{-10} A
6500 L	280 V	5.0×10^{-11} A
Post-recovery	230 V	8.0×10^{-9} A

Table 5.2 FE data taken for single wall nanotubes exposed to O_2.

In the above experiment both SWNTs and MWNTs emit roughly the same current (4 μA) during exposure, with the latter requiring more voltage to do so. See Table 5.3 for a complete listing of voltages required to maintain 4 μA current at the start of each O_2

exposure. We find that the permanent decrease in the FE current of MWNTs is bias voltage dependent. For example, exposing the MWNTs to 6500 L of O_2 at voltages less than 745V leads to the full recovery of the MWNTs. Thus for MWNTs the higher electric fields may drive the oxygen ions to enhanced surface chemical reactions, such as etching. Etching specially at the surface caps degrades the local geometry and can lead to a permanent decrease in the FE current.[9] Molybednum arrays are known to suffer greater current degradation with increasing voltage in an oxygen environment [17]. Reference 17 attributes this to the increased electric field and the accompanying increase in electron emission with rising voltage. SWNTs operating at FE currents up to 10 μA and voltages up to 500V in O_2 were observed to recover completely.

O_2 Exposure	SWNTs	MWNTs
65 L	437 V	750 V
650 L	440 V	754 V
6500 L	459 V	844 V

Table 5.3 Voltages required to maintain 4 μA current for the single wall and multiwall nanotubes at the start of each O_2 exposure.

The F-N equation (2.22) shows that the value of $b\phi^{3/2}/\beta$ can be determined from the slope of the $\ln(I/V^2)$ vs $1/V$ curve. From this we determined the field enhancement

factor ratio β_p/β_0 , where β_p and β_0 are the enhancement factors for the post-recovery and 0 L curves respectively. Our assumption was that after their long run in UHV most of the O_2 had desorbed off the CNT's allowing them to recover their original workfunctions. Thus by taking the ratio of the slopes of the 0 L and post-recovery curves and assuming ϕ is approximately the same, we measured β_p/β_0 = 1.04 and 0.82 for SWNTs and MWNTs, respectively. This analysis is consistent with the results in Figure 5.3 showing that the SWNTs had not suffered any structural degradation that might permanently reduce the FE current. Consistent too are the findings regarding MWNTs. The reduction in the enhancement factor is indicative of permanent structural change that occurred , possibly from processes like etching .

Figures 5.5 and 5.6 show the FE *I-V* curves of SWNTs and MWNTs, respectively, after exposure to Ar. The 0 L, 65 L, 650 L and 6500 L curves all roughly coincide indicating that Ar exposure has almost no influence on the threshold voltage or FE current of the CNTs. Reference 10 reports that sputtering by Ar ions does not greatly impact upon the FE stability of SWNTs at a single current. We find this extends to the entire FE characteristics of SWNTs and MWNTs. As shown in Figure 5.7 the 0 L, 65 L, 650 L and 6500 L FE *I-V* curves taken after SWNTs' exposure to H_2 are all approximately coincident on one another. Figure 5.8 is a similar display for the results of H_2 exposure to MWNTs. In neither case does the impact of light hydrogen ions seem to influence the FE characteristics of the respective emitters. H_2 molecules are known to physisorb on the outer surfaces of CNTs as well as in between the interstitial spaces

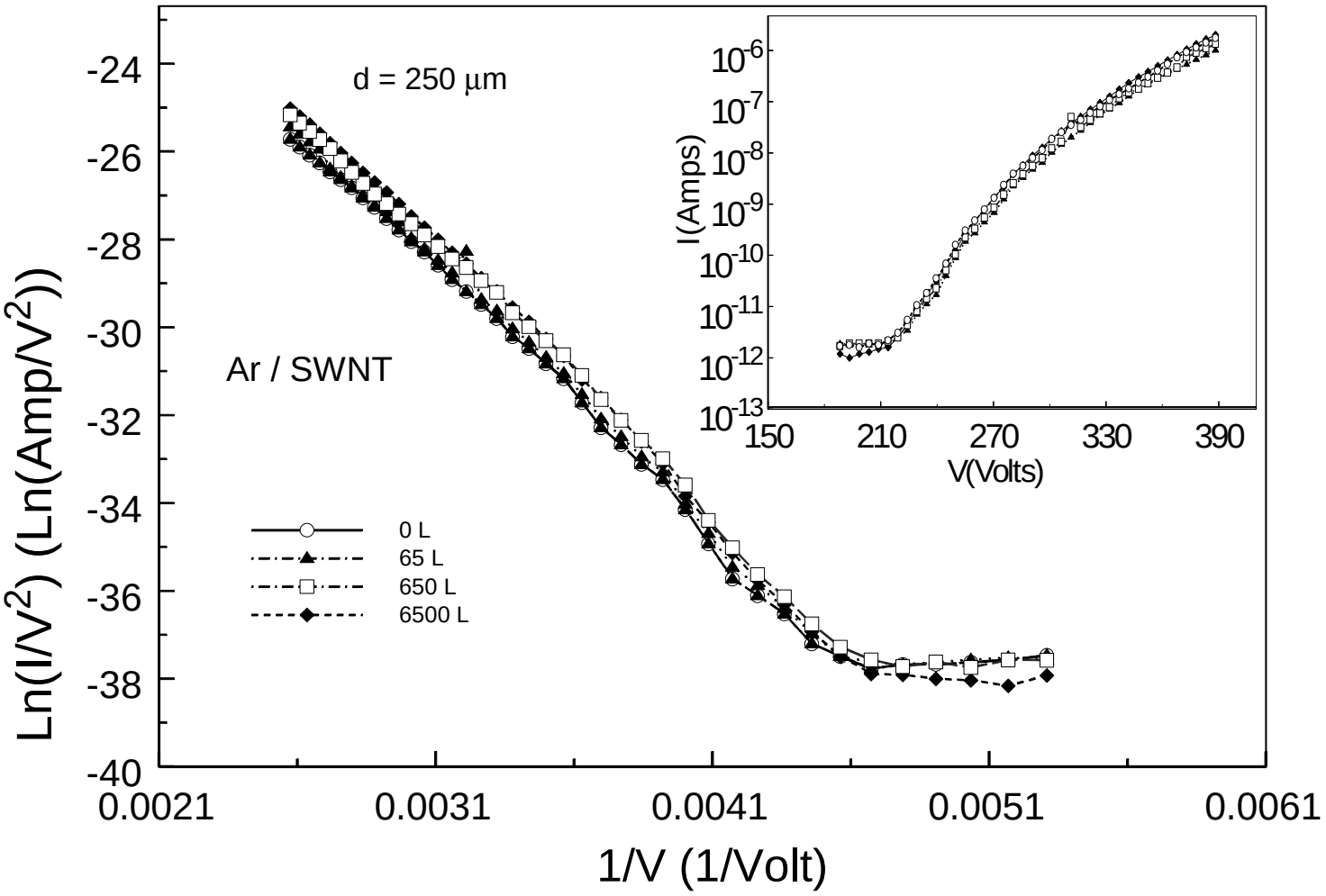

Figure 5.5. Field emission plots for 0 L , 65 L, 650 L and 6500 L Ar exposure of single wall carbon nanotubes. The inset shows a plot of the field emission current versus voltage using a log-linear scale.

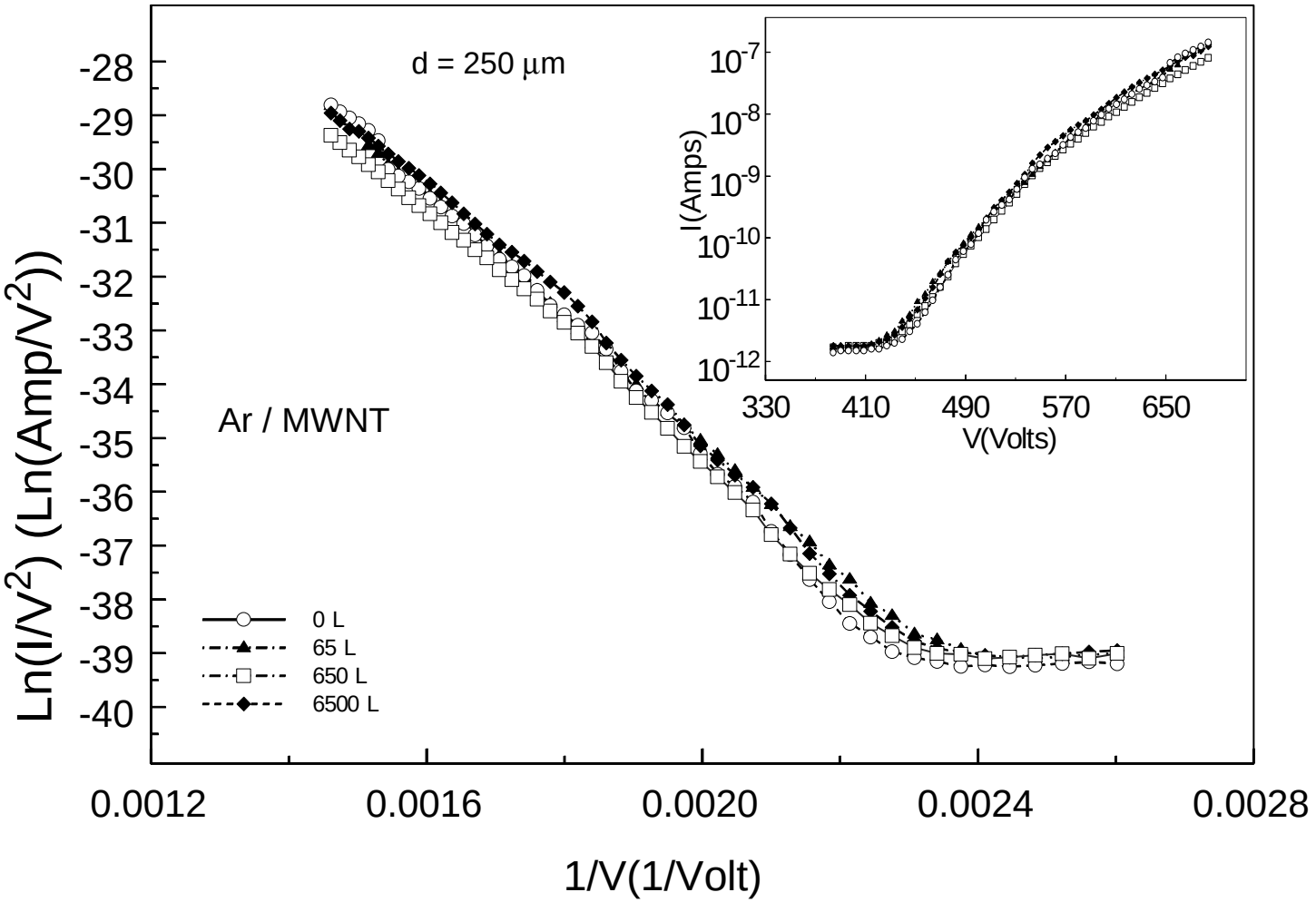

Figure 5.6. Field emission plots for 0 L , 65 L, 650 L and 6500 L Ar exposure of multiwall carbon nanotubes. The inset shows a plot of the field emission current versus voltage using a log-linear scale.

The F- N curves of Figures 5.1 – 5.4 are based on the I – V data taken for a large " sweep" of voltages and their corresponding currents. In practical situations field emitters operate at a single voltage and current value for long periods of time. Thus to model this behavior the SWNTs and MWNTs were set at initial currents of 4 μA. Then the effects of exposure of the gases H_2, Ar, and O_2 to this initial current configuration were noted. The gases were introduced to a pressure of 3×10^{-7} Torr for a period of six hours for a total exposure of approximately 6500 L. With this setup we could compare these results with our previous F-N data.

As seen in Figure 5.9 exposure of O_2 to the SWNTs causes an immediate decrease in the FE current. The current goes down by 2 orders of magnitude to a minimum value fluctuating around approximately 50 nA. Upon removal of the O_2 gas the current slowly recovers to approximately its initial value. It takes about 10 hours for the current to recover. These results are consistent with the F-N data of SWNTs exposed to O_2 presented earlier in Figure 5.3. Figure 5.10 shows the O_2 exposure to MWNTs. The current decreases by approximately 3 orders of magnitude to a minimum fluctuating around 4 nA. After the O_2 has been removed, the current recovers somewhat fluctuating around a value of 0.6 μA, but does not completely recover. This behavior is again consistent with the F-N data of MWNTs exposed to O_2 presented earlier in Figure 5.4. Figures 5.11 and 5.12 show the behavior of SWNTs and MWNTs, respectively exposed to Ar gas. The exposure does not have any effect on the magnitude of the FE current emitted by the SWNTs or the MWNTs.

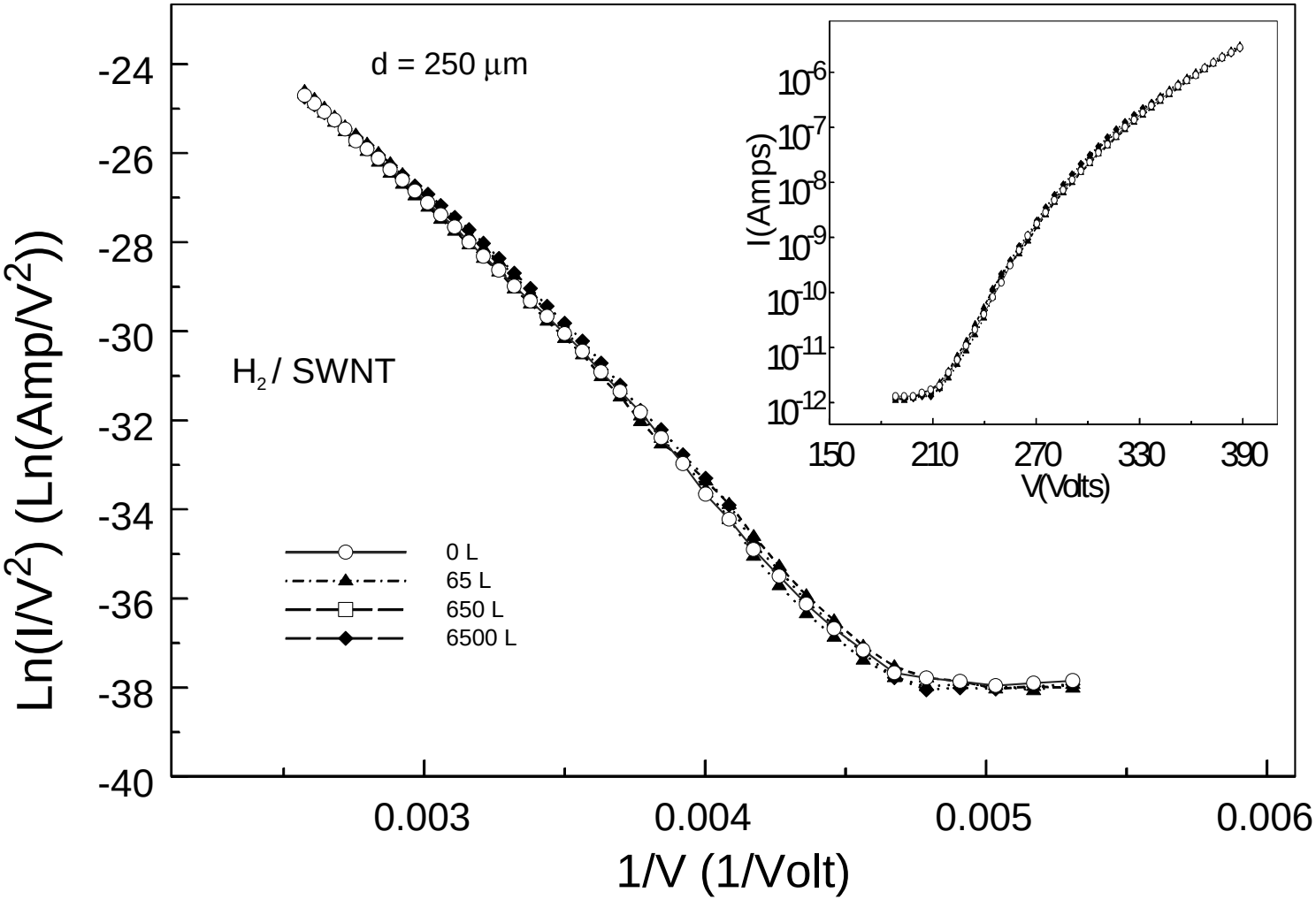

Figure 5.7. Field emission plots for 0 L , 65 L, 650 L and 6500 L H_2 exposure of single wall carbon nanotubes .The inset shows a plot of the field emission current versus voltage using a log-linear scale.

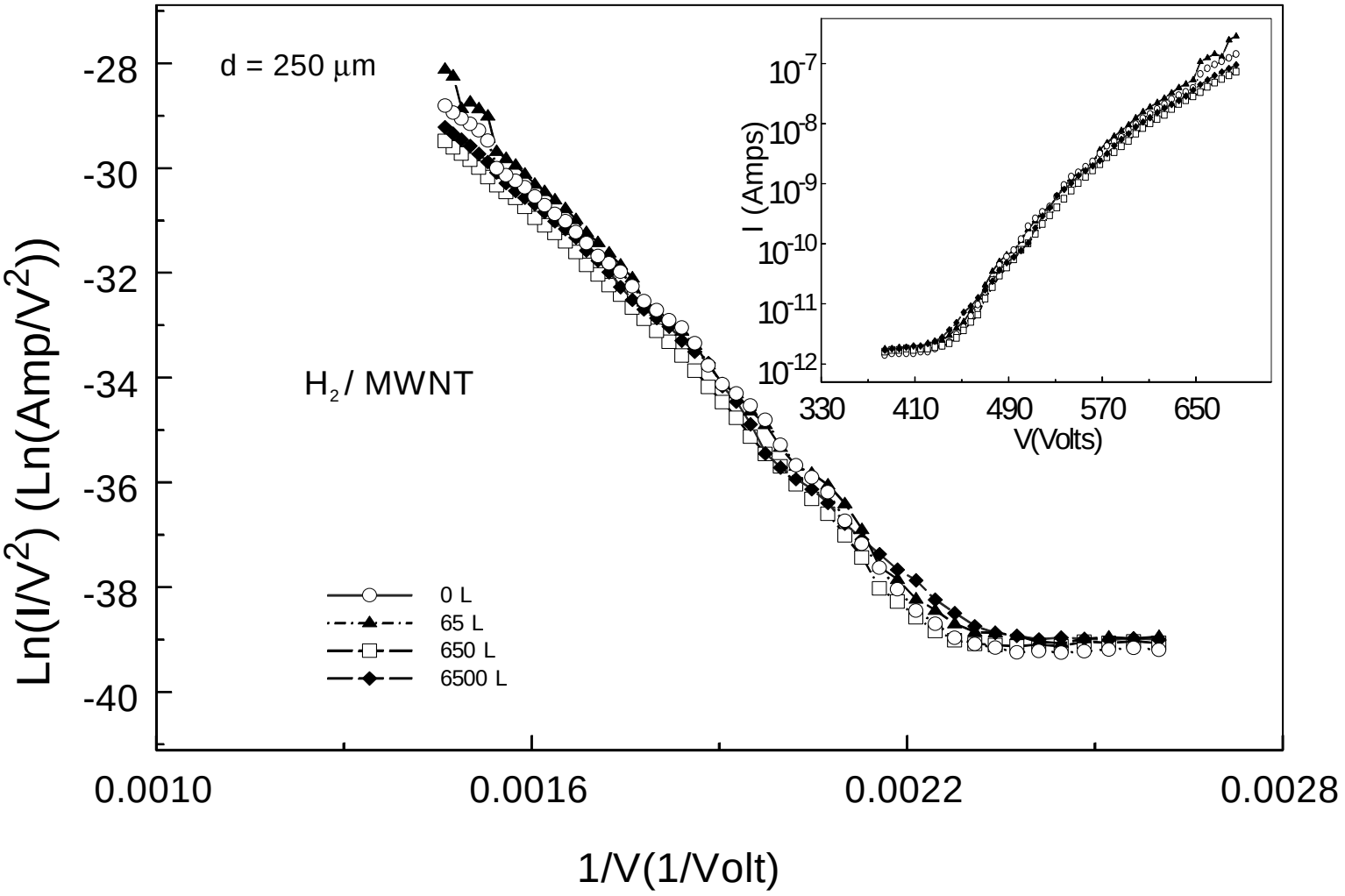

Figure 5.8 Field emission plots for 0 L , 65 L, 650 L and 6500 L H_2 exposure of multiwall carbon nanotubes. The inset shows a plot of the field emission current versus voltage using a log-linear scale.

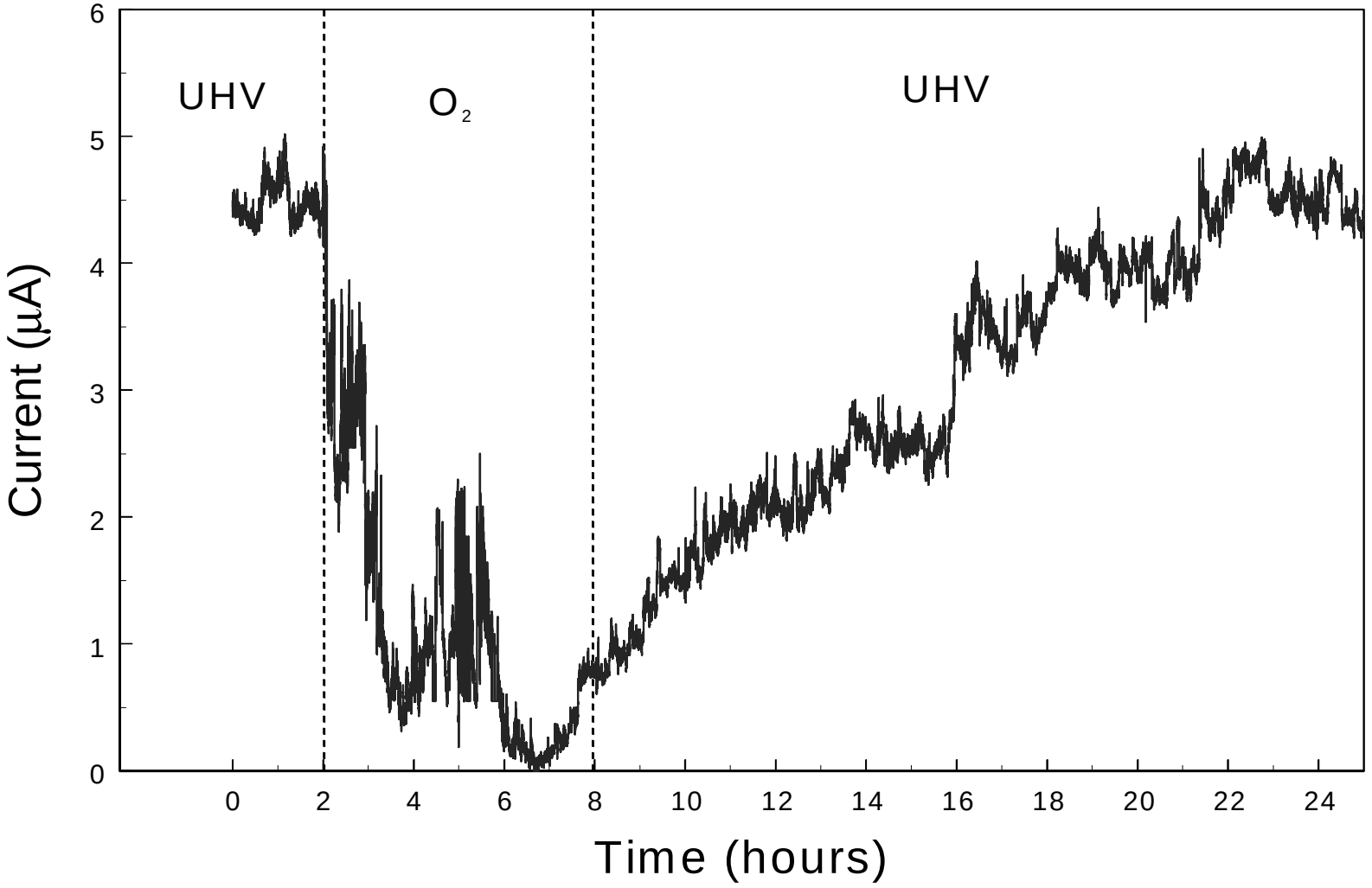

Figure 5.9 Field emission current as a function of time for a single wall nanotube sample at film-anode separation of 250 μm. The current is measured while the sample is exposed to O_2 at 3×10^{-7} Torr for a period of 6 hours.

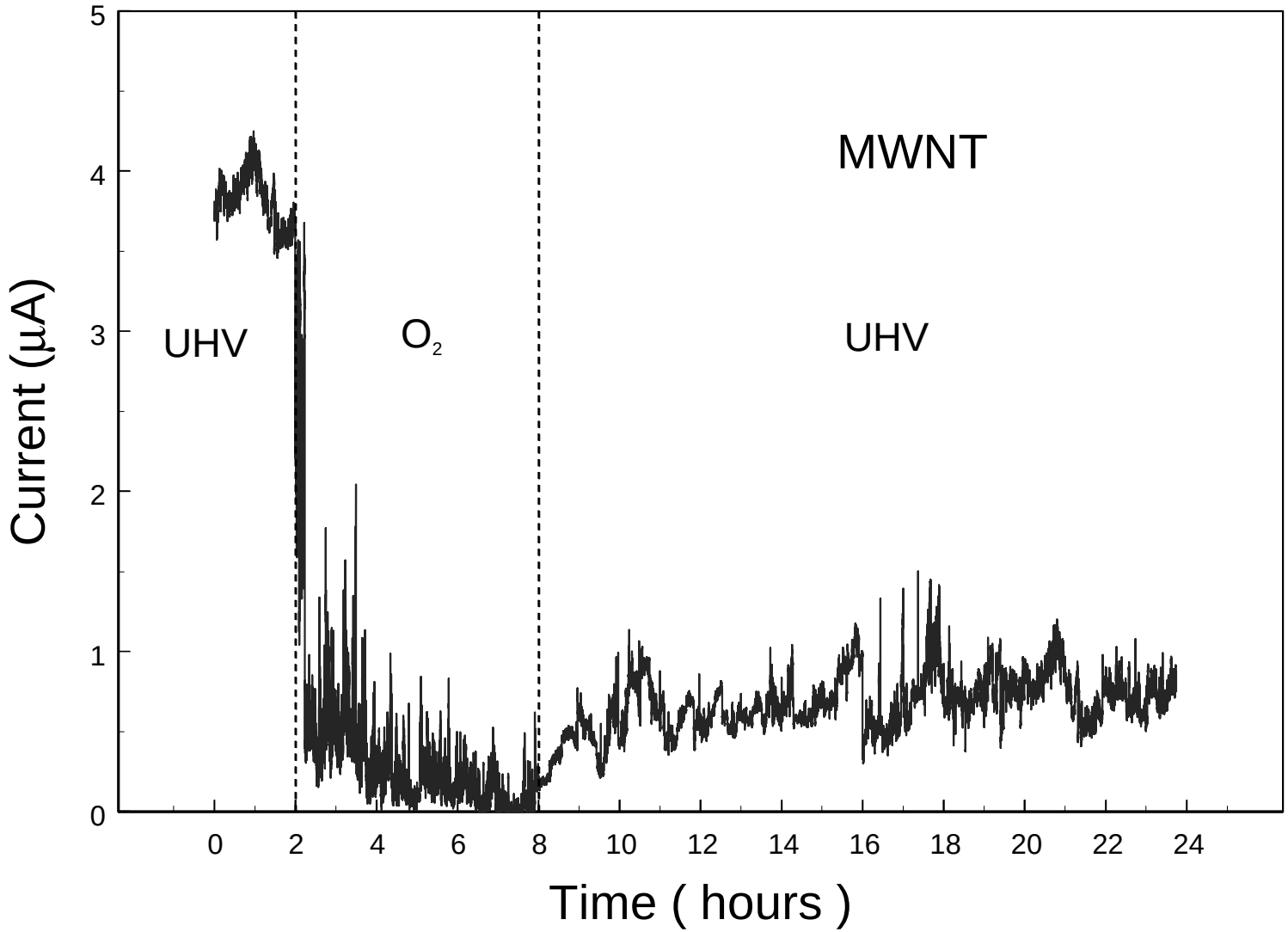

Figure 5.10 Field emission current as a function of time for a multiwall nanotube sample at film-anode separation of 250 μm. The current is measured while the sample is exposed to O_2 at 3×10^{-7} Torr for a period of 6 hours.

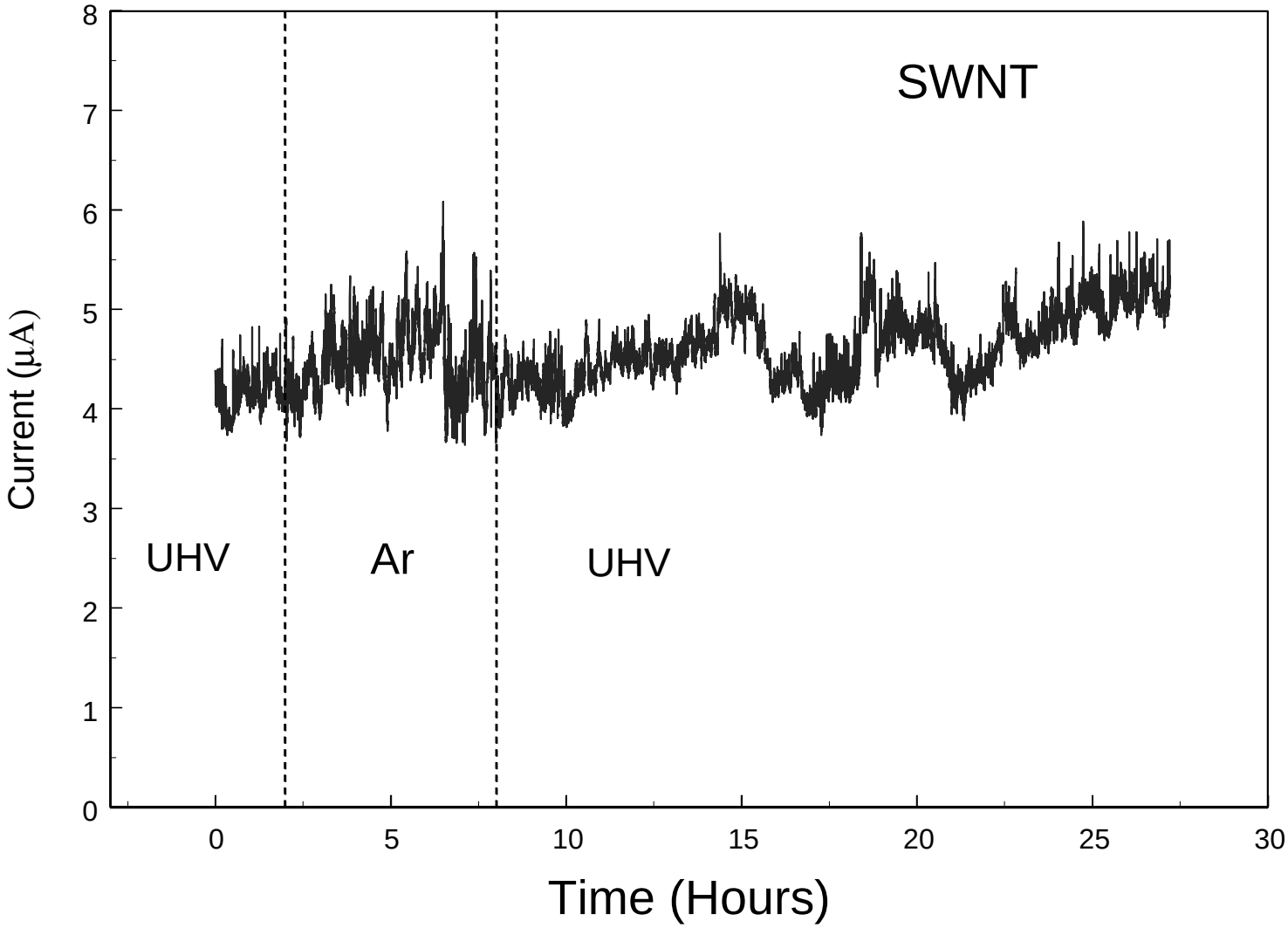

Figure 5.11 Field emission current as a function of time for a single wall nanotube sample at film-anode separation of 250 μm. The current is measured while the sample is exposed to argon at 3×10^{-7} Torr for a period of 6 hours.

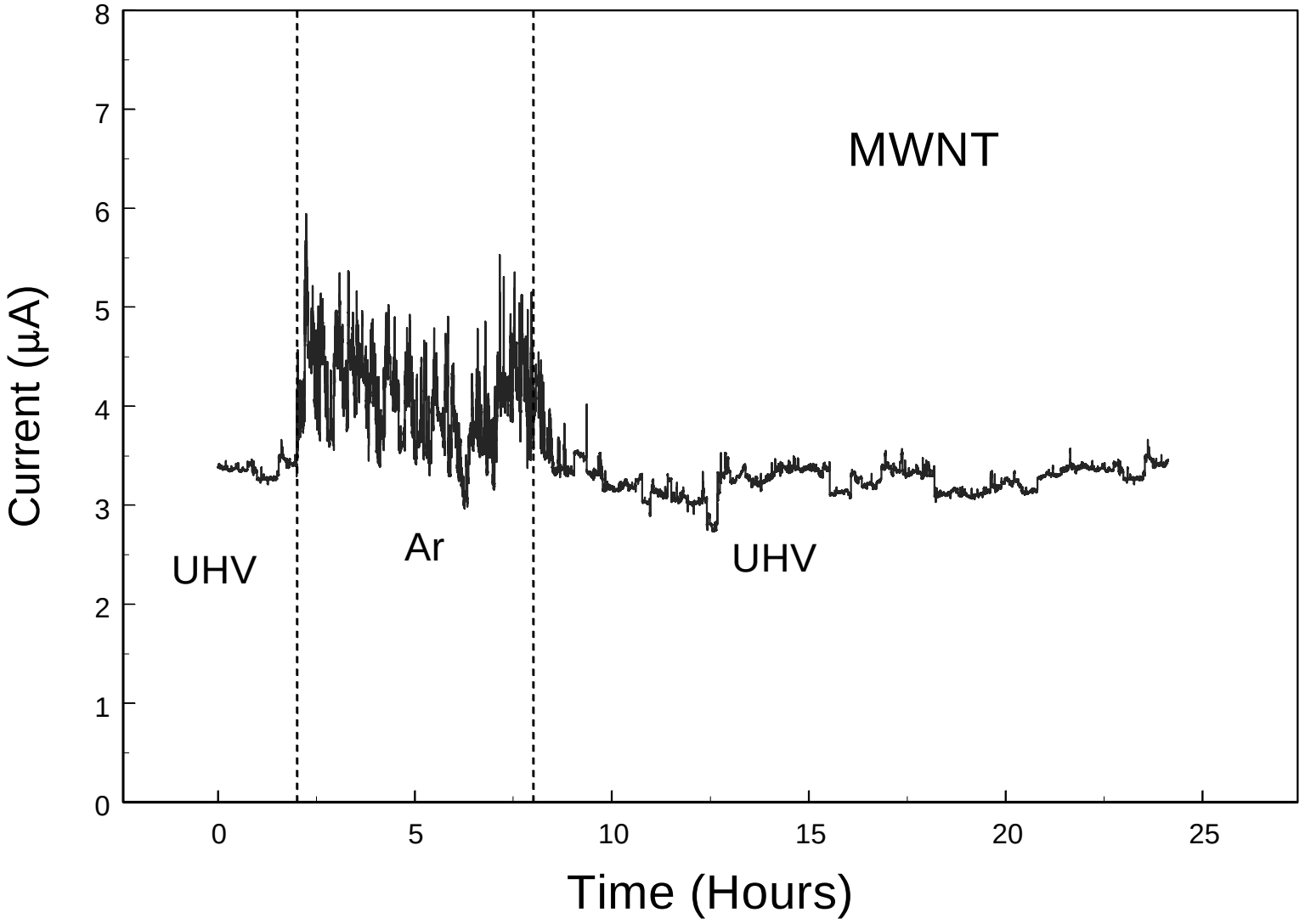

Figure 5.12 Field emission current as a function of time for a multiwall nanotube sample at film-anode separation of 250 μm. The current is measured while the sample is exposed to argon at 3×10^{-7} Torr for a period of 6 hours.

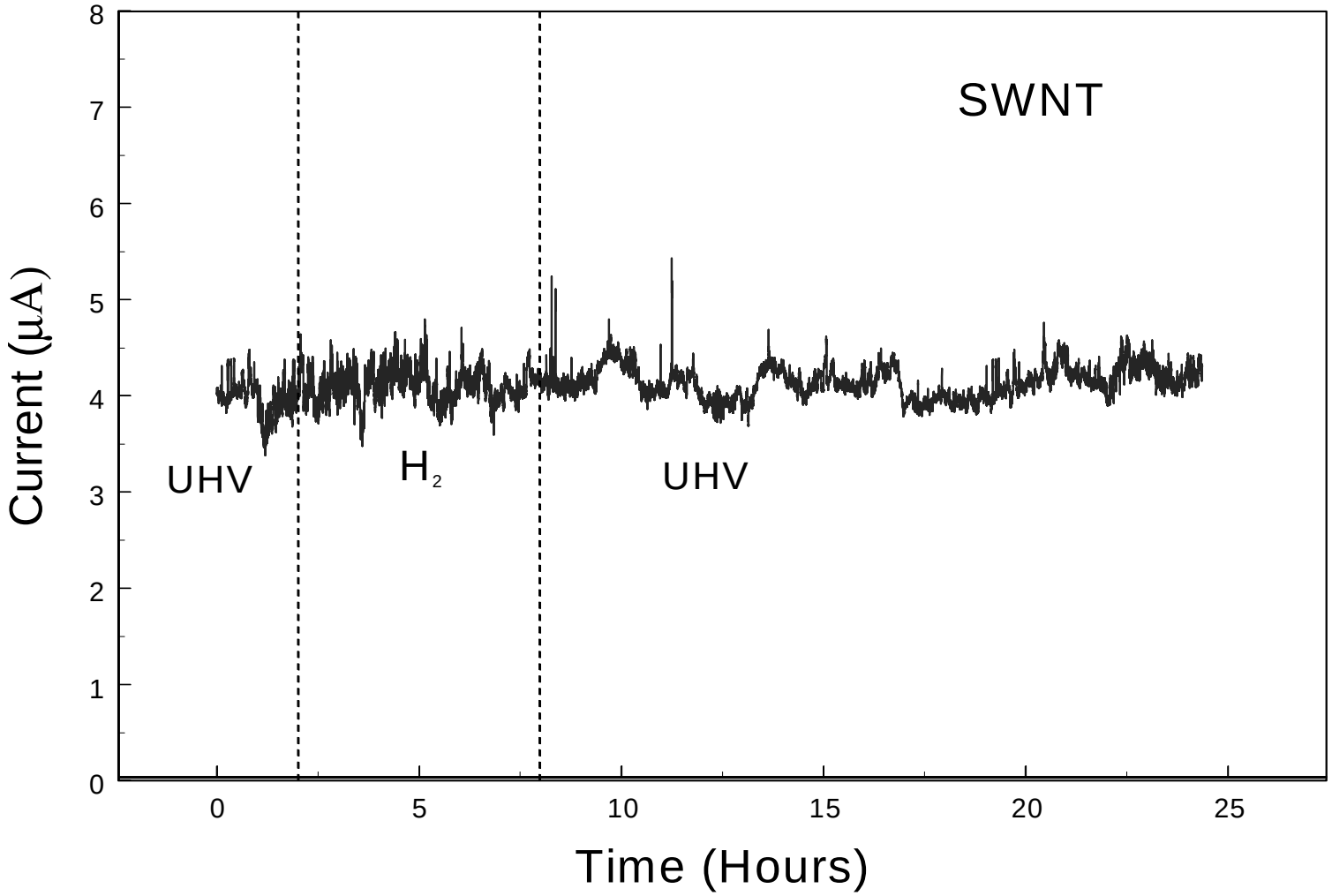

Figure 5.13 Field emission current as a function of time for a single wall nanotube sample at film-anode separation of 250 μm. The current is measured while the sample is exposed to hydrogen at 3×10^{-7} Torr for a period of 6 hours.

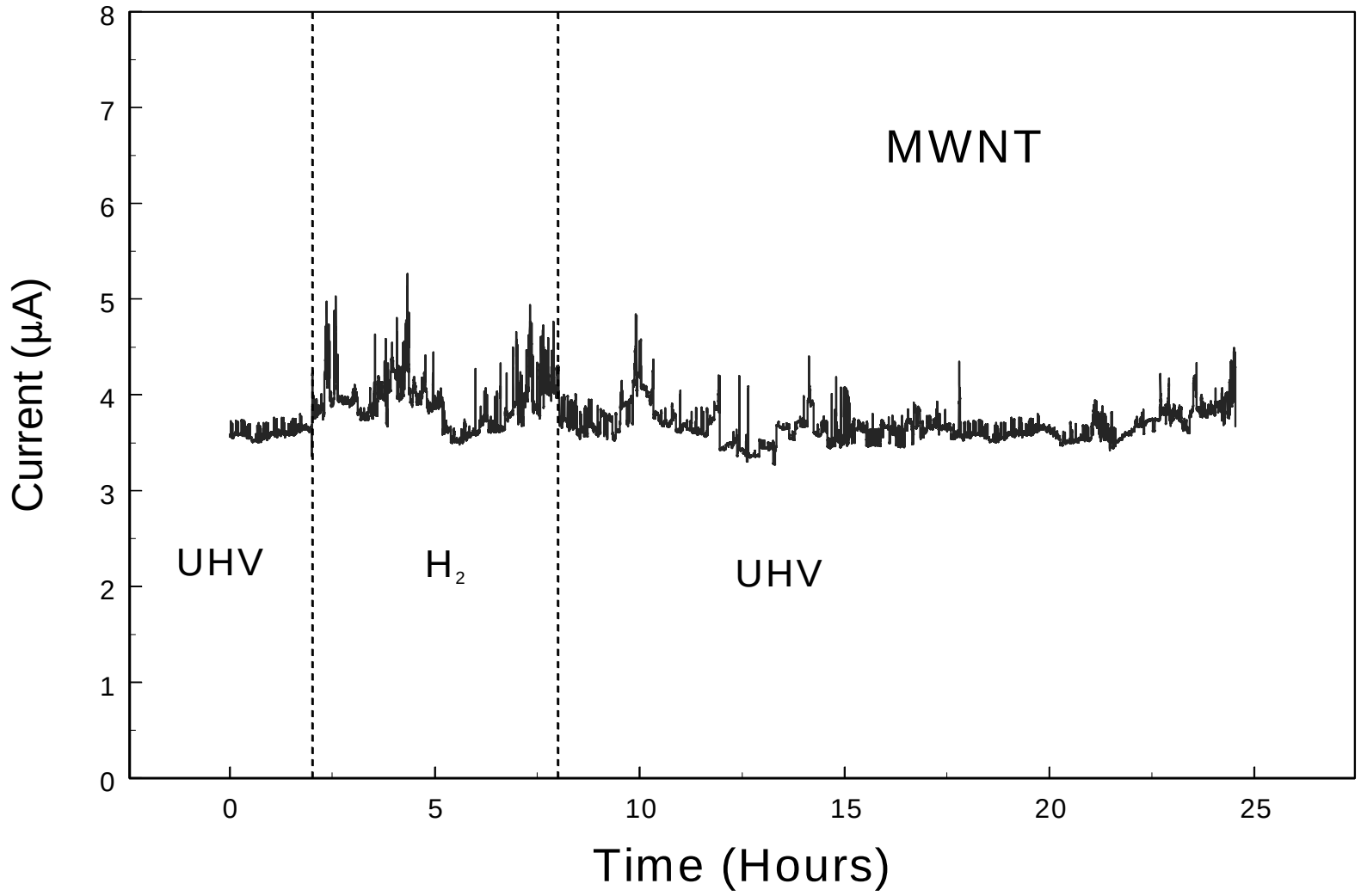

Figure 5.14 Field emission current as a function of time for a multiwall nanotube sample at film-anode separation of 250 μm. The current is measured while the sample is exposed to hydrogen at 3×10^{-7} Torr for a period of 6 hours.

Figures 5.13 and 5.14 are graphs of the exposure of SWNTs and MWNTs to H_2 respectively. Again H_2 does not have any effect on the magnitude of the FE current emitted by the SWNTs or the MWNTs. These results of the exposure of the SWNTs and MWNTs to Ar and H_2 are consistent with the respective F-N data presented in Figures 5.5 – 5.8.

5.9 Conclusion

In summary , O_2 exposure temporarily increases the turn-on field of SWNTs by 22% and decreases the FE by two orders of magnitude. However, the FE properties completely recover after approximately 40 hours of FE operation in UHV. For MWNTs, the higher voltage O_2 exposure leads to a 43% increase of the turn-on field and reduction of FE current by 3 orders of magnitude. Recovery in UHV is only partial, indicating that the MWNTs suffer permanent degradation of FE characteristics. The ratios of the slopes before and after O_2 exposure are approximately 1.04 and 0.82 for SWNTs and MWNTs, respectively, indicating that the geometric field enhancement factor of MWNTs decreases after O_2 exposure. H_2 and Ar gases do not significantly affect the FE properties of SWNTs or MWNTs. SWNTs compared to MWNTs would appear to make more economical and reliable vacuum electron sources.

References

1. Q. Y. Wang and J. K. Johnson, *J. Chem. Phys*. **110**, 577 (1999).

2. F. Darkrim and D. Levesque, *J. Chem. Phys*. **109**, 4981 (1998).

3. Q. Y. Wang and J. K. Johnson, *J. Phys. Chem. B* **103**, 4809 (1999).

4. Y. Ye, C. C. Ahn, C. Witham, and B. Fultz, J. Liu, A. G. Rinzler, D. Colbert, K. A. Smith, and R. E. Smalley, *Appl. Phys. Lett.* **74**, 2307 (1999).

5. A. C. Dillon, K. M. Jones, T. A. Bekkedahl, C. H. Kiang, D. S. Bethune, and M. J. Heben, *Nature* (London) **386**, 377 (1997).

6. P. Chen, X. Wu, J. Lin, and K. L. Tan ,*Science* **285**, 91 (1999).

7. S. M. Lee and Y. H. Lee, *Appl. Phys. Lett*. **76**, 2877 (2000).

8. W. P. Dyke and W. W. Dolan, *Adv. Electron. Electron Phys.* **8**, 89 (1956).

9. J. Y. Cavaille and M. Dechsler, *Surf. Sci.* **75,** 342 (1978).

10. K. A. Dean, and B. R. Chalamala, *Appl. Phys. Lett.* **75**, 3017 (1999).

11. S. Talapatra and A. D. Migone *Phys. Rev. Lett*. **87**, 206106-1 (2001).

12. J. Kong, N. R. Franklin, C. Zhou, M. G. Chapline, S. Peng, K. Cho, and H. Dai, *Science* **287**, 622 (2000).

13. P. G. Collins, K. Bradely, M. Ishigami, and A. Zettl, *Science* **287**, 1801 (2000).

14. J. -M. Bonard, J. -P. Salvetat, T. Stockli, W. A. de Heer, *Appl. Phys. Lett*. **73**, 918 (1998).

15. J. -M. Bonard, F. Maier, T. Stockli, A. Chatelain, W. A. de Heer, J. -P. Salvetat, and L. Forro, *Ultramicroscopy* **73**, 7 (1998).

16. D. S. Chung, W. B. Choi, J. H. Kang, H. Y. Kim, and I. T. Han, Y. S. Park Y. H. Lee, N. S. Lee, J. E. Jung, and J. M. Kim, *J. Vac. Sci. Technol. B* **18**, 1054 (2000).

17. B. R. Chalamala, R. M. Wallace and B. E. Gnade, *J.Vac. Sci. Technol. B* **16,** 2859 (1998).

18. K. A. Dean, and B. R. Chalamala, *J. Appl. Phys.* **85**, 3832 (1999).

19. K. A. Dean, and B. R. Chalamala, *Appl. Phys. Lett.* **76**, 375 (2000).

20. P. J. F. Harris, Carbon Nanotubes and Related Structures, New Materials for the Twenty-first Century (Cambridge University Press, Cambridge, 1999).

21. S. Amelinckx, X. B. Zhang, D. Bernaerts, X. F. Zhang, V. Ivanov and J. B. Nagy, *Science*, **265**, 635 (1994).

22. X. F. Zhang, X. B. Zhang, G. Van Tendeloo ,S. Amelinckx, M. Op de Beeck, J. Van Landuyt, *J. Cryst. Growth* **3**, 130 (1993).

23. R. T. K. Baker, *Carbon* **27**, 315 (1989).

24. Tubes@Rice, P.O. Box 1892, Houston, TX 77251

25. E. W. Mueller and T. T. Tsong, *Field Ion Microscopy, Principles and Applications* (Elsevier, New York, 1969).

BIBLIOGRAPHY

Adachi, H., Fujii, K., Zaima, S., Shibata, Y., Oshima, C., Otani, S. and Ishizawa, Y., *Appl. Phys. Lett.* **43**, 702 (1983).

Amelinckx, S., Bernaerts, D., Zhang, X. B., Van Tendeloo, G. and Van Landuyt, J. *Science*, **267**, 1334 (1995).

Amelinckx, S., Zhang, X. B., Bernaerts, D., Zhang, X. F., Ivanov , V. and Nagy, J. B. *Science*, **265**, 635 (1994).

Baker, R. T. K. *Carbon* **27**, 315 (1989).

Banwell, C. N. and McCash, E. M. , Fundamentals of Molecular Spectroscopy (McGraw-Hill Book Company, UK, 1994).

Bell, R. L., *Negative Electron Affinity Devices* (Clarendon, Oxford, 1973).

Bernaerts, D., Op De Beeck, M., Amelinckx, S., Van Landuyt, J., Van Tendeloo,G. *Phil. Mag. A* ,**74** , 723 (1996).

Biernet, T., Begen, J. and . Meclewski, R., *Surf. Sci.* **266**, 11 (1992).

Blakemore, J. S., *Solid State physics* (Cambridge University Press, Cambridge, (1985), pp.192.

Bohm, D., *Quantum Theory* (Prentice-Hall, Englewood Cliffs, 1951).

Bonard, J.-M., Kind, H., Stockli, T. and Nilsson, L.-O., *Solid-State Electronics* **45**, 893 (2001).

Bonard, J. -M., Salvetat, J. -P., Stockli, T., Forro, L. and Chatelain , A., *Appl. Phys. A* **69**, 245 (1999).

Bonard, J. -M., Salvetat, J. -P., Stockli, T., De Heer, W. A. *Appl. Phys. Lett.* **73**, 918 (1998).

Bonard, J. -M., Maier, F., Stockli, T., Chatelain, A., De Heer, W. A., Salvetat, J. -P., and Forro, L. *Ultramicroscopy* **73**, 7 (1998).

Burleigh Instruments, Inc., Fishers, NY 14453.

Cavaille, J. Y. and Dechsler, M. *Surf. Sci*. **75**, 342 (1978).

Chalamala, B.R., Wallace, R. M., and Gnade, B.E., *J.Vac. Sci. Technol. B* **16** (1998).

Chen, P., Wu, X., Lin, J. and Tan, K. L., *Science* **285**, 91 (1999).

Chung, D. S., Choi, W. B., Kang, J. H., Kim, H. Y., and. Han, I. T., Park Y. S., Lee, Y H., Lee, N. S., Jung, J. E., and Kim, J. M., *J. Vac. Sci. Technol*. **B 18**, 1054 (2000).

Collins, P. G., Hersam, M., Arnold, M., Martel, R. and Avouris , P., *Phys. Rev. Lett.* **86**, 3128 (2001).

Collins, P. G., Bradely, K., Ishigami, M. and Zettl, A., Science **287**, 1801 (2000).

Darkrim, F. and Levesque, D., *J. Chem. Phys*. **109**, 4981, (1998).

Davis, L.E. , MacDonald, N. C., Palmberg, P. W., Riach, G. E. and Weber, R. E., *Handbook of Auger Electron Spectroscopy* (Physical Electronics Industries, eden Prairie, 1976).

De Heer, W.A., Chatelain, A. and. Ugarte, D. *Science* **270**, 1179 (1995).

Dean, K. A., Allen, P.V. and Chalamala, B. C., *J. Vac. Sci. Tech*. **B 17** 1959 (1999).

Dean, K. A., Groening. O., Kuttel, O. M. and Schlapbach, L., *Appl. Phys. Lett.* **75**, 2773 (1999).

Dean, K. A. and Chalamala,B. R., *Appl. Phys. Lett*. **75**, 3017 (1999).

Dean, K. A. and Chalamala,B. R. *Appl. Phys. Lett.* **76**, 375 (2000).

Dean, K. A., and Chalamala, B. R., *J. Appl. Phys*. **85**, 3832 (1999).

Delaney, P., Ventra, M. D. and Pantelides, S. T., *Appl. Phys. Lett.* **75**, 3837 (1999).

Frank, S., Poncharal, P., Wang, Z. L. and de Heer, W. A., *Science* **280**, 1744 (1998).

Dillon, A. C., Jones, K. M., Bekkedahl, T. A., Kiang, C. H., Bethune, D. S. and Heben, M. J., *Nature* (London) **386**, 377 (1997).

Dyke, W. P. and Dolan, W. W., *Adv. Electron. Electron Phys.* **8**, 89 (1956).

Fischer, J. E., Lee, R. S., Kim, H. J., Rinzler, A. G., Smalley, R. E., Yaguzhinski, S. L.,

Bozhko, A. D., Sklovsky, D. E. and Nalimova, V. A., *Phys. Rev. B* **55,** R4921 (1997).

Fowler, R.H. and Nordheim, L. W., *electron Emission in Intense electric Fields*, Proc. *Roy. Soc., Ser. A,* **Vol. 119**, 173 (1928).

Geis, M. W. and Twichell, J. C., *Appl.Phys. Lett.* **67**, 1328 (1995).

Geis, M.W. and Twichell, J.C., *Appl.Phys. Lett.* **67**, 1328 (1995).

Gomer, R., *Field Emission and Field Ionization*, (Harvard University Press, Cambridge, MA 1961).

Good, R. H. and Meuller, E. W., Handbuch der Physik, (Springer, Berlin,1956), vol 21, pg 26.

Grigorian,L., Sumanasekera, G.U., Loper, A.L., Fang, S., Allen, J. L. and Eklund, P.C., *Phys. Rev. B*, **58,** R4195 (1998).

Haas, G. A., Thomas, R. E., Marrian, C. R. K., and Shih, A., *IEEE Trans. Electron Dev.* **ED-38**, 2244 (1991).

Haefer, R., *Z., Phys.* **116**, 604 (1940).

Hamada, T., Furuyama, M., Tomioka, T., and Endo, M., *J. Mater. Res.* **7**, 1178 (1992).

Han, S and Ihm, J., *Phys. Rev. B.* **61**, 9986 (2000).

Harris, P. J. F., Carbon Nanotubes and Related Structures, New Materials for the Twenty-first Century (Cambridge University Press, Cambridge, 1999).

Hone, J., Ellwood, I., Muno, M., Mizel, A., Cohen, M. L., Zettl, A., Rinzler, A. G. and

Smalley, R. E., *Phys. Rev. Lett.* **80**, 1042 (1998).

Iijima, S., *Nature*, 354 (1991).

Jaskie, J. E., *MRS Bulletin* **21**, 3,59 (1996).

Jishi, R. A., Inomata, D., Nakao, K., Dresselhaus, M. S. and Dresselhaus , G., *J. Phys Soc. Jpn*. **63**, 2252 (1994).

Joshi, A., *Metals Handbook Ninth Edition: Volume 10, Materials characterization*, (American Society for Materials Park, OH 1986).

Kaiser, A. B., Dusberg, G. and Roth, S., *Phys. Rev. B* **57**, 1418 (1998).

Ko, Y. W. and Kim, S. I., *J. Appl. Phys.* **82**, 2631 (1997).

Kong, J., Franklin, N. R., Zhou, C., Chapline, M. G., Peng, S., Cho, K., and Dai, H., *Science* **287**, 622 (2000).

Lee, R. S., Kim, H. J., Fisher, J.E.,. Thess, A., Smalley, R.E., *Nature* **388,** 257 (1997).

Lee, R. S., Kim, H. J., Fisher, J.E.,. Thess, A., Smalley, R.E., *Nature* **388,** 255 (1997).

Lee, S. M., and Lee, Y. H., *Appl. Phys. Lett*. **76**, 2877 (2000).

Macaulay, J. M., Brodie, I., Spindt, C. A., and Holland, C. E., *Appl. Phys. Lett*. **61**, 997 (1992).

Marrian, C. R. K., Haas, G. A., and Shih, A., *Appl. Surf. Sci.* **16,**73 (1983).

Martinelli, R. U., and Fischer, D. G., *Proc. IEEE* **62**, 1339 (1974).

Martinelli, R.U. and Fischer, D.G., *Proc. IEEE* **62**, 1339 (1974).

MDC Vacuum Products Corporation, 23842 Cabot Boulevard, Hayward, CA 94545-1651.

Mintmire, J. W., Dunlap, B. I. and White, C. T., *Phys. Rev. Lett*. **68,** 631 (1992)

Mintmire, J. W., Robertson, D. H., and White, C. T., *J. Phys. Chem. Solids* **54,** 1853 (1993).

Mueller, E. W. and Tsong, T. T., *Field Ion Microscopy, Principles and Applications* (Elsevier, New York, 1969).

Omicron Associates, 1226 Stoltz Road, Bethel Park, PA 15102.

Pan, L. S., Felter, T. E., Ohlberg, D. A. A., Hsu, W. L., Fox, C. A., Cao, R.,and Vergara, G., *J. Appl. Phys.* **82**, 2624 (1997).

Rao, A. M., Richter, E., Bandow, S., Chase, B., Eklund, P.C., Williams, K.C., Menon, M., Subbaswamy, K. R., Thess, A., Smalley, R. E., Dresselhaus, G., and Dresselhaus, M. S., *Science* **275**, 187 (1997).

Rao, A. M., Eklund, P.C., Bandow, S., Thess, A., Smalley, R. E., *Nature* **388**, 257 (1997).

Rinzler, A. G., Liu, J., Dai, H., Nikolaev, P., Huffman, C.B., Rodriguez-Macias, F.J., Boul, P.J., Lu, A. H., Heymann, D., Colbert, D. T., Lee, R. S., Fischer, J. E., Rao, A.M. , Eklund, P.C. and Smalley, R.E. *Appl. Phys. A* **67**, 29 (1998).

Rinzler, A. G., Hafner, J. H., Nikolaev, P., Lou, L., Kim, S.G., Tomanek, D., Nordlander, D. T., Nordlander, P., Colbert, D.T., and. Smalley, R.E., *Science* **269**, 1550 (1995).

SAES Getters, Inc., Colorado Springs, CO 80906.

Saito, R., Fujita, M., Dresselhaus, G. and Dresselhaus, M. S., *Phys. Rev. B* **46**,1804 (1992).

Saito, R., Dresselhaus, G. and Dresselhaus, M. S., *J. Appl. Phys*. **73**, 494 (1993).

Dresselhaus , M. S., Jishi, R. A., Dresselhaus, G., Inomata, D., Nakao, K. and Saito, R., *Molecular Materials* **4**, 27 (1994).

Saito, R., Dresselhaus, G., and Dresselhaus , M.S., Physical Properties of Carbon Nanotubes (Imperial College Press, London, 1998).

Saito,R., Fujita, M., Dresselhaus, G. and Dresselhaus, M. S., *In Electrical Optical and Magnetic Properties of Organic Solid State Materials, MRS Symposia Proceedings*, Boston, edited by L. Y. Chiang, A. F. Garito, and D. J. Sandman, page 333, Materials Research Society Press, Pittsburgh, PA, 1992.

Saito,R., Fujita, M., Dresselhaus, G. and Dresselhaus, M. S., *Appl. Phys. Lett.* **60**, 2204 (1992).

Schottky, W., *Z. tech. Physik*, **14**, 63 (1923).

Spindt, C.A., Brodie, I., Humphrey, L., and Westerberg, E.R., *J. Appl. Phys.* **47**, 5248 (1976).

Succi, M., Canino, R. and Ferrario, B., *Vacuum* **35**, 579 (1985).

Suzuki, S. and Tomita, M., *J. Appl. Phys.* **79** 3739 (1996).

Suzuki, S., Bower, C., Watanabe, Y. and Zhou, O., *Appl. Phys. Lett.* **76**, 4007 (2000).

Suzuki, S., Bower, C., Watanabe, Y. and Zhou, O., *Appl. Phys. Lett*. **76**, 4007 (2000).

Suzuki, S., Bower, C. and Zhou, O., *Chem. Phys. Lett* **285**, 230 (1998).

Talapatra, S. and Migone, A. D., *Phys. Rev. Lett*. **87**, 206106-1 (2001).

Tamura, R. and Tsukada, M., *Phys. Rev. B.* **52**, 6015 (1995).

Thess, A., Lee, R. , Nikolaev, P., Dai, H., Petit, P., Robert, J., Xu, C., Lee, Y.H., Kim, S .G. , Rinzler, A.G., Colbert, D.T., Scuseria, G.E., Tomanek, D., Fischer, J. E.,. Smalley, R.E., *Nature* **273**, 488 (1996).

Tubes@Rice, P.O. Box 1892, Houston, TX 77251.

Wang, Q. Y. and Johnson, J. K., *J. Chem. Phys*. **110**, 577 (1999).

Wang, Q. Y. and Johnson, J. K., *J. Phys. Chem. B* **103**, 4809 (1999).

Ye,Y., Ahn, C. C., Witham, C. and Fultz, B., Liu, J., Rinzler, A. G., Colbert, D., Smith, K. A. and Smalley, R. E., *Appl. Phys. Lett.* **74**, 2307 (1999).

Zhang, X F., Zhang, X. B., Van Tendeloo , G., Amelinckx, S., Op de Beeck, M., Van Landuyt, J . *J. Cryst. Growth* **3**, 130 (1993).

Zhou, O. Fleming, R. M., Murphy, D. W., Chen, C. H., Haddon, R.C., Ramirez, A. P., Glarum, S. H., *Science* **263** , 1744 (1994).